New insights on how changing hydroclimate might affect crop yields -- and a way to avoid the worst of it

Corey Samuel Lesk

Submitted in partial fulfillment of the
requirements for the degree of
Doctor of Philosophy
under the Executive Committee
of the Graduate School of Arts and Sciences

COLUMBIA UNIVERSITY

2022

Abstract

New insights on how changing hydroclimate might affect crop yields -- and a way to avoid the worst of it

Corey Samuel Lesk

Climate change threatens global food security by increasing extreme-weather shocks and reducing the productivity of major global crops. While recent research has highlighted the risk of rising extreme heat, comparatively little is known about how the intensity distribution of rainfall, and rainfall's interactions with heat, influence global crops. Further, as the broader climate transition gains momentum, the industrial activities needed to mitigate and adapt to climate change will emit CO_2. These emissions remain unquantified and largely ignored in research and policy, and thus present an under-assessed risk to crops and society at large.

This thesis advances the understanding of present and future agricultural risks from two aspects of hydroclimatic complexity: hourly rainfall intensity and temperature-moisture (T-M) couplings. Both aspects are expected to shift under climate change, with highly uncertain crop impacts. It further simulates the adaptation and mitigation emissions embedded in the broader climate transition, illuminating a previously under-appreciated benefit of enhance climate ambition.

Climate warming is expected to intensify rainfall, decreasing the frequency of drizzle while boosting heavy and extreme events. I show that surprisingly heavy rainfall is optimal for US maize and soy yields, with yield loss due to drizzle and very extreme downpours. As a result, the future concentration of rainfall into fewer, heavier hourly events will benefit crop yields 2-3%, partly offsetting larger damages from warming.

T-M couplings arising from land-air interactions and atmospheric circulation may shift under 21st Century warming, altering the likelihood of concurrent heat and drought extremes, with uncertain risks to crops. I demonstrate that maize and soy grown in regions with strong T-M couplings historically suffered enhanced crop sensitivity to heat. These couplings will strengthen over most of global croplands this century, worsening the impact of warming on crops by 5% globally, with large regional variations.

The energetic demands of the broader climate transition – such as steel for wind turbines, and concrete for coastal barriers – will initially be satisfied by fossil fuels. I show that simulated mitigation and adaptation will emit 185GtCO_2 by 2100 under a transition path consistent with current policies (~2.7°C warming by 2100), equivalent to half the remaining carbon budget for 1.5°C. However, these emissions can be reduced by 90% under a 1.5°C transition path, a previously unidentified co-benefit of enhanced climate ambition.

Table of Contents

Acknowledgments

I would like to thank the many people who made this research possible and enjoyable. I could not have made sense of any of this research without the thoughtful feedback and hard work of my co-authors: Ethan Coffel, Jonathan Winter, Jakob Zscheischler, Sonia Seneviratne, Deepak Ray, Denes Csala, Sgouris Sgouridis, Antoine Levesque, Robin Krekeler, Katharine Mach, Daniel Horen Greenford, and Damon Matthews. Many other dear colleagues inspired or improved this work, including Jonas Jagermeyr, Justin Mankin, Weston Anderson, Nathan Lenssen, Delavane Diaz, Caleb Gingrich, and Anton Safonov. I owe even considering doing a PhD, let alone much guidance along the way, to my advisor Radley Horton. My committee members Mingfang Ting and Ruth DeFries shaped this research with their astute feedbacks and guidance, and welcomed me into their research groups. I am also grateful to countless past and present members of the Lamont and Columbia communities for all the conversations big and small over the years. Finally, and certainly not least, I thank my partner, Sarah Yahyaoui, for her loving support and sagacious scientific sense.

Dedication

To the farmers of the world, who marry sky and soil to keep us fed.

Introduction

The global emissions trajectory and the future of climate extremes

The 26th Conference of the Parties (COP 26) to the United Nations Framework Convention on Climate Change in 2021 was at once watershed and a missed opportunity. Most countries enhanced their national greenhouse gas mitigation pledges, inching their aggregate climate pathway 0.3°C closer to the 1.5°C maximum warming goal agreed to in Paris (Rogelj et al., 2016). However, even if these enhanced pledges come to fruition, the planet is on track for *additional* warming of 1.8-2.3°C (Climate Action Tracker, 2021; UNEP, 2020).

The watershed was spiritual – there is now wind in the sails of the clean energy transition and the imperative of adaptation. The broader climate transition – including mitigation and adaptation – is no longer a question of 'if', but 'when 'and 'how'. The missed opportunity was to actually align policy pledges with the strong biogeoscientific consensus that any warming above 1.5°C is a risk to planetary and human wellbeing not worth taking (Hoegh-Guldberg et al., 2018). Drastic mitigation effort would be needed throughout the 2020s, but pledges are still falling short, and global policy priorities have shifted to address more near-term concerns of pandemics and conflicts.

Given this status quo, some serious consequences of climate change are unlikely to be avoided. While gradual warming and changes in precipitation will affect ecosystems and human societies, the bulk of climate damages are likely to be concentrated in worsening extreme climate events including droughts, extreme heat, and extreme precipitation (Sippel et al., 2018; E. Vogel et al., 2019). These events have already become more frequent, intense, and widespread in recent decades, and are robustly projected to continue in that direction as long as humans emit net greenhouses gases into the atmosphere (Seneviratne, 2019).

Of particular concern are compound extreme events, a topic that has drawn substantial academic interest and societal anxiety in the past few years. Various forms and conceptualizations of compound extremes have been identified and proposed (Leonard et al., 2013; Raymond et al., 2020; Zscheischler et al., 2020), but they all address two potentials. First, interactions among physical climate process in the genesis of extremes can cause them to take on unique multivariate, spatial, and temporal characteristics, and pose unique challenges (Zscheischler & Seneviratne, 2017). Second, extremes with compound multivariate, spatial, and temporal dimensions often induce unique and severe impacts on human and natural systems (Van Der Wiel et al., 2020). For instance, a heat wave can have outsize impacts on vegetation during meteorological drought (Gampe et al., 2021), not only because the atmospheric drivers of heat and drought are connected and mutually amplifying (Seneviratne et al., 2010), but because combined heat-and-drought stresses can trigger especially severe disruption to plant physiology and photosynthesis (Suzuki et al., 2014).

Compound extremes and global stable crops

Climate is a major driver of temporal and spatial variation in crop yield (i.e., harvested product per unit area, or productivity). Although the number of calories produced only partly determines food security—questions of access and distribution are also fundamental—productive crops underpin the global food system, commodity prices, human wellbeing, and rural livelihoods. Other social and natural factors such as policy and pathogens also influence crop production, and can complicate detecting climate signals. Nevertheless, up to half of year-to-year variation in crop yields globally can be explained by variation in climate (Frieler et al., 2017;

Ray et al., 2015), with extreme events playing a particularly important role (E. Vogel et al., 2019).

As climate-related hazards mount, temperature extremes, drought, and moisture excess are increasingly colliding in space and time (Lesk & Anderson, 2021; Ridder et al., 2022; Sarhadi et al., 2018; Zscheischler et al., 2020). The compound effects of multiple, interacting climate extremes pose a challenge to understanding how climate variability affects staple crop yields, projecting the impacts of multifaceted future climate change, and adapting cropping and food systems. Further, changing interactions between heat, moisture, atmospheric CO_2 concentration and plants are among the largest uncertainties surrounding how climate change will affect global crop productivity.

For example, pioneering statistical modeling of agricultural data revealed a particular sensitivity of staple crop yields to extreme heat (Lobell et al., 2011; Schlenker & Roberts, 2009). However, while extreme temperatures can directly disrupt metabolism, damage crop tissue, and reduce yield capacity, they can also induce moisture stress by raising evaporative demand (Buckley, 2019; Grossiord et al., 2020). Land-surface drying also often amplifies atmospherically-driven heating, physically linking the two extremes (Miralles et al., 2019; Brigitte Mueller & Seneviratne, 2012). Furthermore, crop responses to combined drought and heat stresses are physiologically distinct from those to individual stresses (Cohen et al., 2021; Ostmeyer et al., 2020), and often more severe (Matiu et al., 2017). Such connections between water and heat in the physics of climate extremes and the biology of their crop impacts raise the potential for compound, interactive effects of changing precipitation, temperature, and aridity.

Recent data and experimental advances have enabled disentangling and diagnosing correlated climate drivers of crop yields, and more complete and accurate projection of future

agricultural risks and opportunities. Applications of satellite observations of root-zone soil moisture, for instance from the Soil Moisture Active-Passive (SMAP) project (Entekhabi et al., 2010), have provided the most direct evidence to date of the importance for crop yields of soil water supply relative to atmospheric demand (Ortiz-Bobea et al., 2019; Rigden et al., 2020). These results help explain the resistance of irrigated crop yields to high temperatures that would strongly suppress the yield of rainfed crops (Carter et al., 2016; Schauberger et al., 2017). They further provide mechanistic clarity on the particularly severe yield effects of combined heat and drought (Matiu et al., 2017).

Future changes in crop productivity will thus depend on the evolution of many climate variables and their interactions. However, projections of the response of some of these variables to anthropogenic greenhouse gas emissions are highly uncertain. Critically, the response of soil moisture to climate warming is complicated by uncertainty over future changes in precipitation and its partitioning to soil moisture, runoff, and evapotranspiration (Allan et al., 2020; Ault, 2020; Fowler et al., 2021; Scheff et al., 2021; Ukkola et al., 2020). Future warming is, by contrast, projected with relatively high confidence. But the degree to which warming will benefit or hurt crop yields will ultimately depend on hydrologic variables and their co-variability with temperature.

The emerging mechanistic understanding of compound climate impacts on crops thus raises new scientific questions and presents challenges for adapting crops and farming systems to climate change. The overarching goal of the first two chapters of this thesis is to understand the historical and future implications for crop yields of two modes of heat-moisture co-variability that drive compound extremes. The first is the dependence of sub-daily rainfall intensity on temperature, and the second is the seasonal temperature-moisture couplings that control

imbalances of moisture supply and demand. Below, I briefly characterize the present understanding of – and key knowledge gaps in – these two modes of heat-moisture co-variability and their crop impacts.

Sub-daily rainfall intensification and its crop implications (prelude to Chapter 1)

Although early statistical analyses of crop-climate relationships found little global influence of seasonal total precipitation on yields (Lobell et al., 2011; Schlenker & Roberts, 2009), more recent studies have demonstrated improved prediction of historical crop yields using microwave soil moisture observations (Ortiz-Bobea et al., 2019; Rigden et al., 2020), at least in the US where observations are sufficiently available. In particular, these studies stress the importance of *plant-available* soil moisture relative to atmospheric vapor demand. A possible explanation for the weak statistical link between crop yields and seasonal precipitation is that the latter may only weakly determine the sub-seasonal evolution of soil moisture. Many factors can mediate whether falling precipitation becomes plant-available as soil moisture or is lost to runoff or evaporation, including canopy structure, interception dynamics, and soil texture and permeability. However, the relevance of these factors ultimately depends on the intensity of the incoming precipitation, which on sub-daily timescales can vary by up to three orders of magnitude and is closely dependent on temperature.

On sub-daily timescales, warmer temperatures are linked to heavier rainfall because water-holding capacity of the atmosphere rises approximately 7%/°C (or, more precisely, because the water vapor pressure at which free-surface condensation and vaporization reach equilibrium increases by 7%/°C, such that at saturation, warmer air contains more vapor than cooler air). Further, surface heat can favor rising air (convection), additionally fueling thunderstorms

dynamically and boosting rainfall intensification up to 40%/°C. Future change in this moisture-heat interaction is relevant for crops for two reasons.

First, overall rainfall intensity is expected to increase with long-term warming, shifting the sub-seasonal rainfall distribution. Hourly to daily rainfall events have intensified in recent decades according to observational trends at rates exceeding earlier model- or theory-based projections, with greater increases at sub-daily time scales (Ali et al., 2021; Fowler et al., 2021; Westra, S., Fowler, H. J., Evans et al., 2014). The concentration of total rainfall into fewer, heavier events implies that precipitation frequency may decrease overall (Dai et al., 2020). The crop yield implications of these rainfall intensity and frequency changes across sub-seasonal timescales remain uncertain. For example, studies using daily rainfall totals estimate yield losses with rainfall intensification due to the decreasing number of rainy days during the growing season, even if total growing season precipitation remains constant or increases (Fishman, 2016; Shortridge, 2019). However, analyses at the daily scale aggregate a wide diversity of sub-daily rainfall intensities – a daily 25mm rainfall total can occur as a single hour of severe thunderstorms, or as a full day of steady drizzle. The crop yield response to hourly rainfall intensity remains crucially understudied, yet essential to project the crop implications of simultaneous rainfall changes across sub-daily to seasonal timescales.

Second, since heavy short-duration rainfall is more likely on hot days in many regions, future extreme heat and precipitation may become increasingly concurrent. Rainfall intensities have been observed to increase with temperature on hourly-to-daily scales, consistent with theory (Fowler et al., 2021; Westra, S., Fowler, H. J., Evans et al., 2014). As such, compound extreme heat-precipitation events are relatively common – for instance, over 1960-2016 in China, 23% of precipitation extremes immediately followed a heat event (Ning et al., 2022). However, the

understanding of compound or compensating extreme heat-precipitation impacts on crop yields is limited. Further research is needed on the extent to which future rainfall intensification on hot days – or other convection-related covariates such as cloud cover – might alleviate or exacerbate the crop yield impacts of increasing extreme heat.

Chapter 1 of this thesis examines the historical sensitivity of US crop yields to hourly rainfall intensity, and projects the yield impacts of rainfall intensification under warming. It constitutes a novel effort to understand the influence of sub-daily rainfall intensity on crops, and lays groundwork for integrating insights at that timescale across sub-seasonal timescales. Further, it provides an initial estimate of the extent to which rainfall intensification may counteract the impacts of hotter future heat extremes.

Temperature-moisture couplings and compound climate risks to crops (prelude to Chapter 2)

The land-atmosphere system is connected through large-scale atmospheric circulation (dynamics), the land surface water-energy balance (thermodynamics), and regulation of land-surface water and energy fluxes by vegetation (physiology). These mechanisms often occur simultaneously, and together strongly determine the co-variability of temperature and moisture, and thus the occurrence of compound extremes like combined heat and drought, which so strongly impact crop yields.

Heat waves are generally driven by atmospheric blocking, which results in high pressure atmospheric circulation patterns favoring clear skies, warm and descending winds, and high solar radiation (Horton et al. 2016). Such heat-wave patterns thus typically co-occur with low precipitation (Trenberth & Shea, 2005). These large-scale dynamic land-atmosphere interactions

can amplify (Koster et al., 2016), mitigate (Zhou et al., 2021), or shape the timing and location (A. Berg et al., 2017) of hot-dry extremes by altering moisture convergence or monsoon onset.

Thermodynamic land-atmosphere interactions primarily concern the partitioning of incoming energy at the land surface into that used to evaporate water (latent heating) and that which increases surface temperatures (sensible heating). If the land surface becomes water-limited, air temperatures rise quicker, as more energy is partitioned to sensible heating, creating a positive feedback between decreasing soil moisture and increasing temperature (A. Berg et al., 2016; Miralles et al., 2019; Seneviratne et al., 2010). This feedback occurs most strongly in semi-humid to semi-arid (i.e, transitional) zones, including important breadbaskets in Central Europe and the North American Great Plains (Zscheischler & Seneviratne, 2017). In these regions climate change is expected to strengthen this land-atmosphere feedback by increasing evaporative demand and drying surface and root-zone soil moisture (Cook et al., 2020), boosting the occurrence of joint hot-dry extremes in the warm season (A. Berg et al., 2014, 2016; Zscheischler & Seneviratne, 2017). These interactions have likewise been observed to work in reverse over more humid mid-latitude and tropical breadbaskets, where increased evapotranspiration from soils and natural vegetation cools summertime temperatures (N. D. Mueller et al., 2017; Singh et al., 2018). In these regions, climate change may nonetheless strengthen land-atmosphere interactions during droughts, resulting in extremely dry days that are hotter than would be expected from warming alone (Byrne, 2021).

Natural vegetation and its physiological responses to climate further alter evapotranspiration, the terrestrial water cycle, and the evolution of compound climate extremes (Lian et al., 2018; Wei et al., 2017). For instance, stomatal closure during high temperatures and VPD can conserve soil moisture, but boost land temperatures (Miralles et al., 2019; Teuling et al.,

2010). The influence of natural vegetation on regional climate extremes will likely shift as higher atmospheric CO2 concentrations alter vegetation physiology (McDermid et al., 2021; Skinner et al., 2018; Swann et al., 2016). However, the magnitude and even sign of these changes are actively debated (Cook et al., 2020; Allan et al. 2020).

Heat and moisture variations are closely linked not only in the climate system through these three categories of interaction, but within crops through complex physiological interactions at the molecular to plant scales. Crop physiological responses to combinations of extremes – such as extreme heat and low soil moisture – are often unique and cannot be adequately extrapolated from responses of the individual components (Choudhury et al., 2017; H. Zhang & Sonnewald, 2017). Additionally, the order of occurrence of these extreme (e.g., co-occurring or sequential) elicits varying degrees of complex responses - defined by different, and sometimes opposing, signaling pathways (Suzuki et al., 2014). Ultimate yield impacts of compound extremes thus reflect intertwined physiological responses to multiple aspects of climate.

Climate change entails not only changes in long-term means and extremes of temperature, precipitation, and soil moisture, but also in their co-variability, which is largely determined by the processes described above. The historical climate dynamics and future evolution of these processes is a topic of ongoing interest. However, their relevance to global crop yields, now and in the future, remains largely unstudied. In Chapter 2, I statistically characterize the strength of temperature-moisture couplings over global croplands, examine how the strength of these couplings has historically influenced crop yield sensitivity to temperature, and apply a suite of climate model projections to assess the likely impacts of future changes in the couplings. By connecting the known crop risks of compound heat-drought events with their underlying climate dynamics, I draw new insights that help constrain future risks and better define the challenge of adaptation.

The incremental risk of warming to crops and the need for an effective climate transition (a rationale for Chapter 3)

As I will show, the hydroclimatic nuances explored in Chapters 1 and 2 are important to understand to what degree and by which mechanisms future climates will result in crop yield changes in the absence of adaptation. Further, by clarifying the mechanisms of impacts, the results of these chapters provide useful guidance to crop adaptation, which I expand briefly upon in the chapters and the Conclusions. However, these results broadly confirm their motivating concern: climate change will on average reduce crop productivity this century.

While fossil fuel combustion has provided easy energy to power rising living standards globally, its by-products now threaten the most basic underpinnings of human wellbeing. Nevertheless, process-based crop model projections suggest the majority of crop impacts can be avoided by limiting greenhouse gas emissions and climate warming (Jonas Jägermeyr et al., 2021; Schleussner et al., 2018). Under a high-emissions scenario (SSP5-8.5, ~4°C warming by 2100), global average maize yields decline by 30% in 2100 in the ensemble mean, compared with 6% in a moderately-ambitious mitigation scenario (SSP1-2.6, 1.8°C warming) (Jonas Jägermeyr et al., 2021). Between 1.5 and 2°C, uncertainties related to CO_2 physiological effects are strong compared to temperature signals, making definitive claims of differential impacts challenging (Schleussner et al., 2018). However, any amount of additional warming will reduce crop yields in the tropics, where households are most reliant on subsistence agriculture and where adaptive capacity is generally weakest.

For this and myriad other reasons, prompt, rapid, sustained, and effective mitigation of greenhouse gas emissions is overwhelmingly necessary. In this thesis, I focus on the clean energy

transition component of mitigation (as opposed to, for instance, reducing land-use emissions), partly because fossil fuel combustion is the largest source of emissions, and for technical reasons discussed in Chapter 3. The economic, technical, and political dimensions of clean energy transition proposals have been debated extensively (F. C. Moore et al., 2022; Pahle et al., 2022), and low-emissions energy systems are already being implemented at an accelerating rate (IEA, 2021). Alongside this trend, the imperative of adapting to the climate impacts we cannot (or choose not) to avoid is becoming clear (Berrang-Ford et al., 2021). Together, the twinned projects of deploying of clean energy systems and adapting to climate impacts can be thought of as a *broader climate transition*.

This transition will entail a massive global industrial project lasting at least decades. Initially, this project will inevitably be powered by fossil fuels as the dominant energy source at present, and will thus emit greenhouse gases. Rigorous accounting of the emissions produced by the current and future global economy is essential to effectively plan and execute the climate transition. Emissions accounting is also being increasing applied in the private sector for climate risk disclosure, with attendant potential for greenwashing. However, the broader climate transition is presently a small part of the economy, and its likely future emissions have not yet been constrained. This among other accounting omissions come with a risk that underappreciated future emissions sources jeopardize meeting globally agreed-upon mitigation targets. In Chapter 3, I aim to fill this gap by modeling the emissions likely to result from selected mitigation and interventions during the broader climate transition.

Chapter 1: Net benefits to US soy and maize yields from intensifying hourly rainfall

Published 10 August 2020, *Nature Climate Change*, https://doi.org/10.1038/s41558-020-0830-0

Many varieties of short-duration extreme weather pose a threat to global crop production, food security, and farmer livelihoods (Lesk et al., 2016; Schlenker & Roberts, 2009; Troy et al., 2015; E. Vogel et al., 2019). Hourly exposure to extreme heat has been identified as detrimental to crop yields (D. B. Lobell et al., 2013; Schlenker & Roberts, 2009), however the influence of hourly rainfall intensity and extremes on yields remains unknown (Rosenzweig et al., 2002; Troy et al., 2015; van der Velde et al., 2010). Here, we show that while maize and soy yields in the US are severely damaged by the rarest hourly rainfall extremes (≥50mm hr^{-1}), they benefit from heavy rainfall up to 20 mm hr^{-1}, roughly the heaviest downpour of the year on average. We also find that yields decrease in response to drizzle (0.1-1 mm hr^{-1}), revealing a complex pattern of yield sensitivity across the range of hourly intensities. We project that crop yields will benefit by ~1-3% on average due to projected future rainfall intensification under climate warming (O'Gorman & Schneider, 2009; Westra, S., Fowler, H. J., Evans et al., 2014), slightly offsetting larger expected yield declines from excess heat, with the benefits of more heavy rainfall hours outweighing the damages due to additional extremes. Our results challenge the view that an increasing frequency of high-intensity rainfall events poses an unequivocal risk to crop yields (Rosenzweig et al., 2002; E. Vogel et al., 2019; Zhu & Troy, 2018) and provide insights that may guide adaptive crop management and improve crop models.

1) Introduction

Crop production is sensitive to variation in climate and weather, with 30-40% of variability in global crop yields attributable to monthly and seasonal climate (Lobell & Field, 2007a; Ray et al., 2015). Recent research has emphasized the important impacts of short-duration weather extremes on crop yields, particularly the steep reductions from hourly exposure to high temperatures (Lobell et al., 2013; Schlenker & Roberts, 2009). However, the influence of short-duration rainfall intensity and extremes on yields remains scarcely understood and is widely omitted from historical analyses, crop models, and climate risk projections (Li et al., 2019; Rosenzweig et al., 2002; Troy et al., 2015; Urban, Roberts, et al., 2015; van der Velde et al., 2010; E. Vogel et al., 2019).

Assessments of the effects of rainfall variability on crop yields have focused on monthly to seasonal total accumulation, detecting regionally variable and often weak relationships(Lobell et al., 2013; D. B. Lobell & Gourdji, 2012; Lobell & Burke, 2008; David B Lobell & Field, 2007a; Ray et al., 2015; Schlenker & Roberts, 2009). However, rainfall occurs in events with mean duration of several hours that vary in intensity by up to three orders of magnitude, from less than 1 to over 100mm hr^{-1} (Palecki et al., 2005; Thorp & Scott, 1982). The response of crop yields to both extreme and common rainfall intensities remains obscured by analyses using longer-term rainfall totals. Given that the largest changes to rainfall climatology under global warming are projected to occur at sub-daily time scales (Westra, S., Fowler, H. J., Evans et al., 2014; W. Zhang et al., 2017), anticipating and adapting to the impacts of climate change on global crop production require a detailed understanding of the yield response to short-duration rainfall intensity.

In this study, we assess the sensitivity of crop yields in the United States to hourly rainfall intensity and extremes over 2002-2017. Combining high spatial resolution hourly rainfall observations with county-level maize and soy yield data, we identify threshold intensities of

extreme downpours with damaging effects on yields and two additional non-extreme intensity zones with significant impacts. We then illustrate the importance of hourly rainfall intensity to crops by comparing its influence to that of rainfall distribution across other timescales. Finally, we project future crop yield impacts under three scenarios of changing rainfall intensity in response to climate warming.

2) Results and discussion

We find substantial deleterious effects of the most extreme rainfall events on crop yields. County-level maize yields decline by 23-45bu ac^{-1} per hour of exposure to rainfall with intensities of 80-90mm hr^{-1} ($P < 0.05$, Fig. 1a-b, Appendix A Table 1), or 16-32% of the national mean yield. Soy yields decline at lower intensity thresholds of 50-70mm hr^{-1} and by a smaller amount of 2 to 4bu ac^{-1} per hour of exposure, or 5-10% of the national mean ($P < 0.01$, Fig. 1c-d, Appendix A Table 1). This yield reduction is similar for soy and larger for maize compared with daily exposure to extreme temperatures of 40℃ (~7% per day) (Schlenker & Roberts, 2009).

The impacts of such extreme rainfall events may result from direct damage to plant tissue, either by rainfall or the wind and hail that often accompany such storms (Lepore et al., 2016). Indirect mechanisms such as waterlogging and rhizosphere anoxia (Ashraf & Habib-ur-Rehman, 1999; Rosenzweig et al., 2002) or soil erosion (Martínez-Casasnovas et al., 2002) and soluble nutrient leaching (Meisinger & Delgado, 2002) may also cause or compound the yield reduction. These potential mechanisms may explain the differing responses between crops: soy may be damaged at a lower intensity than maize due to its broader foliar configuration and weaker stems, while the magnitude of damage may be mitigated by its nitrogen fixation capacity (Meisinger & Delgado, 2002; Zahran, 1999).

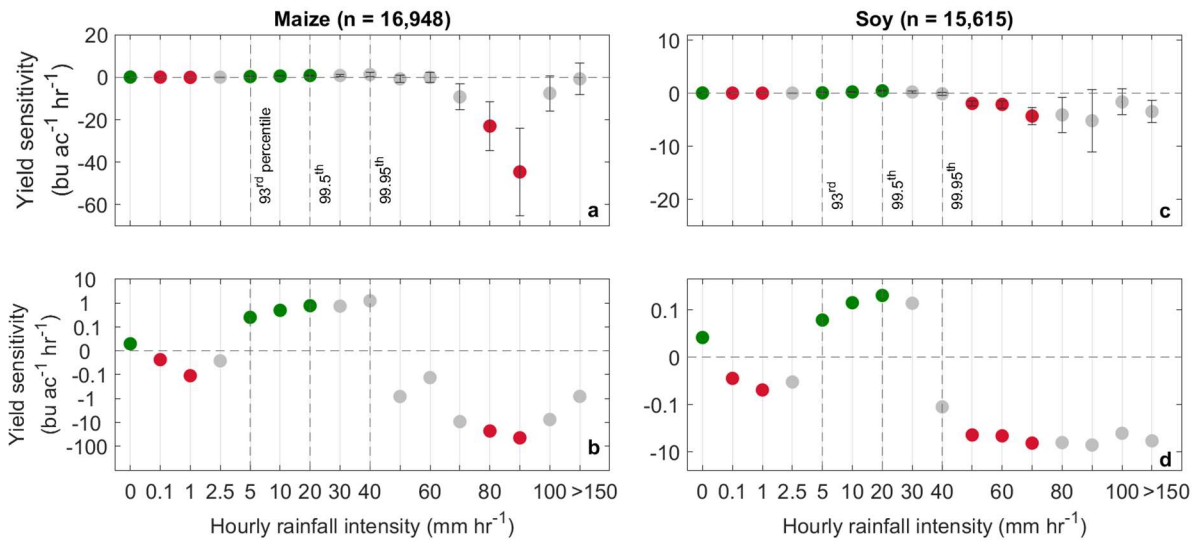

Figure 1: Sensitivity of maize and soy yields to hourly rainfall intensity. a) National mean county-level maize yield sensitivity (±SE) to hourly rainfall intensity per hour of exposure over 2002-2017. b) Same as a, but on symmetric logarithmic axes. c-d) Same as a-b, but for soy. Vertical dashed lines denote the indicated percentiles of climatological rainfall intensity. Sensitivities are inferred from a model controlling for exposure to beneficial and excessive heat and seasonal total rainfall. Sample sizes reflect county-year pairs. Dark green and red points indicate significant positive and negative sensitivities (two-sided $P < 0.05$, Appendix A Table 1). Transformed standard error estimates are omitted in b and d for clarity.

The damaging rainfall extremes exceed the 99.95th percentile of hourly intensity, representing once-per-decade to once-per-century events (Fig. 1, Fig. 2, Appendix A Table 2). In contrast, crop yields benefit from heavy rainfall up to the 99.5th percentile of hourly intensity, roughly a once-per-year event. Yields increase by ~1bu ac^{-1} hr^{-1} for maize and ~0.1bu ac^{-1} hr^{-1} for soy from exposure to heavy rainfall ranging from 5-20mm hr^{-1} ($P < 0.001$, Fig. 1a-d). Meanwhile, exposure to very light 'drizzle '(0.1 to 1mm hr^{-1}) corresponds to significant yield reductions in both maize (~0.1bu ac^{-1} hr^{-1}, $P < 10^{-8}$) and soy (~0.01bu ac^{-1} hr^{-1}, $P < 10^{-8}$). This drizzle effect is significant from 0.1-2.2mm hr^{-1} for maize and 0.1-1.4mm hr^{-1} for soy, and largest in magnitude between 1 and 2mm hr^{-1} (Appendix A Fig. 3).

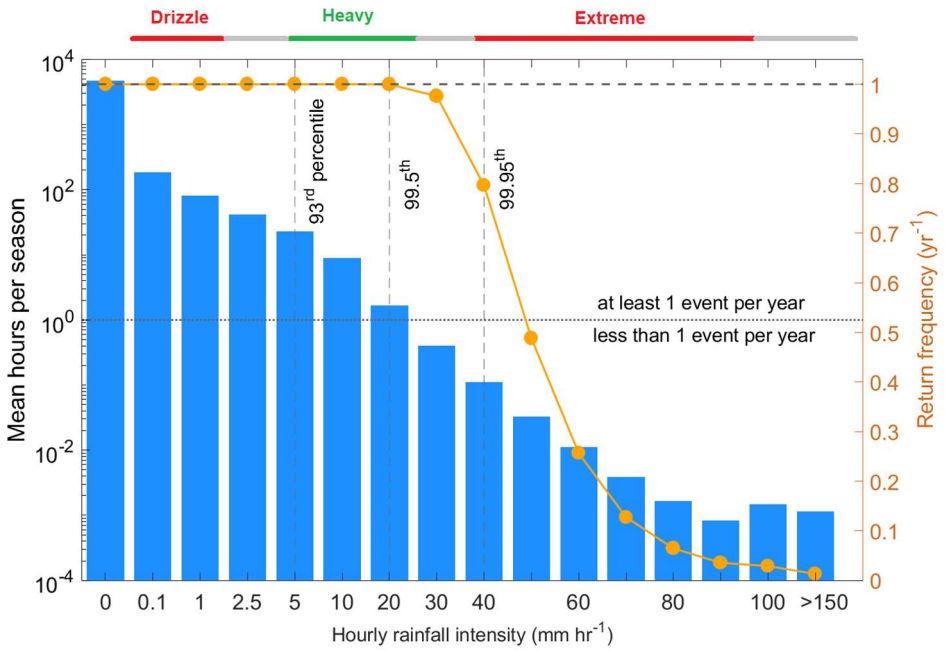

Figure 2: Frequency distribution of hourly rainfall intensities. National average county-level number of exposure hours per season (blue bars) and estimated national return frequency (yellow curve) for each hourly rainfall intensity bin over 2002-2017. Fine dotted line represents a once-per-year occurrence (mean hours per season of 1), such that bars above the line occur annually on average while bars below the line occur less than once per year. For the return frequency, a value of 1 (horizontal dashed line) indicates an event that occurs in every year for each county in the sample. Vertical dashed lines denote the indicated percentiles of climatological rainfall intensity.

Our analysis thus reveals a pattern of yield responses to rainfall intensity that varies substantially across the range of hourly intensities and is broadly consistent between the two crops. The estimated magnitude of yield responses to drizzle and heavy rainfall are at least as large as those to the more widely-studied seasonal total rainfall and multi-day extremes (Fig. 3). Crucially, we find positive or statistically insignificant yield sensitivities to annual maxima of hourly and daily rainfall (Fig. 3), likely because these measures capture beneficial heavy hourly intensities (E. Vogel et al., 2019; Zhu & Troy, 2018) (the mean national maximum hourly rainfall is 29mm hr^{-1}, Fig. 2, Appendix A Fig. 6). These findings underline the importance of accounting explicitly for sub-daily intensity in understanding and projecting the impact of rainfall on crops, as simple annual

maxima or percentile-based definitions may conceal crucial complexities and non-linear responses (Li et al., 2019; Urban, Roberts, et al., 2015; E. Vogel et al., 2019; Zhu & Troy, 2018).

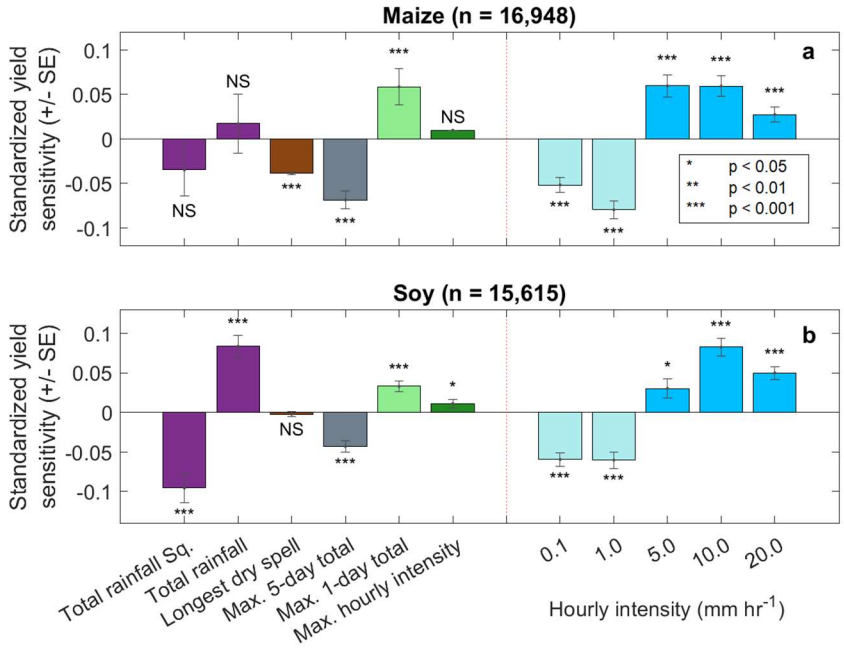

Figure 3: Crop yield sensitivity to rainfall distribution across timescales. Yield sensitivity estimates (±SE) to five measures of sub-seasonal rainfall distribution and select hourly intensities over 2002-2017 for a) maize, and b) soy. Sub-seasonal measures include seasonal total rainfall (mm), duration of the longest dry spell (days), and seasonal maxima of 5-day, 1-day, and hourly total accumulations (mm). Sensitivities are standardized to enable comparison among measures of differing units and variances. All p-values are two-sided and NS denotes coefficients $P > 0.05$.

Because we control for seasonal total rainfall, our estimated yield sensitivities reflect the yield impact of an incremental hour at a given rainfall intensity aside from its contribution to integrated moisture conditions. Our results thus suggest that heavy rainfall benefits crops because of its intensity, not merely because it contributes greater moisture than lower intensities. The significant benefits to crop yields from zero rainfall hours are consistent with this interpretation (Fig. 1): given the seasonal total rainfall control and the fixed total number of hours per growing season, each

incremental dry hour reduces the incidence of damaging drizzle and increases that of beneficial heavy rainfall (Fig. 1).

Regional differences in the pattern of yield response to rainfall intensity suggest that heavy rainfall benefits yields by providing moisture that is more plant-available than drizzle (Dastane, 1978; Van Elewijk, 1989). A higher fraction of heavier rainfall infiltrates the root zone, while a higher fraction of drizzle evaporates from the canopy, evading the crop. By this logic, heavy rain would offer a greater advantage to more moisture-limited crops. Indeed, we find contrasting yield responses to drizzle versus heavy rainfall consistent with the national pattern in the more moisture-limited northeastern and western portions of our study region, but not in the wetter southeast where heavy rainfall is ~25% more frequent (Appendix A Fig. 2, Appendix A Table 3, see Methods). Consistent with this potential mechanism, we find a weaker contrast between drizzle and heavy rainfall effects on yield in more heavily irrigated counties (Appendix A Fig. 3). The damaging effect of drizzle most likely reflects a missed opportunity to receive heavy rainfall, but may also arise partly from conditions conducive to foliar fungal pathogens (Harvell et al., 2002; Munkvold, 2003). Further research into interactions between rainfall intensity and the canopy-soil continuum may clarify the mechanism behind the contrasting impacts of heavy rainfall and drizzle.

In contrast to rare damaging extremes, drizzle and heavy rainfall occur essentially every year for each county in our sample (Fig. 2). To account for the variable incidence of differing rainfall intensities, we estimate the integrated seasonal yield sensitivity by weighting the per-hour sensitivities (Fig. 1) by the average seasonal total exposure hours for each intensity bin (Fig. 2, Appendix A Table 2, see Methods). Despite large per-hour sensitivity to extreme rainfall, the magnitude of the integrated seasonal sensitivity to heavy rainfall and drizzle (order 1-10bu ac^{-1}) exceeds that of extremes (order 0.01-0.1bu ac^{-1}) due to their relative commonness (Fig. 2, Fig. 4a-

b, Appendix A Table 2). In the current climate, we estimate a combined net negative yield impact from the hourly rainfall intensity distribution (2.2% of the mean national yield for maize and 1.6% for soy), with the dominant negative influence of drizzle only partly offset by the benefit of heavy rainfall (Fig. 4c-f). This indicates sup-optimal hourly rainfall distribution in the current climate.

In a warming climate, heavy and extreme rainfall events are expected to intensify because the saturation vapour pressure of air increases by ~7%/K, boosting precipitable water in the atmosphere (O'Gorman & Schneider, 2009; Westra, S., Fowler, H. J., Evans et al., 2014). However, rainfall intensification may exceed this scaling as condensation and latent heating enhance convection (P. Berg et al., 2013; Lenderink & Van Meijgaard, 2008), an effect which may be amplified for higher rainfall intensities (Chou et al., 2012; Prein et al., 2017). We project the change in net intensity effects under three idealized intensification scenarios derived from recent empirical and modeling studies: uniform low- and high-change (7 and 14%/K) across the intensity distribution (P. Berg et al., 2013; Lenderink & Van Meijgaard, 2008), and amplified change increasing with intensity from 7-40%/K (Chou et al., 2012; Kendon et al., 2014; Prein et al., 2017) (Appendix A Fig. 4, see Methods).

To assess the implications of hourly rainfall intensification for crop yields under climate warming, we apply the scaling factors for each scenario to intensities ≥5mm hr^{-1} under idealized warming of 1, 2, and 4K compared to present. We keep all other variables constant to isolate the impact of rainfall intensification. We find that under all three scenarios, crop yields increase meaningfully with intensifying hourly rainfall (Fig. 4c-d), primarily due to increased incidence of beneficial heavy events (Fig. 4e-f, Appendix A Fig. 4). In response to rainfall intensification from 2K warming, we project yield increases ranging from 0.9-2.1% across scenarios for maize and 1.3-2.5% for soy, approximately equivalent to recent harvests of Ethiopian maize and Russian soy.

Soy yields increase by 0.7% and maize yields decrease by 0.6% under the amplified scenario with 4K warming, the worst-case among the three scenarios due to greatest rises in damaging extremes (Fig. 4e-f, yellow curve). Our projections thus suggest that, on average, yields will most likely benefit slightly from rainfall intensification itself. However, this yield boost would only partly offset larger expected losses from heat stress (~10-30% for maize and ~0-15% for soy under 2K warming (Zhao et al., 2017)).

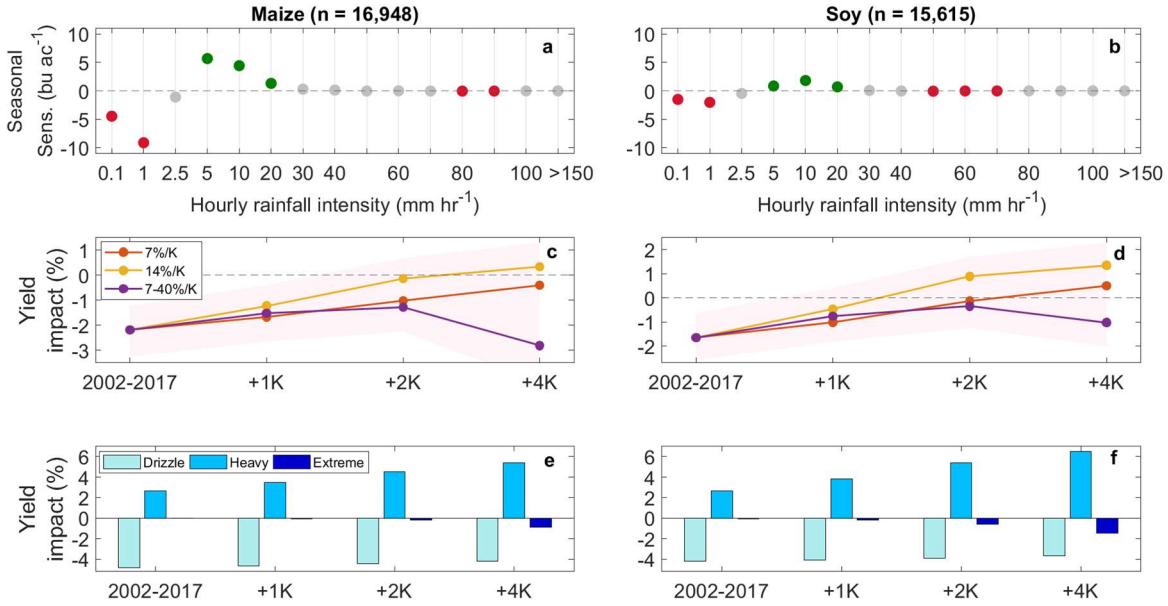

Figure 4: Current and projected future net yield impacts of hourly rainfall intensity. a-b) Integrated seasonal yield sensitivity for a) maize and b) soy, estimated by weighting the per-hour sensitivity by total exposure hours. c-d) Net impacts across all intensities on c) maize and d) soy yields under the 2002-2017 climate and for 1, 2, and 4K warming for 3 rainfall intensification scenarios: low-change (red), high-change (yellow), and amplified (purple). Shaded area shows the 90% confidence interval accounting for regression and scenario uncertainties. Net impacts are presented as percentages of the national mean yield. e-f) Same as c-d for the 14%/K scenario, but with yield impacts partitioned by intensity zone. For other scenarios, see Appendix A Fig. 5.

3) Conclusions

Several limitations of our study should be noted. First, although we focus on United States maize and soy as globally-important and widely-cultivated crops, attention to other crops and regions

may yield important insights into the ecophysiology and generalizability of our results. Second, while our analysis focuses on the full growing season, future work may investigate the importance of the duration, timing, and sequences of hourly rainfall, especially relative to crop growth phases (de Bruyn & de Jager, 1978) and regionally-varying growing seasons. Third, our method precludes projecting impacts due to unprecedented rainfall intensities and changes in the temporal and spatial structure of rainfall events. Interactive effects of changing heat, rainfall intensity, and seasonal total rainfall on crop yields also merit further attention. Finally, variables such as hail and wind, pests and disease, soil characteristics (Li et al., 2019), and antecedent moisture (Urban, Roberts, et al., 2015) are unavailable at sufficient spatial resolution for inclusion in our analysis, but likely compound or mediate the yield responses and may explain their regional variation.

We draw the following three overall conclusions from our study. First, rainfall intensity exerts an important influence on crop yields that varies substantially across the range of hourly intensities. Yields are reduced by drizzle but benefit from heavy rainfall, with damages only from exceptionally extreme events. Second, although extremes are severely damaging to crops, their rareness limits their overall influence on yields. As a result, crops are most responsive overall to drizzle and heavy rainfall rather than rare extremes. Third, rainfall intensification will on average benefit rather than harm crop yields, as damaging extremes remain much rarer than heavy rainfall under most plausible climate change scenarios. These benefits will not, however, outweigh expected losses from higher temperatures.

Our findings may help identify new opportunities for climate-adaptive crop management and improved modeling. For instance, we propose potential mechanisms behind the contrasting yield response to drizzle and heavy rainfall that, if corroborated, may help refine optimal sowing densities for both the current and future climate. Further, incorporating rainfall intensity effects

into crop models may enhance their experimental and predictive value (van der Velde et al., 2010). Most fundamentally, our results suggest that beyond extreme events, the crop yield response to more common rainfall intensities merits further attention.

4) Methods

We employ the Stage IV gridded mosaic of radar-derived hourly rainfall data for the continental United States at 4km resolution, obtained for 2002-2017 from the National Center for Environment Prediction (NCEP) (Lin, 2011). The Stage IV data are bias-corrected and quality-controlled using gauge-based observations. To the best of our knowledge, this is the first application of radar-derived data to analyze the impact of hourly rainfall on crop yields. Annual county-level maize and soy yield data were compiled from USDA National Agriculture Statistical Survey Quick Stats (USDA, n.d.). Daily temperature data were obtained from NCEP CPC's observational gridded dataset at 0.5-degree resolution. We also use daily 1-km gridded total incident surface shortwave radiation data from Daymet (Thornton et al., 2016). All datasets supporting the results of this paper are freely available from the references and links listed in Appendix A Table 4.

All sub-county and sub-seasonal scale data were aggregated to the seasonal and county scales to correspond with the annual county level yield data, which constituted the limiting spatial and temporal sampling resolution in the dataset. Temporal aggregation was based on the national average maize and soy growing season of March-September, i.e. the full envelope of the national growing season, to avoid erroneous exclusion of rainfall events that may result from downscaling available state-level crop progress data to the study resolution. Our reported pattern of yield sensitivity is also robust when using a growing season of March-August in the southern portion of the study region and April-September in the north (i.e. a 1-month shift), to broadly reflect variable

cropping seasons across the region (Appendix A Fig. 7). Daily temperatures were aggregated to the growing season via growing and killing degree days (GDD and KDD) as measures of aggregate exposure to beneficial and excessive heat, respectively (Butler & Huybers, 2013). We do not spatially downscale daily temperature observations used to compute GDD and KDD to the sub-county scale as temperature is less variable on fine spatial scales than rainfall. Our estimated sensitivity to KDD on a national average concurs with estimates based on station data (Butler & Huybers, 2013).

Hourly rainfall data were aggregated to the seasonal scale by computing intensity-binned histograms summarizing all hours in each growing season and county, and via summing across all hours for the seasonal total rainfall control. Fig. 2 shows the mean intensity-binned histogram averaged across all counties and years. The intensity binning scheme was chosen to reflect conventional meteorological classifications of rainfall (e.g., 0.1mm hr^{-1} as intensities above trace rainfall, and 2.5mm hr^{-1} to represent the upper limit of drizzle intensities), and results are robust to varying bin widths and centers (Appendix A Figures 6 and 8). The occurrence of extreme rainfall in our sample was relatively uniform in time over 2002-2017 (Appendix A Fig. 9). To match the county-level spatial resolution of the yield data, all final derived temperature and rainfall measures were aggregated to the county scale by averaging over all grid cells within each county. Finally, the spatial domain of the analysis was limited to counties east of the 104th meridian, as the density of radar stations west of this limit dropped sufficiently to raise concerns about data quality. The region included in the analysis comprises the majority of US maize and soy production areas.

To examine effects on crop yields due to specific hourly rainfall intensity, we apply a linear fixed-effects multiple regression model of the form:

$$\hat{y}_{i,t,b} = C_i + T_t + \beta_1 W_{i,t} + \beta_b H_{i,t,b} \quad (1)$$

where $\hat{y}_{i,t,b}$ is the predicted yield for year t in county i and intensity bin b. The first two terms are controls including a county-specific intercept vector (C_i) to account for time-invariant spatial yield heterogeneity and a national time fixed effect (T_t) to account for broader yield time trends (Appendix A Table 5). We account for long-term yield trends using a time fixed-effect rather than a linear or quadratic time trend, as the short time period of the analysis is insufficient for reliable trend estimation. The third term is a vector of seasonal weather measures $W_{i,t}$ (with corresponding coefficient vector β_1) including linear terms for GDD and KDD, which together capture the non-linear yield response to temperature, and a quadratic term for seasonal total rainfall predictors, which captures damaging yield effects of both drought and seasonal excess moisture.

We estimate the national mean sensitivity of county-level yields to specific hourly rainfall intensities as the coefficient β_b on seasonal total exposure hours to rainfall intensities in bin b ($H_{i,t,b}$) in Equation 1. This term regresses yields against each bin in the county-specific seasonal rainfall intensity histogram, resulting in a national mean estimate of county-level yield sensitivity per hour of exposure. We use names consistent with common meteorological conventions to identify the three intensity zones for which we find significant effects on yield, namely drizzle (0.1-1mm hr^{-1}), heavy (5-20mm hr^{-1}), and extreme (≥50mm hr^{-1}). The binning scheme for hourly rainfall intensity was also selected to match these meteorological conventions, and we show results under a finer binning scheme for drizzle in Appendix A Fig. 8. No significant effects on maize yields were found for rainfall above 100mm hr^{-1}, with similar but less pronounced patterns above 80mm hr^{-1} for soy (Fig. 1). The lack of sustained significant yield-damaging effects at these high intensities may reflect small sub-grid scale spatial extent of such rainfall events, insufficient sample size to detect a signal, or greater propensity for error in the Stage IV data at such high intensities (Krajewski W.F. & Smith J.A., 2002).

The inclusion of the $W_{i,t}$ term enables the isolation of intensity-specific yield effects, beyond their contribution to the total rainfall. Sensitivities to $W_{i,t}$ terms are reported in Appendix A Table 1 and are broadly consistent across bins. The model has r^2 of 0.75 for maize and 0.76 for soy. Occurrence of each rainfall intensity is correlated to varying degrees with both extreme heat and seasonal total rainfall (Appendix A Fig. 1)[20]. However, we do not find a coherent relationship between the pattern of observed yield sensitivity to hourly rainfall intensity and the correlation among these variables. KDD, which reflects detrimental heat extremes, is most positively correlated with moderate rainfall intensity ($r \sim 0.2$), for which positive yield effects are observed, and most negatively correlated with drizzle ($r \sim -0.5$), for which yield effects are negative. Meanwhile, correlation between KDD and extreme rainfall intensities is small ($r < 0.2$). Similarly, total rainfall is positively correlated with all non-zero rainfall intensity bins, and the peak correlation between 2.5 and 10 mm hr^{-1} ($r \sim 0.9$) is not consistently aligned with the observed zones of yield sensitivity. Collinearity between rainfall intensity and total rainfall thus cannot explain observed yield responses to intensity, suggesting independent effects of rainfall intensity on yields. Reported yield sensitivities are robust to including a linear term for total seasonal incident shortwave radiation in equation 1 as an explicit control for solar radiation (Appendix A Fig. 10).

Our model is analogous to that in ref. 1, except that we estimate yield sensitivity to each intensity bin separately rather than additively to eliminate the risk of type II errors from standard error inflation due to collinearity between adjacent bins (the r^2 between adjacent bins is about 0.5, generally <0.1 in the second bin, and approaching 0 beyond Appendix A Fig. 7). Observed distinct zones of sensitivity for drizzle, heavy, and extreme rainfall are separated by more than the radius of considerable correlation (~2 bins, $r^2 < 0.1$). Based on this separation, we consider

exposure hours among identified zones of significant sensitivity to be independent. Since adjacent bins within zones are not independent, however, we do not strongly interpret differences or trends in coefficient magnitudes within the zones.

To test the influence of collinearity between the rainfall intensity zones on the estimated yield sensitivities, we conduct a post-hoc re-binning of the drizzle, moderate, and extreme significant impact zones into a single model (in contrast to the individual estimation in equation 1). The model is of the form:

$$\hat{y}_{i,t} = C_i + T_t + \beta_1 W_{i,t} + \beta_D D_{i,t} + \beta_H H_{i,t} + \beta_E E_{i,t}$$

where *D*, *H*, and *E* represent county total seasonal exposure hours in the drizzle, heavy, and extreme zones of significant impact (summed across bins within each zone), with corresponding coefficients from which sensitivity is inferred (Appendix A Fig. 6). The estimated yield sensitivities to each zone are consistent with those estimated using equation 1 (Fig. 1), suggesting limited influence of collinearity between rainfall intensity zones on the results.

Hourly rainfall intensity percentiles are estimated as the fractional rank of a given rainfall intensity within the national mean intensity distribution excluding zero-rainfall hours, averaged across all counties (Fig. 1, Fig. 2). National mean return frequency is estimated as the ratio of the number of county-years with non-zero exposure hours to the total county-years in the sample for each intensity bin (Fig. 2, yellow curve), i.e. only accounting for binary occurrence and not the number of events per season. This measure reflects the rareness of heavy and extreme rainfall intensities on a national average relative to the common events that occur each year and in each county.

The regional analysis divides the spatial domain of the dataset into 3 regions with roughly equal sample sizes, with the west defined as west of the 93rd meridian, the northeast as east of the

93rd meridian and north of the 40th parallel, and the southeast as east of the 93rd meridian and south of the 40th parallel (Appendix A Fig. 2a). These regional boundaries correspond approximately to climatological rainfall contours, with seasonal mean rainfall ±SD of 660 ±200mm, 750 ±167mm, and 850 ±200mm in the west, northeast, and southeast, respectively. For this analysis, we applied the regression model in equation 1 limited to bins less than 50 mm hr^{-1} as sample sizes for extreme rainfall bins were insufficient for data stratification. Beyond this limitation, yield sensitivity to extremes likely differs regionally as well, for instance because the southeast experiences the most extremes among the regions (on average 47% of total extreme hours per season, Appendix A Fig. 2b) and may be somewhat more strongly represented in the national scale sensitivity estimates. The regional results reveal certain general patterns which likely mask spatial variability at the county scale, which we cannot explicitly analyze due to a limited time series (15-16 years) in the rainfall data.

Our stratification based on irrigated crop area (Appendix A Fig. 3) followed an analogous method to the regional analysis. We first computed the percent of harvested area that is irrigated for each county, averaged across available censuses (2002, 2007, 2012, and 2017), using data from USDA-NASS (Butler & Huybers, 2013). We excluded 5,706 counties with no available irrigation data from this analysis. We then stratified the sample of 11,242 counties using the irrigated area threshold of 5% (which resulted in two samples of similar size) and applied the regression model in equation (1) separately for the two groups.

For the comparison of hourly rainfall within overall growing season weather (Fig. 3), we applied 5 indicators of rainfall distribution across timescales based on CLIVAR climate extremes indicators(Karl et al., 1999): 1) seasonal total rainfall, 2) duration in days of longest dry spell, 3) maximum 5-day total rainfall, 4) maximum 1-day total rainfall, and 5) maximum hourly rainfall

(Fig. 3). We regressed county crop yields against the suite of sub-seasonal rainfall distribution measures using the equation:

$$\hat{y}_{i,t} = C_i + T_t + \beta_1 W_{i,t}$$

where $\hat{y}_{i,t}$ is the predicted yield for year t in county i and $W_{i,t}$ is the vector of rainfall distribution measures with corresponding coefficient vector β_1, from which yield sensitivities are inferred. As in equation 1, we controlled for temperature by including GDD and KDD in $W_{i,t}$ (these coefficient estimates omitted for clarity). To aid the comparison of estimated yield sensitivities across measures with differing units, we present dimensionless standardized coefficients of each measure (B_1), estimated by multiplying the absolute coefficient estimates by the ratio of weather-measure to yield standard deviations (national mean of the within-county time standard deviations, denoted $\overline{\sigma_W}$ and $\overline{\sigma_y}$, respectively):

$$B_1 = \beta_1 \frac{\overline{\sigma_W}}{\overline{\sigma_y}}$$

Various combinations of weather metrics were tested in candidate models to examine the robustness of coefficient sign and magnitude; individual indicator coefficients from candidate sub-models are generally consistent with the full model.

Our estimated yield sensitivities to the duration of the longest dry spell are consistent in sign and approximate magnitude with other recent estimates[4]. However, in contrast to ref's 2 and 4, we find significant negative yield response to the maximum 5-day total rainfall, likely because we control for seasonal total rainfall. This result thus likely reflects the yield-reducing influence of short-duration moisture excess, separate from the contribution of the multi-day rainfall extremes to seasonal moisture conditions. Standardized yield sensitivities to drizzle and heavy rainfall are comparable in magnitude to 5-day maximum rainfall and longest dry spell, whose impacts are

more broadly recognized in recent research. We conclude that daily and hourly maxima correlate positively with yields because they capture beneficial heavy rainfall, rather than damaging extremes. The mean national maximum hourly rainfall is 29mm hr^{-1}, which corresponds to insignificant yield responses between the heavy and extreme rainfall intensities. Further, maximum daily rainfall most strongly correlates with incidence of heavy rainfall ($r \sim 0.5$-0.6) rather than extremes ($r \sim 0.1$-0.4, Appendix A Fig. 1).

We estimate integrated seasonal sensitivities (Fig. 4a-b) by weighting the β_b sensitivities by the hourly exposure $H_{i,t,b}$ averaged nationally over 2002-2017 for each bin (Fig. 2, blue bars). For each intensity bin, this procedure converts per-hour yield sensitivities into estimated total yield impacts, accounting for the total number of exposure hours across the growing season. Because adjacent bins within each intensity zone with significant yield effects cannot be treated as independent (Appendix A Fig. 11), we compute net intensity effects by first averaging integrated seasonal yield sensitivities for drizzle, heavy rainfall, and extreme bins separately, and finally summing the average sensitivities across the three independent intensity zones (Fig. 4c-f).

We project a range of plausible future hourly rainfall intensification using three scenarios of rainfall intensity scaling with mean temperature, representing current empirical and modeling uncertainty over the response of convective and mesoscale dynamics to warming. We apply the scenarios to intensities ≥5mm hr^{-1} consistent with reported distinct temperature scaling of high-percentile rainfall intensities with temperature beginning between the 90^{th} and 99^{th} percentiles (Lenderink & Van Meijgaard, 2008; Westra, S., Fowler, H. J., Evans et al., 2014). The uniform low-change scenario reflects a simple scaling of high-percentile rainfall intensity with precipitable water equal to the 7%/K increase in saturation vapour pressure, governed by the Clausius-Clapeyron relation. The high-change and amplified scenarios reflect potential additional rainfall

intensification mainly due to convective enhancement and associated horizontal moisture convergence from latent heating in the ascending air column. Under the high-change scenario, a uniform 14%/K intensification (double the Clausius-Clapeyron scaling) is applied (P. Berg et al., 2013; Lenderink & Van Meijgaard, 2008), while in the amplified scenario, intensification is linearly increased from 7%/K at 5mm hr^{-1} to 40%/K at 90mm hr^{-1} (Chou et al., 2012; Kendon et al., 2014; Prein et al., 2017). Based on our yield analysis, this final scenario represents the most disadvantageous plausible scenario for crops, serving as a limiting case for projected net yield impacts.

We project future changes in the incidence of heavy and extreme hourly rainfall (≥5mm hr^{-1}) by shifting the observed 2002-2017 frequency distributions by the intensity scaling factors following:

$$I_{bin,scen}^{future} = I_{bin}^{2002-2017}(1 + f_{scen})^{\Delta T}$$

Future bin-center intensities ($I_{bin,scen}^{future}$) are projected by increasing the observed 2002-2017 bin-center intensities ($I_{bin}^{2002-2017}$)by the scaling factors (f_{scen}) under assumed mean temperature increases of 1, 2, and 4K relative to the present day (ΔT). The increased incidence at the original 2002-2017 bin centers are then estimated by linearly interpolating from the shifted distributions (Appendix A Fig. 4). Our method thus preserves the observed relative decay in frequency of rainfall with increasing intensity (Fig. 2). The projected intensification results in 4-27 additional heavy and extreme rainfall hours per season, depending on the scenario and warming magnitude.

To isolate the impact of changing rainfall intensity, we conserve the climatological total rainfall hours by subtracting the projected increase in heavy and extreme hours from the 2002-2017 drizzle hours, consistent with projected declines in the frequency of light precipitation under mean warming (Chou et al., 2012; Lau et al., 2013). Importantly, while seasonal total rainfall,

KDD, and GDD are likely to change in the future, we keep these variables constant in our yield projections to isolate the impact of rainfall intensification. Our projected yield changes from rainfall intensification should thus be interpreted as only one component of climate-induced yield changes, which must be considered in the context of impacts from changing extreme heat and drought.

Projected future yield impacts from the intensification scenarios are finally estimated by re-weighting the intensity-specific per-hour sensitivities by the projected intensified hourly rainfall distributions, as for Fig. 4a-b. This approach assumes that per-hour yield sensitivities estimated over 2002-2017 remain constant into the future. Projected net yield changes are estimated as the sum of the intensity-zone mean impacts (Fig. 4c-d). To represent uncertainty in these estimated impacts, we include an estimated 90% confidence interval from an ensemble of projections in which intensity-specific yield sensitivities are permuted to reflect estimation uncertainty. The permutation involves generating 1000 pseudorandom yield sensitivities from a normal distribution with mean equal to the coefficient estimate and standard deviation equal to the standard error of the estimate. We recompute the net impact using the 1000 sensitivity permutations for each scenario to yield an ensemble of 3000 impacts projections, the 5^{th} to 95^{th} percentiles of which we include as a shaded area in Fig. 4c-d. We also present partitioned impacts for each intensity zone by averaging impacts across bins in the drizzle, heavy, and extreme zones (Fig. 4e-f for the 14%/K scenarios, other scenarios shown in Appendix A Fig. 5). Appendix A Figure 12 provides a visualization of the methods, data, and assumptions employed in this study.

Future changes in hourly rainfall intensity may not be uniformly distributed across the growing season, with potential consequences for daily to multi-day rainfall statistics and their yield impacts. Such potential future changes in the temporal structure of rainfall across timescales may

alter the rainfall intensities that contribute most to extreme daily rainfall totals. For example, 1-day rainfall totals may become damaging to crops in the future if they are more strongly driven by short-duration extremes than at present (Fig. 3). Future research may investigate the influence on crop yields of variation in the time structure of rainfall from hourly to seasonal scales, especially as observational, theoretical, and model basis for reliably projecting these changes improves.

Our results provide an example of a climate-sensitive system essential to human health and wellbeing that is sensitive to hourly rainfall intensity. While the incorporation of hourly rainfall data into climate risk assessment is presently common in hydrological modeling and engineering[9], our results suggest that rainfall on this timescale merits further attention in crop research and in plant science and ecology more generally. Finally, our results highlight the value and applicability of increasing climate model resolution, expert elicitation, and improved spatial and temporal completeness of observational and reanalysis data for understanding and projecting the shifting distribution of hourly rainfall under climate warming and the associated impacts on human and natural systems.

Appendix A

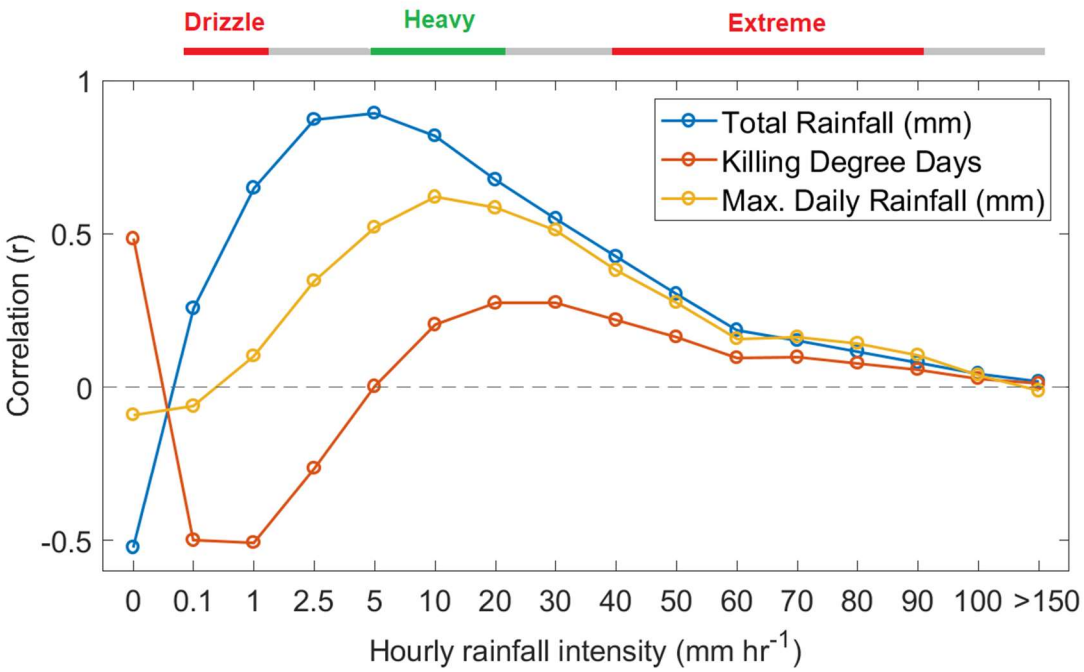

Appendix A Figure 1: Correlation between the incidence of hourly rainfall intensities and seasonal total rainfall, extreme heat, and maximum daily rainfall. Correlation coefficient of seasonal occurrence (hours) of rainfall of given intensities with seasonal total rainfall, killing degree days, and maximum daily rainfall, with annotated zones of significant positive (green) and negative (red) yield response ($P < 0.05$).

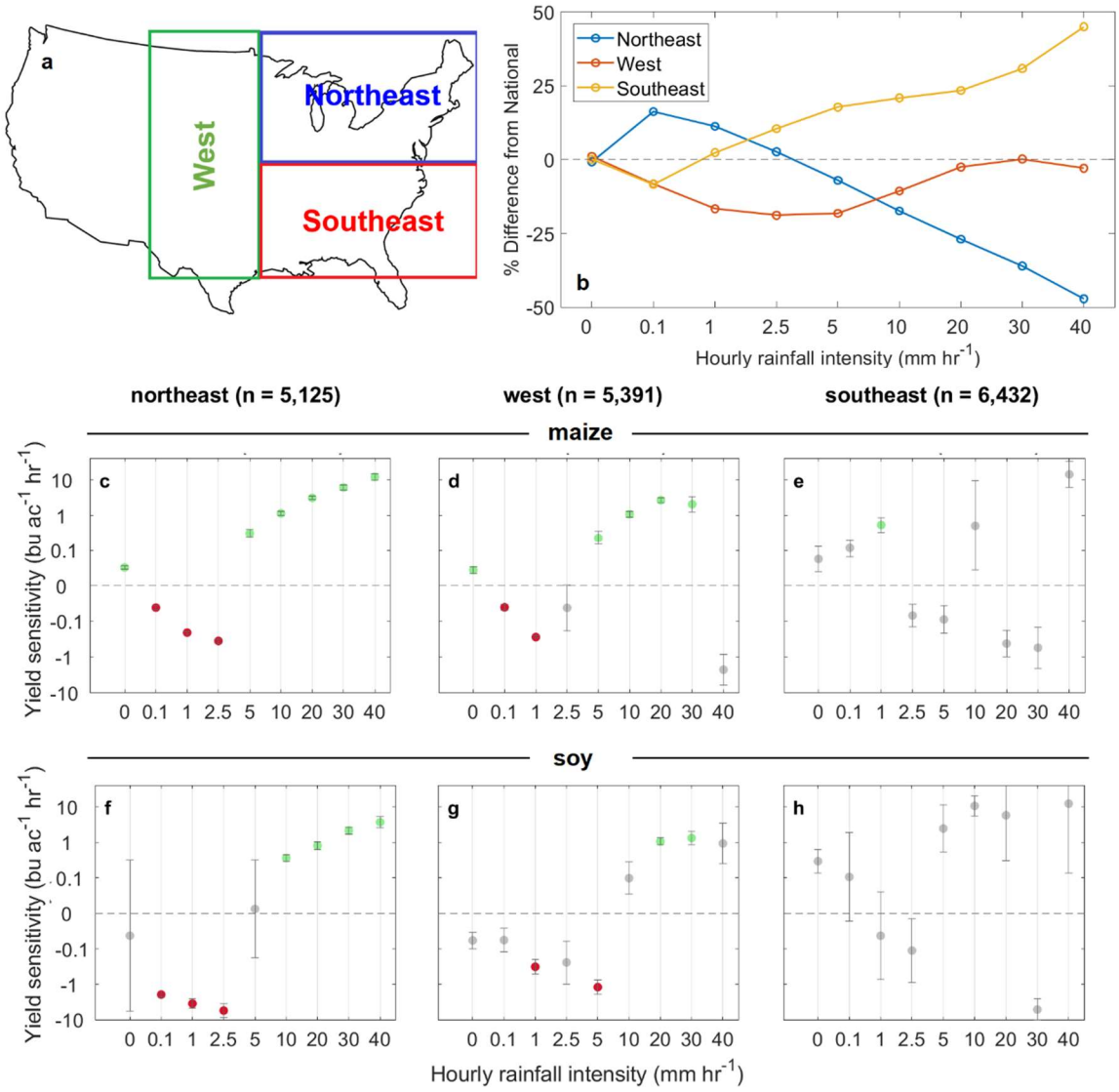

Appendix A Figure 2: Regional maize and soy yield sensitivity to drizzle and moderate rainfall. a) Schematic map of regional boundaries. Northeast is defined as latitude ≥40°N, east of 93°W, southeast as latitude <40°N, east of 93°W, and west as 93 to 104°W. b) Regional variation in the incidence of differing rainfall intensities, as percent deviation from the national mean incidence (Fig. 2). Regional mean county-level yield sensitivity (±SE) to hourly rainfall intensity per hour of exposure for c-e) maize, and f-h) soy. Extreme rainfall bins >40 mm hr^{-1} are omitted due to insufficient data for sample stratification. Sensitivities are plotted on symmetric logarithmic axes, with correspondingly transformed relative error bars. Green and red points indicate significant positive and negative sensitivities (two-sided $P < 0.05$).

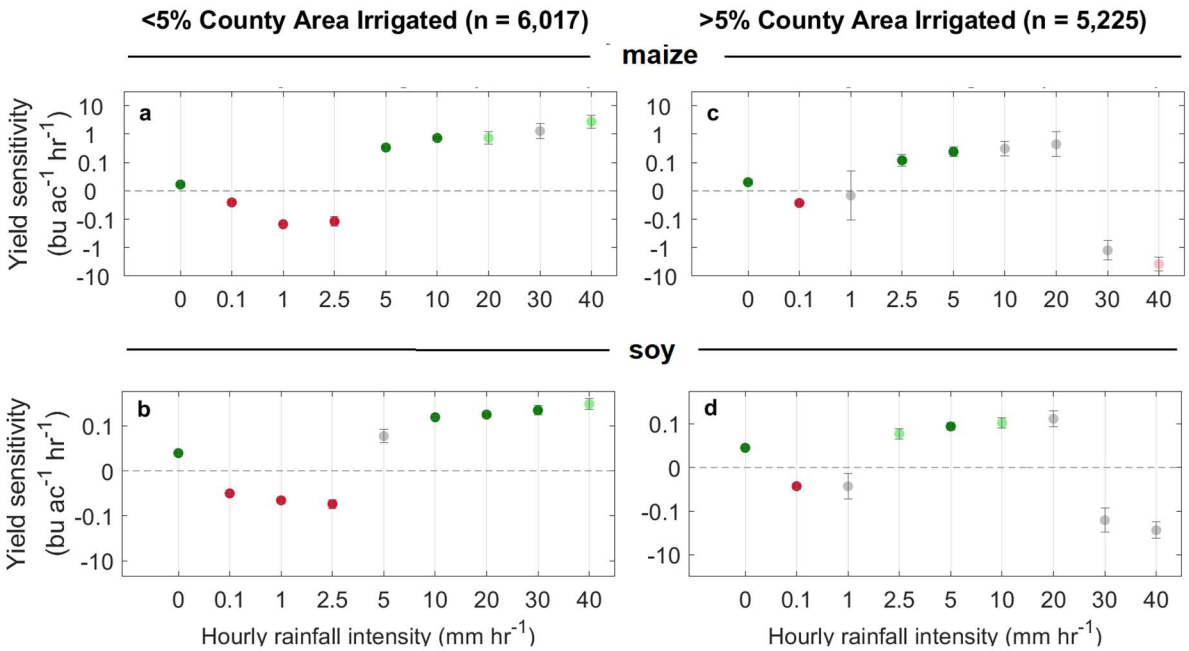

Appendix A Figure 3: Maize and soy yield sensitivity to drizzle and moderate rainfall among counties with more and less extensive irrigation. Mean county-level yield sensitivity (±SE) to hourly rainfall intensity per hour of exposure for a-b) counties with less than 5% of crop area irrigated, and c-d) counties with more than 5% crop area irrigated (see Methods). Extreme rainfall bins >40 mm hr^{-1} are omitted due to insufficient data for sample stratification. Sensitivities are plotted on symmetric logarithmic axes, with correspondingly transformed relative error bars. Dark green and red points indicate significant positive and negative sensitivities (two-sided $P < 0.05$), while pink and light green points denote weakly significant effects (two-sided $P < 0.1$). The total counties analyzed is less than for the other analyses as irrigation data is not available for all counties.

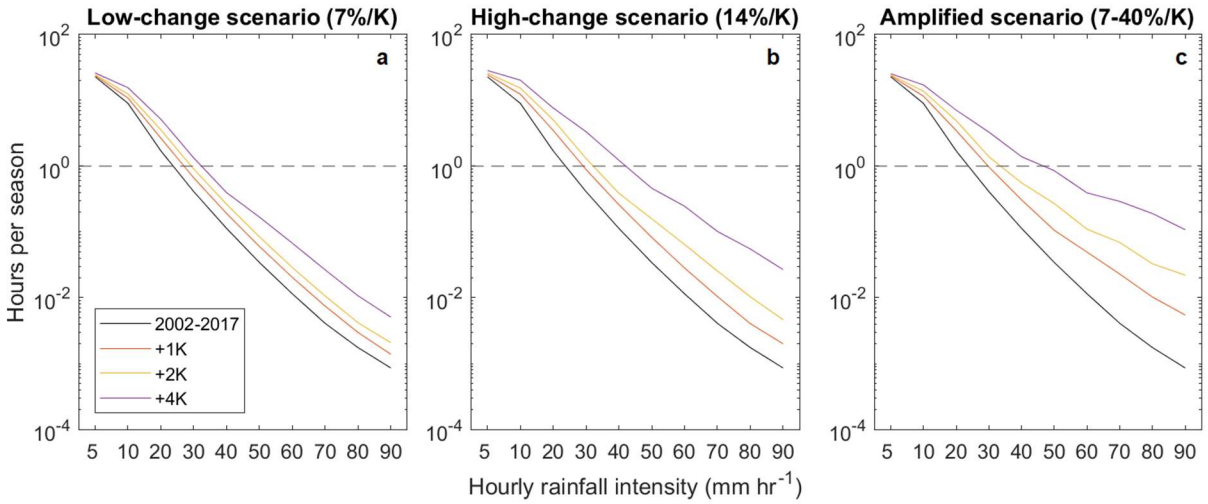

Appendix A Figure 4: Projected future incidence of heavy and extreme rainfall under climate warming. Intensified distributions of heavy and extreme hourly rainfall under idealized warming of 1, 2 and 4K projected by shifting the 2002-2017 baseline distribution (black curve, Fig. 2) under a) the uniform low-change scenario, b) the uniform high-change scenario, and c) the amplified scenario with greater intensification for higher intensities.

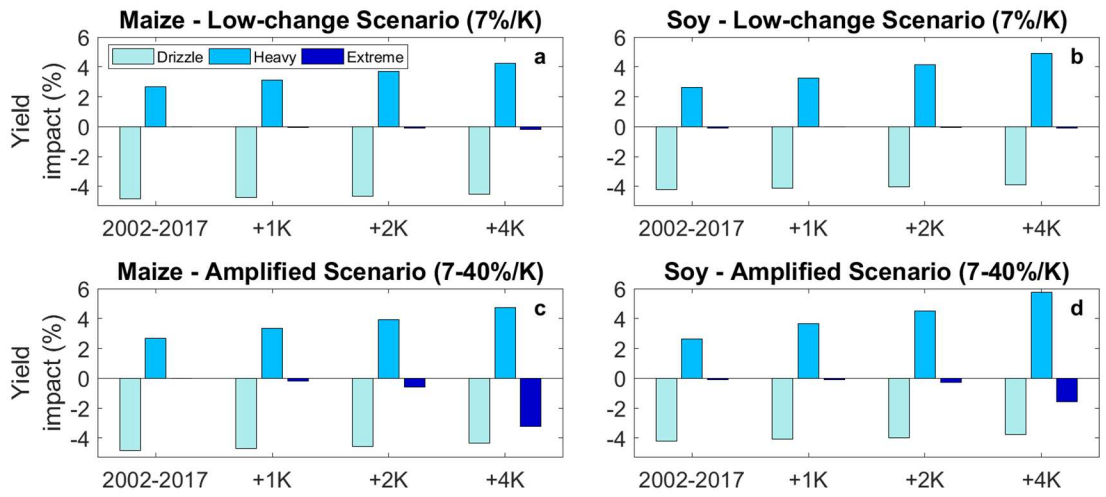

Appendix A Figure 5: Crop yield impact of low-change and amplified rainfall intensification scenarios under climate warming. Same as Fig. 4e-f, except for the a-b) low-change scenario, and c-d) amplified scenario.

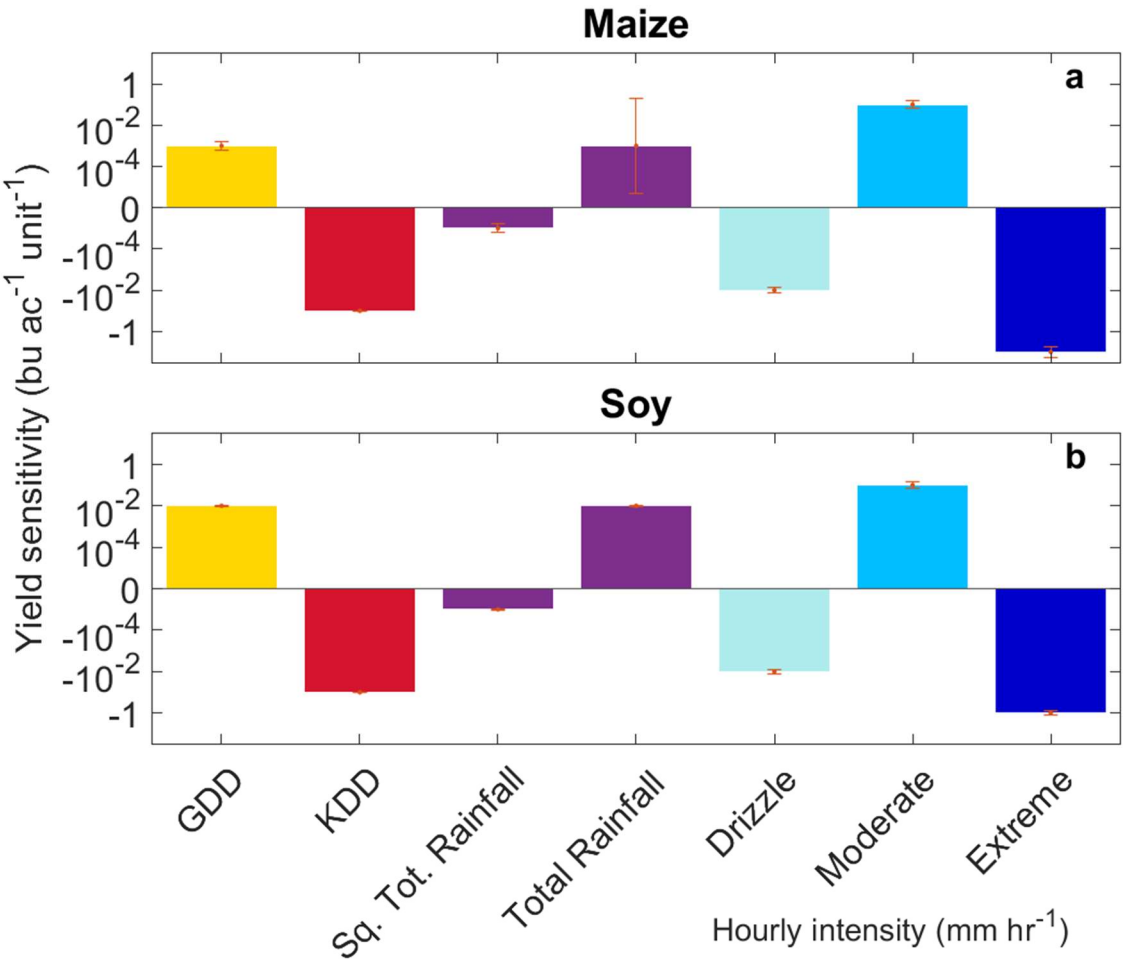

Appendix A Figure 6: Yield sensitivity to re-binned hourly rainfall intensity zones. a) Maize yield sensitivity estimates for a post-hoc model with re-binned drizzle, heavy, and extreme significant yield impact zones (in addition to heat and seasonal total rainfall terms), plotted on symmetric logarithmic axes. b) Same as a), but for soy. Error bars indicate relative standard errors of the coefficients rescaled to the logarithmic axes.

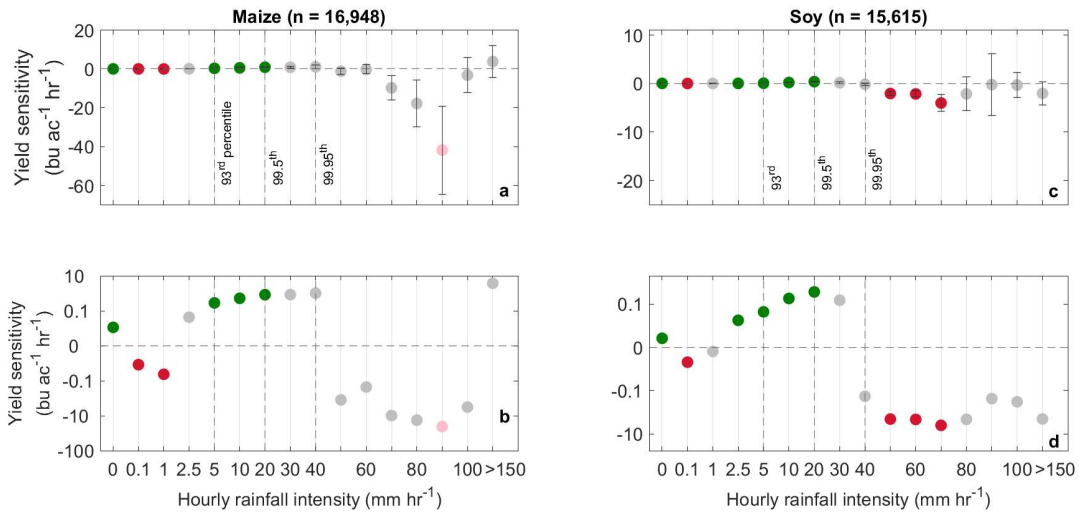

Appendix A Figure 7: Yield sensitivity to hour rainfall intensity using alternate growing season. Same as Fig. 1, but using a regionally-variable growing season (March-August in the southern portion of the study region, April-September in the north).

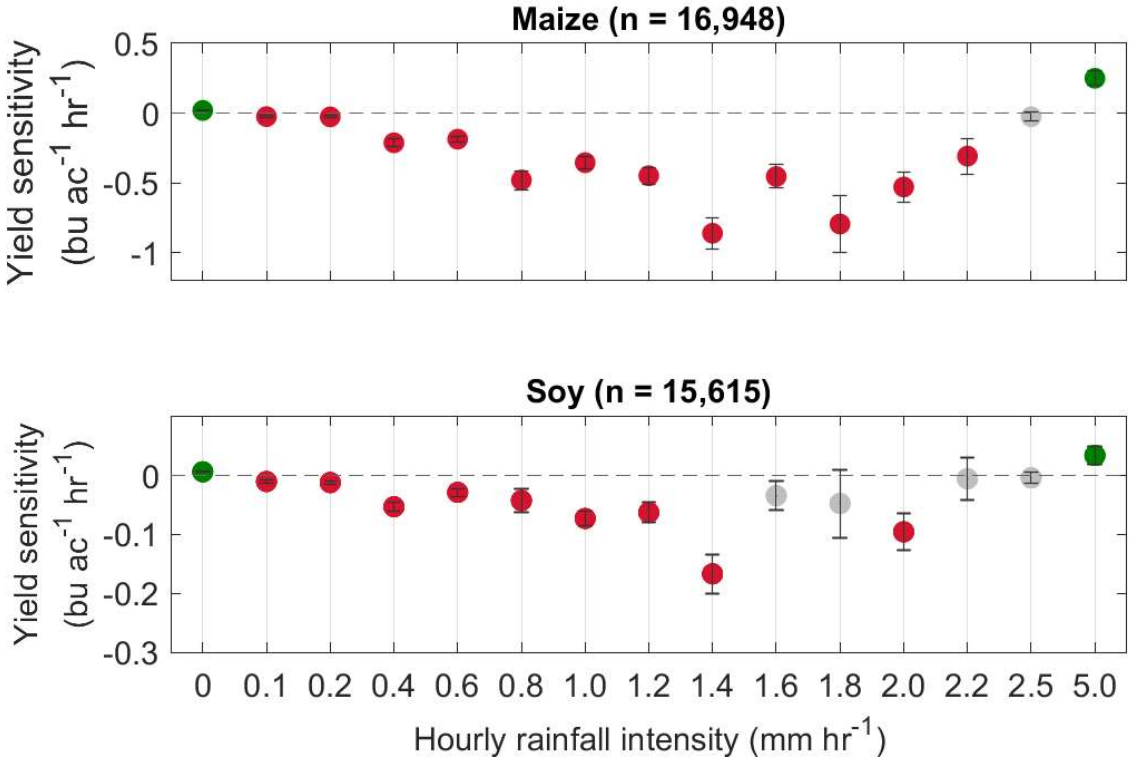

Appendix A Figure 8: A more detailed view of yield sensitivity to low-intensity rainfall. Same as Fig. 1a and c from 0 to 5.0 mm hr^{-1}, but with finer binning of rainfall intensities in the drizzle zone. The 0, 2.5, and 5.0 mm hr^{-1} bins are identical to those in Fig. 1.

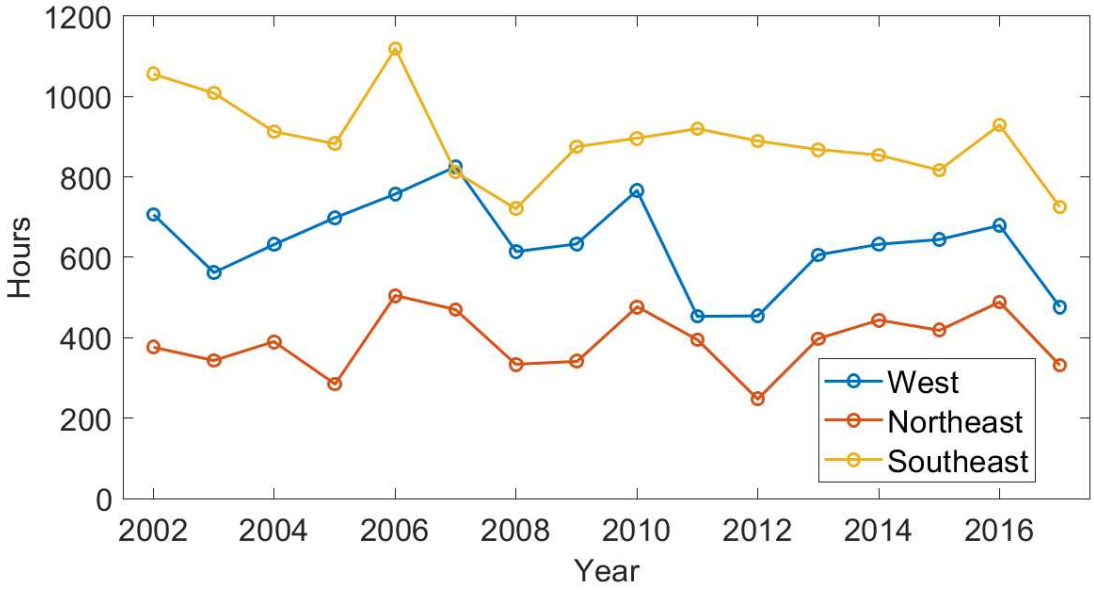

Appendix A Figure 9: Annual regional total incidence of extreme rainfall intensities. Total number of extreme rainfall hours (≥50 mm hr^{-1}) per year in the West, Northeast, and Southeast over 2002-2017. The extreme intensity threshold represents the envelope of intensities with significant negative yield effects on maize and soy.

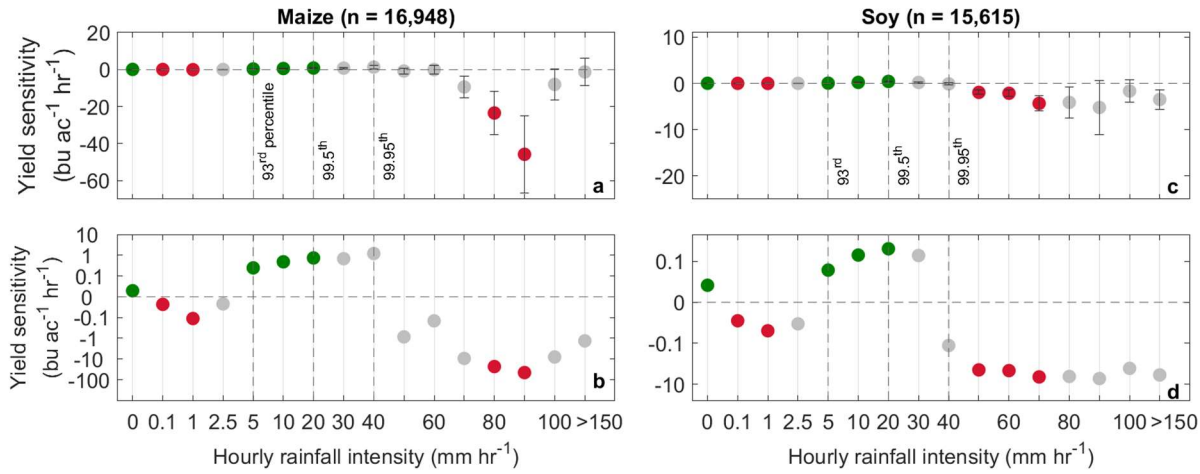

Appendix A Figure 10: Yield sensitivity to hourly rainfall intensity directly controlling for solar radiation. Same as Fig. 1, except for a model including a solar radiation term to examine potential influence of cloudiness on crop yield response to rainfall intensities (see Methods).

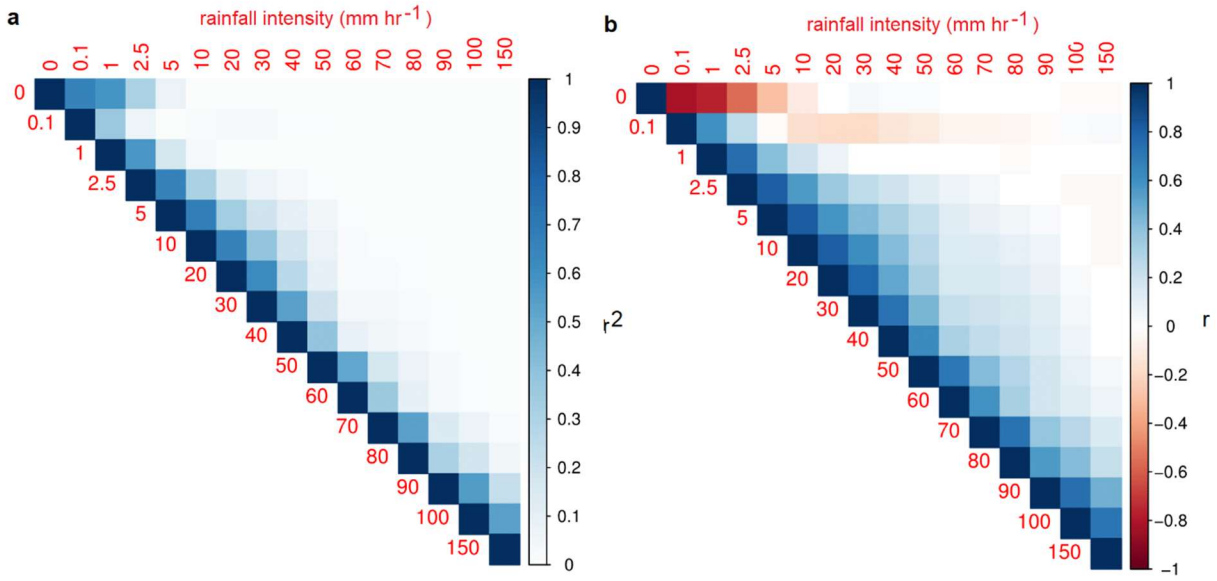

Appendix A Figure 11: Correlation in total seasonal occurrence between hourly rainfall intensity bins. a) Matrix of coefficient of determination (r^2) in exposure hours between rainfall intensity bins. b) Matrix of correlation coefficients (r) in exposure hours between rainfall intensity bins.

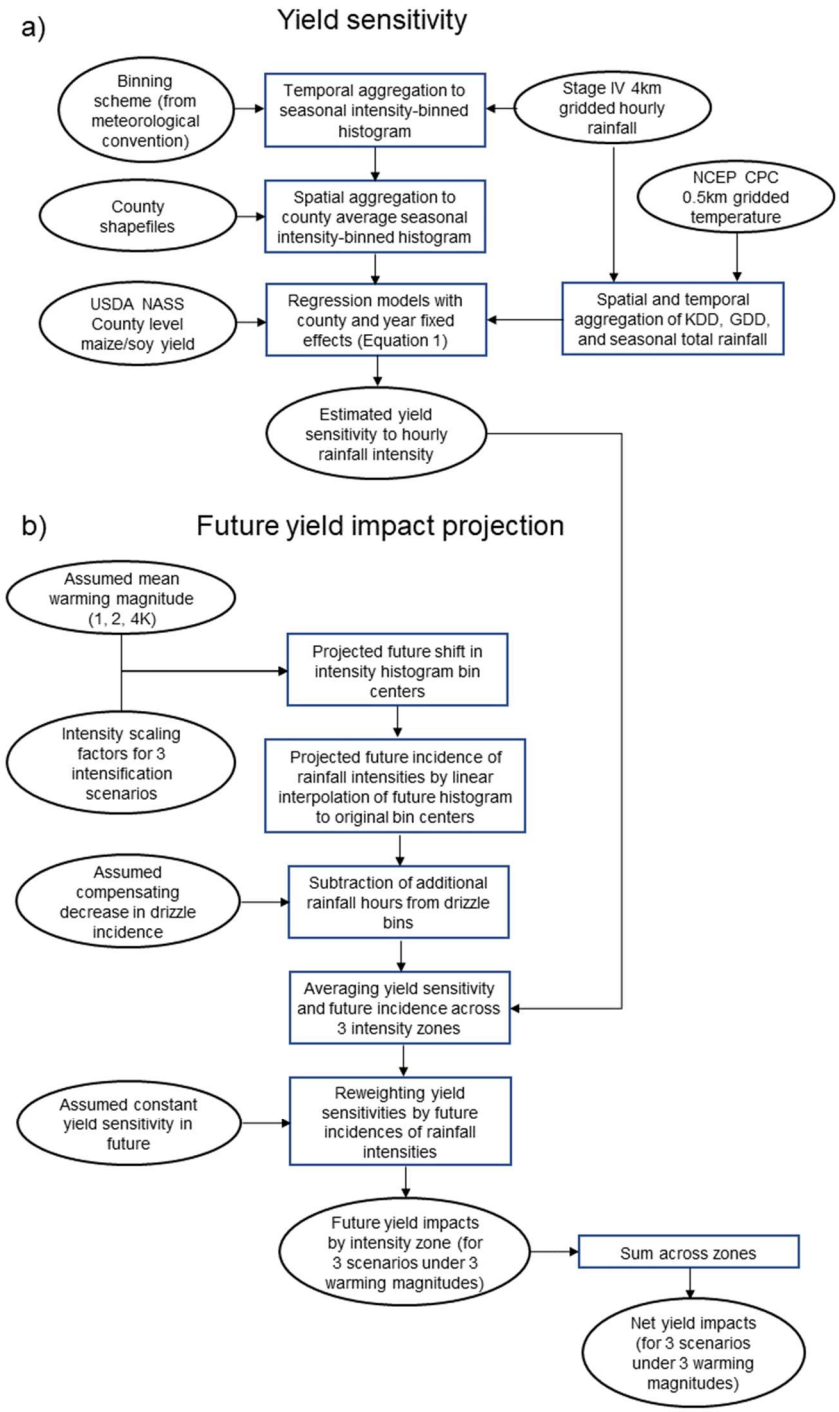

Appendix A Figure 12: Flowchart describing sequence of methods employed for a) yield sensitivity estimation and b) future yield impact projection, including data inputs and assumptions. Elliptical elements depict data and assumptions, while rectangular elements show computations.

Supplementary Table 1: Regression coefficients, standard errors, and p-values for yield sensitivity to hourly rainfall intensity, heat, and total rainfall.

	Intensity bin	GDD			KDD			Squared total rainfall			Total rainfall			Intensity bin exposure hours			non-zero
	(mm hr^{-1})	coefficient	SE	p =	coefficient	SE	p =	coefficient	SE	p =	coefficient	SE	p =	coefficient	SE	p =	county-years
Soy	0	1.13E-02	6.90E-04	2.28E-59	-5.41E-02	1.04E-03	<10E-10	-1.21E-05	8.08E-07	1.73E-50	2.32E-02	1.46E-03	2.79E-56	6.74E-03	8.41E-04	1.22E-15	15615
	0.1	1.16E-02	6.88E-04	5.73E-63	-5.44E-02	1.04E-03	<10E-10	-1.22E-05	8.09E-07	8.58E-51	2.25E-02	1.45E-03	1.20E-53	-7.93E-03	1.14E-03	3.32E-12	15615
	1	1.16E-02	6.89E-04	1.68E-62	-5.44E-02	1.04E-03	<10E-10	-1.21E-05	8.10E-07	2.22E-50	2.31E-02	1.48E-03	9.90E-55	-2.45E-02	4.23E-03	6.88E-09	15615
	2.5	1.17E-02	6.90E-04	9.16E-64	-5.45E-02	1.04E-03	<10E-10	-1.19E-05	8.10E-07	2.53E-48	2.19E-02	1.52E-03	5.20E-47	-1.12E-02	8.93E-03	2.08E-01	15615
	5	1.17E-02	6.89E-04	1.37E-64	-5.45E-02	1.04E-03	<10E-10	-1.17E-05	8.11E-07	8.56E-47	1.99E-02	1.57E-03	1.05E-36	3.70E-02	1.47E-02	1.19E-02	15615
	10	1.13E-02	6.90E-04	4.76E-60	-5.41E-02	1.04E-03	<10E-10	-1.15E-05	8.09E-07	1.68E-45	1.73E-02	1.55E-03	7.21E-29	2.00E-01	2.74E-02	3.32E-13	15615
	20	1.15E-02	6.89E-04	1.89E-62	-5.44E-02	1.04E-03	<10E-10	-1.20E-05	8.09E-07	9.56E-50	1.99E-02	1.47E-03	1.50E-41	4.07E-01	6.69E-02	1.15E-09	15611
	30	1.17E-02	6.89E-04	2.41E-64	-5.45E-02	1.04E-03	<10E-10	-1.20E-05	8.20E-07	4.52E-48	2.14E-02	1.45E-03	5.03E-49	1.90E-01	1.49E-01	2.02E-01	15247
	40	1.17E-02	6.89E-04	1.65E-64	-5.45E-02	1.04E-03	<10E-10	-1.17E-05	8.40E-07	6.93E-44	2.13E-02	1.47E-03	2.70E-47	-1.28E-01	2.64E-01	6.29E-01	12377
	50	1.17E-02	6.89E-04	2.10E-64	-5.44E-02	1.04E-03	<10E-10	-1.11E-05	8.26E-07	6.18E-41	2.06E-02	1.46E-03	8.84E-45	-1.96E+00	4.71E-01	3.08E-05	7470
	60	1.17E-02	6.89E-04	2.01E-64	-5.44E-02	1.04E-03	<10E-10	-1.14E-05	8.17E-07	3.50E-44	2.09E-02	1.45E-03	1.79E-46	-2.14E+00	6.58E-01	1.14E-03	3828
	70	1.17E-02	6.89E-04	1.68E-64	-5.45E-02	1.04E-03	<10E-10	-1.16E-05	8.12E-07	4.12E-46	2.12E-02	1.45E-03	6.15E-48	-4.34E+00	1.68E+00	9.66E-03	1856
	80	1.17E-02	6.89E-04	1.47E-64	-5.45E-02	1.04E-03	<10E-10	-1.18E-05	8.10E-07	1.27E-47	2.13E-02	1.45E-03	6.92E-49	-4.12E+00	3.32E+00	2.15E-01	948
	90	1.17E-02	6.89E-04	1.45E-64	-5.45E-02	1.04E-03	<10E-10	-1.18E-05	8.09E-07	4.71E-48	2.14E-02	1.45E-03	4.25E-49	-5.21E+00	5.87E+00	3.75E-01	516
	100	1.17E-02	6.89E-04	1.44E-64	-5.45E-02	1.04E-03	<10E-10	-1.18E-05	8.09E-07	4.31E-48	2.14E-02	1.45E-03	4.58E-49	-1.66E+00	2.39E+00	4.86E-01	429
	>150	1.17E-02	6.89E-04	1.38E-64	-5.44E-02	1.04E-03	<10E-10	-1.19E-05	8.09E-07	2.88E-48	2.15E-02	1.45E-03	2.46E-49	-3.49E+00	2.13E+00	1.02E-01	207
Maize	0	4.33E-03	2.34E-03	6.39E-02	-1.34E-01	3.29E-03	<10E-10	-6.39E-06	2.68E-06	1.70E-02	1.23E-02	4.80E-03	1.05E-02	1.95E-02	2.78E-03	2.06E-12	16948
	0.1	4.84E-03	2.33E-03	3.84E-02	-1.34E-01	3.30E-03	<10E-10	-6.57E-06	2.68E-06	1.44E-02	1.01E-02	4.77E-03	3.33E-02	-2.37E-02	3.96E-03	2.00E-09	16948
	1	4.91E-03	2.33E-03	3.52E-02	-1.35E-01	3.30E-03	<10E-10	-7.10E-06	2.68E-06	8.14E-03	1.56E-02	4.87E-03	1.36E-03	-1.12E-01	1.42E-02	4.42E-15	16948
	2.5	5.01E-03	2.34E-03	3.23E-02	-1.34E-01	3.30E-03	<10E-10	-5.27E-06	2.68E-06	4.93E-02	7.13E-03	5.00E-03	1.54E-01	-2.66E-02	3.09E-02	3.91E-01	16948
	5	5.25E-03	2.34E-03	2.47E-02	-1.34E-01	3.30E-03	<10E-10	-4.44E-06	2.68E-06	9.71E-02	-3.82E-03	5.10E-03	4.54E-01	2.49E-01	5.14E-02	1.23E-06	16948
	10	4.36E-03	2.34E-03	6.25E-02	-1.34E-01	3.30E-03	<10E-10	-4.72E-06	2.67E-06	7.74E-02	-3.11E-03	5.01E-03	5.35E-01	4.92E-01	9.50E-02	2.26E-07	16948
	20	4.86E-03	2.34E-03	3.74E-02	-1.34E-01	3.30E-03	<10E-10	-5.67E-06	2.68E-06	3.43E-02	3.32E-03	4.77E-03	4.85E-01	7.68E-01	2.33E-01	9.97E-04	16944
	30	5.08E-03	2.34E-03	2.96E-02	-1.34E-01	3.30E-03	<10E-10	-5.78E-06	2.71E-06	3.33E-02	5.79E-03	4.71E-03	2.19E-01	7.35E-01	5.15E-01	1.54E-01	16543
	40	5.14E-03	2.34E-03	2.80E-02	-1.34E-01	3.30E-03	<10E-10	-6.08E-06	2.77E-06	2.80E-02	6.64E-03	4.76E-03	1.63E-01	1.24E+00	9.16E-01	1.78E-01	13487
	50	5.09E-03	2.34E-03	2.94E-02	-1.34E-01	3.30E-03	<10E-10	-4.84E-06	2.73E-06	7.61E-02	5.40E-03	4.75E-03	2.56E-01	-8.28E-01	1.64E+00	6.14E-01	8267
	60	5.10E-03	2.34E-03	2.90E-02	-1.34E-01	3.30E-03	<10E-10	-5.10E-06	2.70E-06	5.91E-02	5.67E-03	4.73E-03	2.31E-01	-1.34E-01	2.37E+00	9.55E-01	4345
	70	5.09E-03	2.34E-03	2.93E-02	-1.34E-01	3.30E-03	<10E-10	-4.70E-06	2.69E-06	8.03E-02	5.25E-03	4.72E-03	2.66E-01	-9.30E+00	5.98E+00	1.20E-01	2157
	80	5.10E-03	2.34E-03	2.90E-02	-1.34E-01	3.30E-03	<10E-10	-4.77E-06	2.68E-06	7.49E-02	5.40E-03	4.71E-03	2.52E-01	-2.31E+01	1.15E+01	4.53E-02	1093
	90	5.10E-03	2.34E-03	2.92E-02	-1.34E-01	3.30E-03	<10E-10	-5.03E-06	2.68E-06	6.02E-02	5.79E-03	4.71E-03	2.19E-01	-4.47E+01	2.07E+01	3.10E-02	602
	100	5.10E-03	2.34E-03	2.91E-02	-1.34E-01	3.30E-03	<10E-10	-5.10E-06	2.68E-06	5.64E-02	5.75E-03	4.71E-03	2.22E-01	-7.62E+00	8.28E+00	3.57E-01	489
	>150	5.10E-03	2.34E-03	2.91E-02	-1.34E-01	3.30E-03	<10E-10	-5.13E-06	2.68E-06	5.53E-02	5.72E-03	4.72E-03	2.25E-01	-8.19E-01	7.52E+00	9.13E-01	219

Appendix A Table 2: Temporal statistics of analyzed rainfall intensities and integrated seasonal sensitivity estimates. NS denotes sensitivities with P > 0.1.

Intensity bin (mm hr-1)	Mean hours per season	Rainfall intensity percentile	Maize integrated seasonal sensitivity (bu ac^{-1})	Soy integrated seasonal sensitivity (bu ac^{-1})	Return frequency (yr^{-1})
0	4.78E+03	N/A			1.000
0.1	1.88E+02	45.5125	-4.462	-1.505	1.000
1	8.17E+01	76.3122	-9.115	-2.026	1.000
2.5	4.13E+01	88.0400	NS	NS	1.000
5	2.28E+01	93.4036	5.670	0.851	1.000
10	8.99E+00	97.3936	4.422	1.808	1.000
20	1.70E+00	99.5057	1.310	0.695	1.000
30	4.10E-01	99.8811	NS	NS	0.976
40	1.13E-01	99.9672	NS	NS	0.796
50	3.43E-02	99.9901	NS	-0.067	0.488
60	1.15E-02	99.9967	NS	-0.025	0.256
70	4.08E-03	99.9988	NS	-0.018	0.127
80	1.75E-03	99.9995	-0.040	NS	0.064
90	8.58E-04	99.9998	-0.038	NS	0.036
100	1.50E-03	N/A	NS	NS	0.029
>150	1.13E-03	N/A	NS	NS	0.013

Supplementary Table 3: Regional yield sensitivites with standard error and p-values

	Intensity bin	Maize			Soy			non-zero
		Intensity bin exposure hours			Intensity bin exposure hours			
	(mm hr^{-1})	coefficient	SE	p =	coefficient	SE	p =	county-years
Southeast	0	5.66E-03	4.69E-03	2.28E-01	5.66E-03	4.69E-03	2.28E-01	6432
	0.1	1.16E-02	6.50E-03	7.51E-02	1.16E-02	6.50E-03	7.51E-02	6432
	1	5.41E-02	2.59E-02	3.65E-02	5.41E-02	2.59E-02	3.65E-02	6432
	2.5	-6.86E-02	4.93E-02	1.64E-01	-6.86E-02	4.93E-02	1.64E-01	6432
	5	-8.86E-02	7.93E-02	2.64E-01	-8.86E-02	7.93E-02	2.64E-01	6432
	10	5.10E-02	1.48E-01	7.31E-01	5.10E-02	1.48E-01	7.31E-01	6432
	20	-4.20E-01	3.61E-01	2.45E-01	-4.20E-01	3.61E-01	2.45E-01	6432
	30	-5.52E-01	7.39E-01	4.55E-01	-5.52E-01	7.39E-01	4.55E-01	6372
	40	1.42E+00	1.17E+00	2.25E-01	1.42E+00	1.17E+00	2.25E-01	5649
Northeast	0	3.25E-02	4.05E-03	1.31E-15	3.25E-02	4.05E-03	1.31E-15	5125
	0.1	-4.12E-02	6.12E-03	1.92E-11	-4.12E-02	6.12E-03	1.92E-11	5125
	1	-2.08E-01	1.98E-02	2.29E-25	-2.08E-01	1.98E-02	2.29E-25	5125
	2.5	-3.55E-01	4.91E-02	5.16E-13	-3.55E-01	4.91E-02	5.16E-13	5125
	5	3.13E-01	8.14E-02	1.21E-04	3.13E-01	8.14E-02	1.21E-04	5125
	10	1.15E+00	1.49E-01	1.92E-14	1.15E+00	1.49E-01	1.92E-14	5125
	20	3.11E+00	3.71E-01	7.48E-17	3.11E+00	3.71E-01	7.48E-17	5122
	30	6.09E+00	9.47E-01	1.41E-10	6.09E+00	9.47E-01	1.41E-10	4883
	40	1.20E+01	2.54E+00	2.33E-06	1.20E+01	2.54E+00	2.33E-06	3448
West	0	2.76E-02	5.72E-03	1.40E-06	2.76E-02	5.72E-03	1.40E-06	5391
	0.1	-4.02E-02	8.09E-03	6.76E-07	-4.02E-02	8.09E-03	6.76E-07	5391
	1	-2.77E-01	2.88E-02	1.17E-21	-2.77E-01	2.88E-02	1.17E-21	5391
	2.5	-4.17E-02	6.20E-02	5.02E-01	-4.17E-02	6.20E-02	5.02E-01	5391
	5	2.30E-01	1.02E-01	2.49E-02	2.30E-01	1.02E-01	2.49E-02	5391
	10	1.08E+00	1.90E-01	1.45E-08	1.08E+00	1.90E-01	1.45E-08	5391
	20	2.68E+00	4.53E-01	3.44E-09	2.68E+00	4.53E-01	3.44E-09	5390
	30	2.07E+00	1.03E+00	4.58E-02	2.07E+00	1.03E+00	4.58E-02	5288
	40	-2.28E+00	2.25E+00	3.12E-01	-2.28E+00	2.25E+00	3.12E-01	4390

Appendix A Table 4: Dataset references and access information.

Dataset name	Reference	Access link
NCEP/EMC Stage IV Hourly 4km Precipitation	32	https://doi.org/10.5065/D6PG1QDD
USDA NASS Quick Stats	33	https://quickstats.nass.usda.gov/
NCEP CPC Global Daily Temperature		https://www.esrl.noaa.gov/psd/data/gridded/data.cpc.globaltemp.html
Daymet Gridded 1-km Daily Surface Weather, v2	34	http://dx.doi.org/10.3334/ORNLDAAC/1219

Appendix A Table 5. Time effects and number of counties observed per year for maize and soy.

Year	Maize		Soy	
	Year effect (bu ac^{-1})	Counties	Year effect (bu ac^{-1})	Counties
2002	-6.5	1075	0.1	1022
2003	0.0	1076	-4.8	1018
2004	10.8	1075	0.0	1027
2005	16.6	1075	5.6	1020
2006	17.1	1072	5.6	1012
2007	16.6	1072	2.9	994
2008	9.5	1052	-0.3	929
2009	19.2	1046	3.4	970
2010	23.1	1073	6.7	1006
2011	23.0	1064	8.4	970
2012	9.7	1065	9.0	985
2013	30.8	1039	6.6	935
2014	36.5	1039	8.2	947
2015	34.3	1032	8.6	907
2016	44.9	1043	13.5	936
2017	46.1	1037	10.9	925

Chapter 2: Stronger temperature-moisture couplings exacerbate the impact of climate warming on global crop yields

Published 20 September 2021, *Nature Food*, https://doi.org/10.1038/s43016-021-00341-6

Rising air temperatures are a leading risk to global crop production. Recent research has emphasized the critical role of moisture availability in regulating crop responses to heat and the importance of temperature-moisture couplings in driving concurrent heat and drought. Here, we demonstrate that the heat sensitivity of key global crops depends on the local strength of couplings between temperature and moisture in the climate system. Over 1970-2013, maize and soy yields dropped more during hotter growing seasons in places where decreased precipitation and evapotranspiration more strongly accompanied higher temperatures, suggestive of compound heat-drought impacts on crops. Based on this historical pattern and a suite of climate model projections, we show that changes in temperature-moisture couplings in response to warming could enhance the heat sensitivity of these crops as temperatures rise, worsening the impact of warming by -5% (-17 to 11% across climate models) on global average. However, these changes will benefit crops where couplings weaken, including much of Asia, and projected impacts are highly uncertain in some regions. Our results demonstrate that climate change will impact crops not only through warming, but also through changing drivers of compound heat-moisture stresses, which may alter the sensitivity of crop yields to heat as warming proceeds. Robust adaptation of cropping systems will need to consider this underappreciated risk to food production from climate change.

1) Introduction

Several studies have dentified negative relationships between air temperature and crop yields in observations, signaling the potential for global warming to reduce agricultural output

(Lobell et al., 2013; Lobell & Field, 2007b; Zhao et al., 2017). Extreme heat can steeply reduce crop yields both directly through heat stress and indirectly by raising atmospheric vapour demand and contributing to moisture stress (Lobell et al., 2013; Lobell et al., 2011; Prasad et al., 2008; Schlenker & Roberts, 2009; Urban, Sheffield, et al., 2015; E. Vogel et al., 2019). Because of this dual effect, the impacts of extreme heat are typically amplified by drought, and can be minimized with sufficient soil moisture from either precipitation or irrigation (Carter et al., 2016; Coffel et al., 2019; Matiu et al., 2017; Ortiz-Bobea et al., 2019; Rigden et al., 2020; Schauberger et al., 2017; Siebert et al., 2017; Troy et al., 2015; Urban, Sheffield, et al., 2015). Jointly hot and dry conditions thus pose a particular climate risk to global crops, especially under global warming (Lesk & Anderson, 2021).

In many regions, such jointly hot and dry conditions during cropping seasons tend to occur due to physical couplings between temperature and moisture in the climate system (A. Berg et al., 2015; Seneviratne et al., 2010; Zscheischler & Seneviratne, 2017). These couplings can be conceptualized in two ways: first as a connection between temperature (T) and precipitation (P), and second as a connection between T and evapotranspiration (ET). We refer to the former connection as the *atmospheric circulation* coupling, and the latter as the *land-atmosphere interaction* coupling. While the separability and relative importance of these two couplings is debated (A. Berg et al., 2015; Seneviratne et al., 2006; Trenberth & Shea, 2005) (see Methods), they generally reflect two critical sets of processes that both vary in magnitude over global croplands and strongly influence the local risk of joint heat and drought.

Where the atmospheric circulation coupling is strong, clear skies tend to accompany dry cropping seasons, boosting temperatures at the surface due to increased penetration of solar radiation and delivery of warm compressed air by descending winds (A. Berg et al., 2015; Horton

et al., 2016; Trenberth & Shea, 2005; Zscheischler & Seneviratne, 2017). The strength of this coupling is reflected by the magnitude of the negative correlation between temperature and precipitation across years ($r_{T,P} < 0$). Where the land-atmosphere coupling is strong, ET tends to decline during a warmer cropping season, reflected by a negative correlation between T and ET ($r_{T,ET} < 0$). The resulting enhanced sensible heating can further raise air temperatures and atmospheric vapour demand, generating a positive feedback (A. Berg et al., 2014; Miralles et al., 2014; Seneviratne et al., 2006, 2010). By contrast, enhanced ET from warmth ($r_{T,ET} > 0$) limits the feedback between warming and drying. Thus, the couplings characterized by negative correlations of T with ET and P drive concurrent and mutually-reinforcing hot and dry conditions during the cropping season in many regions.

Despite the importance of these couplings in controlling the concurrent heat and moisture stresses that so strongly damage crop yields, their effect on global crop responses to current and future temperatures remains a gap in understanding present and future climate impacts on crops. Here, we demonstrate the global influence of temperature-moisture couplings on crop yield sensitivity to temperature over 1970-2013 and project future impacts on crops from changing couplings. We combine historical global yield observations (Ray et al., 2015, 2019) with observed and modeled meteorological data to show that during warmer growing seasons, maize and soybean yields drop more steeply where precipitation and ET tend to also decrease. Using simulations from a suite of climate models, we then identify how these couplings are likely to change by the late 21st century. Combining these projections with the historical results, we demonstrate that the modified couplings will likely worsen the impacts of warming on some of the world's most important crops.

2) Results and Discussion

Historical influence of temperature-moisture couplings on crop heat sensitivity

Over the historical period, we find significant correlations between crop yields and mean seasonal temperature over 20-32% of global maize, soybean, rice and wheat croplands ($p < 0.1$, Fig. 1). While maize and soybean yields generally decline with increasing temperature (by 0.3-0.4 standard deviations (σ) per σ temperature), they benefit from heat over around a quarter of croplands with significant temperature impacts, primarily at higher latitudes and elevations as well as in pockets of the tropics (Fig. 1a-b). Yield benefits from warmer seasons in some locations likely reflect crop limitations by cold and short growing seasons. By contrast, wheat yields are almost universally reduced by higher temperatures in North America and Eurasia (Fig. 1c), likely reflecting the lower physiological heat tolerance of wheat compared to maize (Liu et al., 2016; Sánchez et al., 2014). While seasonal heat benefits rice yields in parts of Europe and damages them slightly in India, rice yields show a generally weaker connection to temperature (Fig. 1d), as reported elsewhere (David B Lobell & Field, 2007b; Welch et al., 2010). This may relate to the prevalence of irrigation in rice cropping, which may partially decouple yields from temperature. We also note weak maize yield dependence on temperature where it is mainly irrigated such as northern India, central France, and the western United States (Fig. 1a).

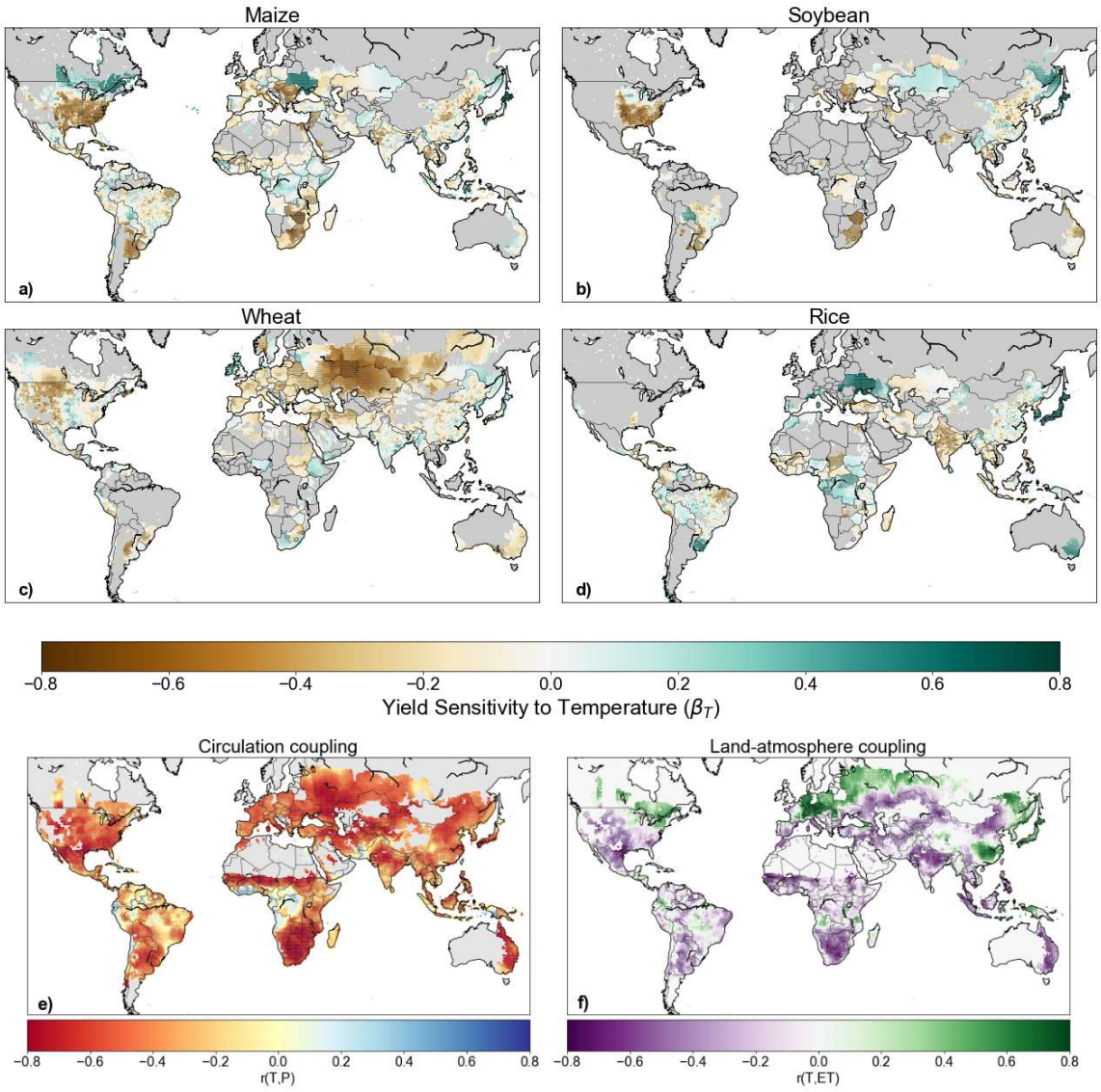

Figure 1: Crop yield sensitivity to temperature and temperature-moisture couplings across global croplands. Standardized yield sensitivity to mean growing season maximum air temperature estimated as the linear slope coefficient, with units of standard deviations (σ) of yield per σ temperature, for a) maize, b) soybean, c) wheat, and d) rice. Yield and temperature observational data are detrended to remove long-term warming and yield trends. Stippling denotes significant slope coefficients (two-tailed $p < 0.1$, t-test). Land area without crops is shown in gray. e) Circulation coupling strength, measured as the interannual correlation between detrended observed growing season mean temperature and total precipitation ($r_{T,P}$). f) Land-atmosphere coupling, measured as the interannual correlation between detrended modeled growing season mean temperature and evapotranspiration ($r_{T,ET}$). Couplings in e-f are shown for the maize growing season and over the full global cropland where data is available to ease interpretation of global patterns. Couplings for other growing seasons are shown in Appendix B Fig. 1.

Large portions of the global croplands also experience significant temperature-moisture coupling during the local growing season. Seasonal total precipitation is significantly correlated with mean temperature over 62-89% of cropland ($p < 0.1$, Fig. 1e, Appendix B Fig. 1), with exceptions mainly concentrated in the tropics. These significant interannual correlations are almost entirely negative (>98%), with mean magnitude of -0.5. ET further correlates with temperature over 36-65% of global croplands ($p < 0.1$, Fig. 1f, Appendix B Fig. 1). Correlations are predominantly negative over global croplands but are positive at higher latitudes as well as in southern China (Fig. 1f), a pattern corresponding broadly to moisture- versus energy-limited soil moisture regimes (Seneviratne et al., 2010), respectively. The majority of global cropland area thus experiences climate couplings whereby lower moisture conditions coincide with higher heat and moisture demand.

We find a global tendency for increasingly negative impacts of temperature on maize and soybean yields with the increasing strength of these temperature-moisture couplings historically. Figure 2 situates the grid-cell yield sensitivity to temperature (presented as the colouring of the points) with respect to the local strength of the two temperature-moisture couplings (presented as the position in the plane of the points). The lower-left quadrant of each panel includes grid cells with both circulation and land-atmosphere couplings ($r_{T,P}$ and $r_{T,ET} < 0$). For maize and soy (Fig. 2a-b), we note that this quadrant contains the bulk of grid cells where yields decline with temperature, with greatest negative yield sensitivities where couplings are strongest. Meanwhile, yields tend to benefit from warmer temperatures where the couplings are weakest ($r_{T,P} \sim 0$ and $r_{T,ET} > 0$).

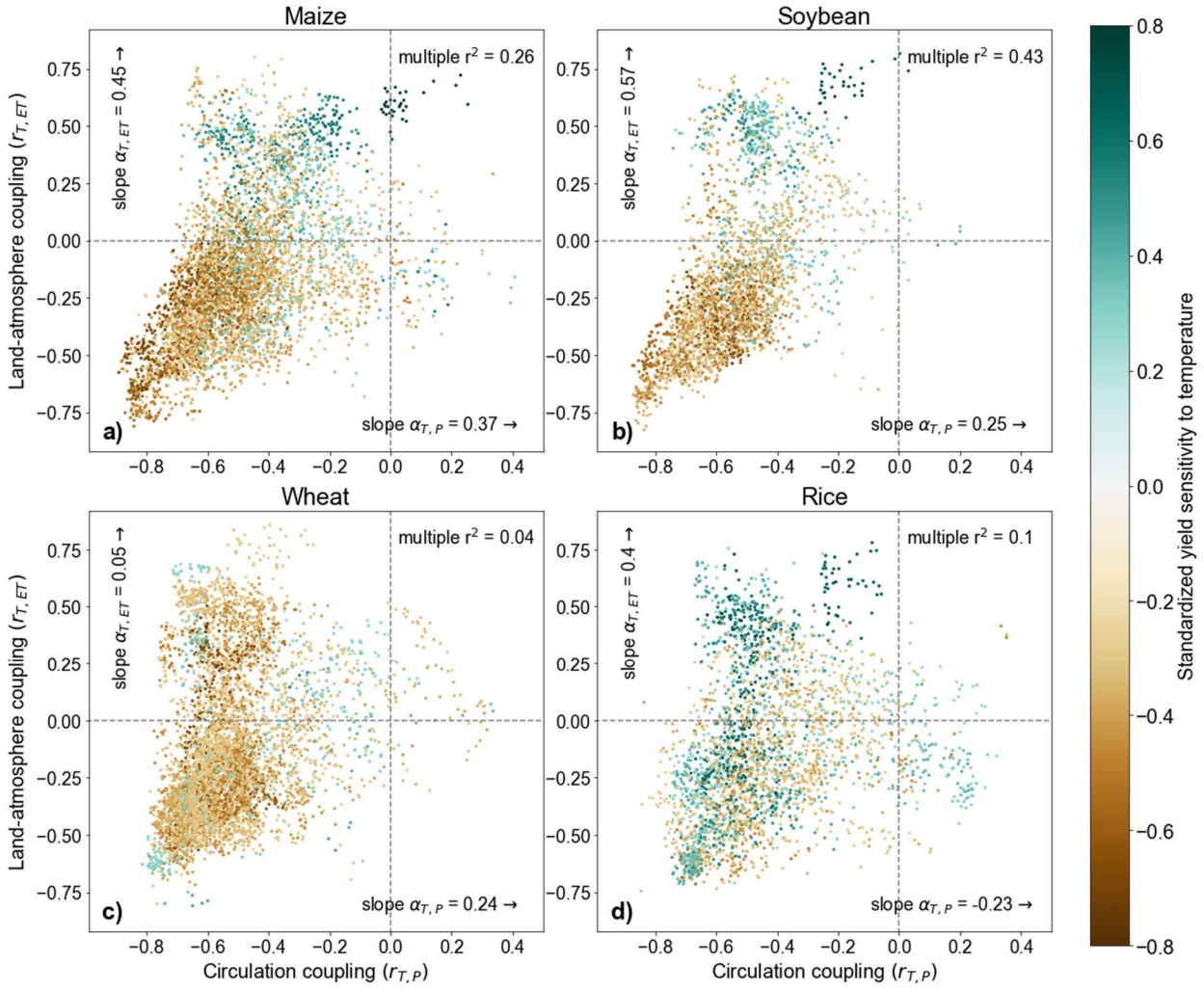

Figure 2: Global dependence of yield sensitivity to temperature on two temperature-moisture couplings. Estimated standardized yield sensitivity to mean growing season maximum air temperature (colouring of points) plotted in relation to correlations of temperature with ET (land-atmosphere coupling, vertical axes) and precipitation (circulation coupling, horizontal axes), for a) maize (n = 4,771 grid cells), b) soybean (n = 2,663), c) wheat (n = 5,062), and d) rice (n = 2,800). Each data point represents one grid cell. Data are shown for areas with significant yield response to temperature (two-tailed $p < 0.1$). Slope coefficients relating yield sensitivity to each coupling ($\alpha_{T,P}$ and $\alpha_{T,ET}$) are annotated on their respective axes. Reported multiple r^2 values are for the multiple regression model relating yield sensitivity to the two couplings.

To quantify these relationships, we regress crop yield sensitivity to temperature on the two couplings and find meaningful global dependence for maize and soy ($r^2 = 0.26$ for maize and 0.43 for soybean, Fig. 2a-b). The regression also affords slope coefficient estimates, $\alpha_{T,P}$ and $\alpha_{T,ET}$, that

quantify the steepness of the dependence of yield sensitivity to temperature on the two couplings. On average, yields decline more steeply per σ temperature (slope $\alpha_{T,ET}$ ± standard error = 0.45±0.02 for maize and 0.57±0.02 for soybean, $p < 0.001$) in areas with the most negative $r_{T,ET}$. In other words, crops are around 40% more sensitive to temperature (34% for maize and 43% for soybean) in regions with strong land-atmosphere coupling, compared to where temperature and ET are uncorrelated. The influence of the land-atmosphere coupling on yield sensitivity to temperature is somewhat larger than the influence of circulation coupling on yield sensitivity to temperature (slope $\alpha_{T,P}$ ± standard error = 0.37±0.03 for maize and 0.25±0.04 for soybean, $p < 0.001$). We found no spatial correlation between recent 10-year mean yields (2004-2013) and the two couplings ($r^2 < 0.02$), suggesting that the observed effects are independent of overall crop productivity. Overall, these patterns of higher crop heat sensitivity where couplings are strong is consistent with the compounding of heat impacts on crops by moisture effects where these couplings are strong, and alleviation where they are weak.

By contrast, we find little such dependence on temperature-moisture couplings among the temperature sensitivities of wheat and rice (Fig. 2c-d, $r^2 \leq 0.1$). This may be due in part to the low thermal tolerance of wheat, whose optimal growth temperature is about 10°C cooler than for the other crops (Liu et al., 2016; Sánchez et al., 2014). Due to its exponential dependence on temperature, atmospheric vapor demand and its impact on crops increase most strongly at relatively high temperatures. However, heat impacts on wheat may be severe at relatively low temperatures, for which atmospheric vapor demand remains relatively low, limiting the scope for compounding of heat impacts by moisture (T. Zhang et al., 2015). For rice, lower heat sensitivity and widespread irrigation may effectively decouple the crop from temperature and moisture (Fig. 1d), similarly precluding compounding impacts (Welch et al., 2010).

These results suggest that local crop responses to temperature depend not only on crop physiology and temperature stressors, but also on climatological couplings between temperature and moisture. These couplings tend to align heat and moisture stress in time, exposing crops to heat and high atmospheric moisture demand while precipitation and soil moisture are low (Fig. 3). Where the couplings are strong, yields are likely more sensitive to temperature due to antagonistic feedbacks between physiological heat and drought acclimation and stress mechanisms (Mittler, 2006; Prasad et al., 2008), notably the impact of stomatal closure on canopy temperature and photosynthesis (Crafts-Brandner & Salvucci, 2002; Gates, 1968; Grossiord et al., 2020; Prasad et al., 2008; Siebert et al., 2017; Skinner et al., 2018; Swann, 2018) (Fig. 3). By contrast, where the couplings are weak, heat and high atmospheric moisture demand are more likely to coincide with periods of normal or abundant precipitation and soil moisture, mitigating the impact of heat on crops.

Importantly, these results indicate that the ultimate impact of global warming on some crops will depend not only on the mounting heat hazard itself, but also on the impact of warming on the physical coupling between temperature and moisture. Specifically, they raise the possibility that climate change will affect the sensitivity of crop yields to heat by altering temperature-moisture couplings throughout the world. This potential impact is currently omitted from climate risk projections using statistical models (David B. Lobell et al., 2011; Schlenker & Roberts, 2009; Zhao et al., 2017), which assume constant temperature sensitivity into the future, and mechanistic crop models, whose climate projection inputs are typically adjusted to match the historical correlation structure between temperature and moisture (Rosenzweig et al., 2014; Zhao et al., 2017), excluding the potential influence of changes in temperature-moisture couplings.

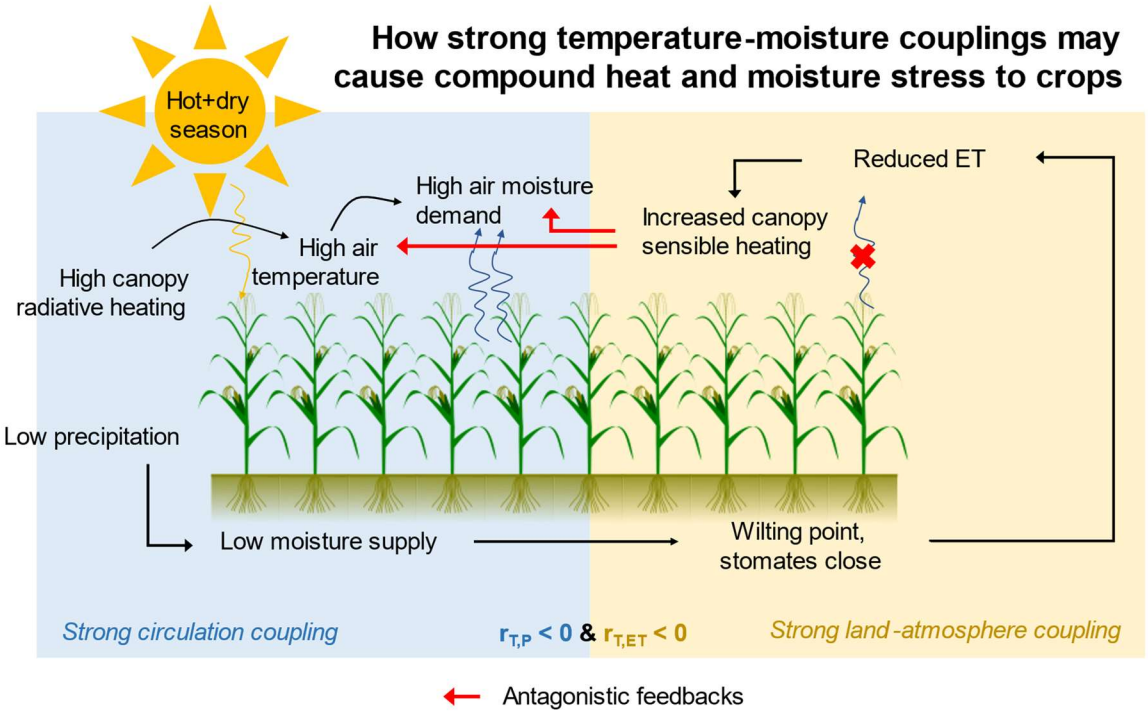

Figure 3: Schematic of potential mechanism for compound heat and moisture impacts on crops in regions with strong temperature-moisture couplings. Where temperature-moisture couplings are strong, hot growing seasons are more likely to be also dry, depicted by the sun at upper left. Ensuing effects of consequence to crops that are linked to strong circulation coupling ($r_{T,P} < 0$) are shown in the blue square at left, while effects linked to strong land-atmosphere coupling ($r_{T,ET} < 0$) are shown in the yellow square at right. Red arrows show antagonistic feedbacks by which correlations of temperature with P and ET can induce compounding heat and moisture stresses on crops.

Impact of projected change in couplings on global crop yields

To examine the implications of these effects for maize and soy under future climate change, we combine the historical dependence of yield sensitivity to temperature on the two couplings (Fig. 2) with simulated future changes in couplings from a suite of 12 CMIP6 global climate models (Eyring et al., 2016). By 2051-2100 under moderate greenhouse gas emissions (SSP2-4.5), we project substantial changes in $r_{T,ET}$ and to a smaller extent in $r_{T,P}$ (Fig. 4a-b), over much of global croplands in the ensemble median. These changes indicate amplified couplings between temperature and moisture in response to climate warming over croplands in the US, Europe, and southeastern Africa, but reduced couplings across southern to eastern Asia. Based on historical relationships in Fig. 2a-b, these changes in couplings will likely exacerbate yield sensitivity to temperature over a preponderance of croplands, but alleviate it in much of Asia (Fig. 4c).

We project that such heightened crop heat sensitivities due to changing temperature-moisture couplings will worsen the impacts of warming on maize and soy yields across most of the globe (Fig. 5a, Appendix B Fig. 2). In the multi-model median, these additional yield impacts ($\Delta\Delta Y$) amount to regional maize (soy) losses of 7% (9%) in the US, 7% (16%) in western Europe, 12% (24%) in eastern Europe, 9% (5%) in southeastern Africa, and 3% (6%) in southeastern South America, with more modest yield gains of 1% (3%) in eastern Asia (Fig. 5a and d, Appendix B Fig. 2). We note important model uncertainty in these regional figures, which we discuss further below and in Figure 6d. More severe localized yield impacts at sub-regional scales reach ~20% in the United States and ~40% in eastern Europe and southeastern Africa.

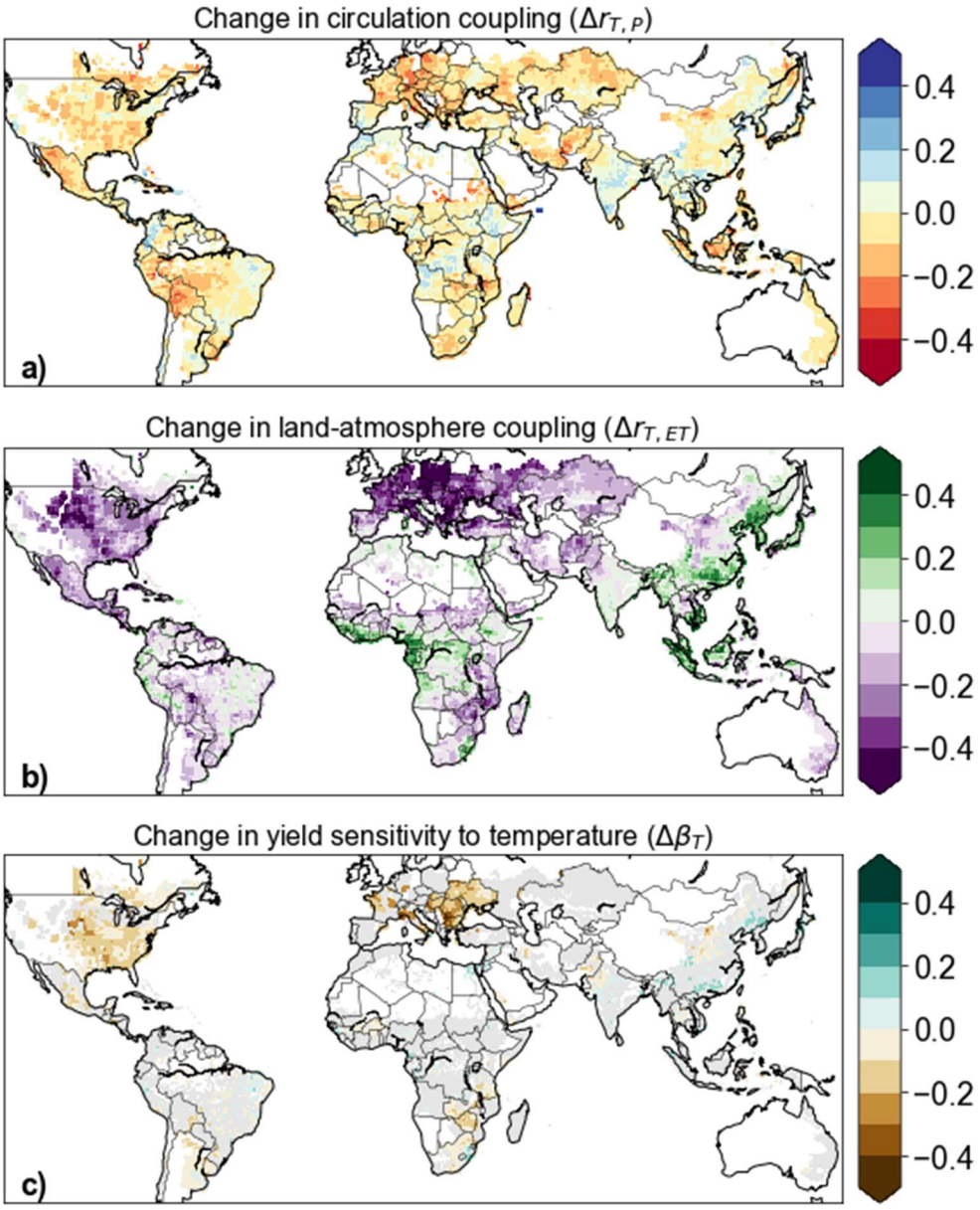

Figure 4: Projected future changes in temperature moisture couplings and yield sensitivity to temperature in response to warming. a) Projected change in circulation coupling (detrended interannual $r_{T,P}$) over 2051-2100 under a moderate emissions scenario (SSP2-4.5), compared to historical couplings over 1961-2010. The median of an ensemble of 12 CMIP6 climate model projections is shown for each grid cell. b) Same as a), but for land-atmosphere coupling ($r_{T,ET}$). c) Projected change in standardized maize yield sensitivity to temperature in response to changes in the two couplings, based on global slope coefficients from in Fig. 2a. For a-b) projections are shown over the full global maize croplands to facilitate interpretation of broader patterns, while for c) projections are shown only for areas with significant historical maize yield sensitivity to temperature ($p < 0.1$); gray shading shows croplands with insignificant yield dependence on temperature.

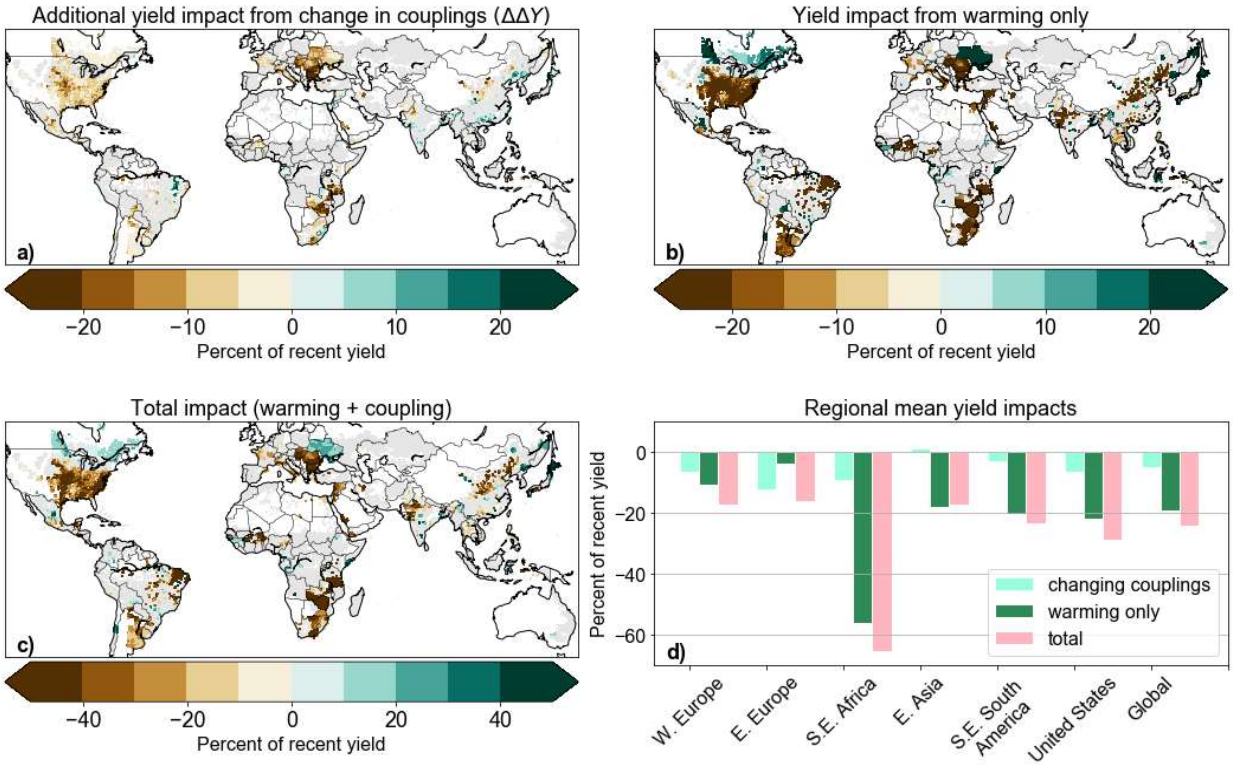

Figure 5: Projected additional impact of future warming on maize yields due to changing temperature-moisture couplings. a) Ensemble median additional impact of warming on maize yields from projected changes in $r_{T,ET}$ and $r_{T,P}$ over 2051-2100 under a moderate emissions scenario (SSP2-4.5), as a percent of local mean of recent yields (2004-2013). b) Maize yield changes (as a percent of recent yield) from ensemble median warming only, projected using historical yield sensitivity to temperature from Fig. 1a. c) Projected total yield impacts, estimated as the sum of impacts from changing couplings and warming only (note that the scale differs from a-b). Projections in a-c) are shown only for areas with significant historical maize yield sensitivity to temperature ($p < 0.1$); gray shading shows croplands with insignificant yield dependence on temperature. d) Yield impacts averaged across selected key regions and globally. Model uncertainties associated with these ensemble median results are shown in Figure 6

These projected additional yield impacts due to changing temperature-moisture couplings ($\Delta\Delta Y$) would add to projected yield losses from warming alone (Fig. 5b), worsening them in some regions (e.g. in central US) but slightly ameliorating them in others (e.g. in eastern Asia, Fig. 5c). In some cool climates such as in the northern US, Canada, and Ukraine, changing couplings may also curtail projected yield gains from warming. Globally, we project that changing couplings will

aggravate the impact of warming on maize and soy yields by ~5% relative to recent yields (Fig. 5d, Appendix B Fig. 2), evincing an important but underappreciated risk to agriculture under climate change.

Considerable inter-model variation underlies these multi-model median projections (Zscheischler & Seneviratne, 2017). Over much of global maize croplands, fewer than two-thirds of models agree on the sign of additional yield changes due to coupling responses to warming ($\Delta\Delta Y$, Fig. 6a), especially in the tropics and sub-tropics. Even in areas with high model agreement on sign (mainly in Europe, the US, and eastern Asia), the magnitude of change can vary substantially across models (Fig. 6d, Appendix B Fig. 3). This inter-model variability induces uncertainty in the projected global mean impacts for the moderate emissions scenario, with model-specific yield impacts ranging from -17 to 11% (Fig. 6b, blue bars).

Alternate emissions scenarios add a further dimension of uncertainty to the projected yield impacts of changing temperature-moisture couplings. Under a high emissions scenario (SSP5-8.5), maize yield losses in the Americas and southeastern Africa are reduced and gains in Asia are increased compared to the moderate emissions scenario (Fig. 6c-d). Surprisingly, these regional responses amount to a global mean *additional* yield gain ($\Delta\Delta Y$) of 1.6% in the ensemble median (‘*additional* ’in that they only slightly offset large yield loss from warming itself). The counterintuitive non-monotonicity of the global mean response to emissions is ultimately driven by regional coupling changes that alleviate yield sensitivity to temperature, most notably the widespread relative decoupling between T and P under higher emissions (Appendix B Fig. 4). However, we also note large model disagreement in the high emissions scenario, with global mean impacts ranging from -18 to 32% (Fig. 6b, red bars).

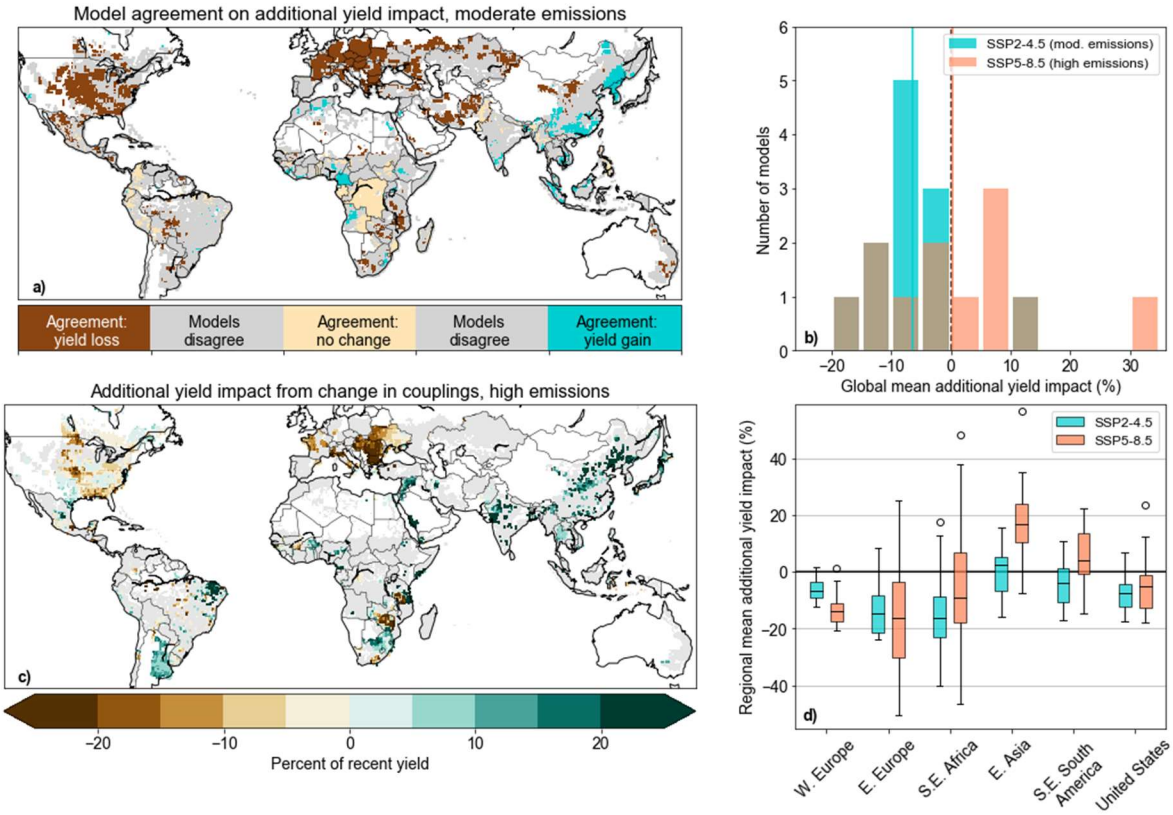

Figure 6: Uncertainty in projected additional maize yield impact due to changing temperature-moisture couplings. a) Model agreement on local sign of projected additional yield impact due to changing temperature-moisture couplings ($\Delta\Delta Y$) under a moderate emissions scenario by 2051-2100. Colouring denotes areas where at least two-thirds (8 out of 12) of the models in the ensemble agree on either positive (blue), negative (brown), or no substantial change (within +/- 10%, beige). Grey denotes areas with less than two-thirds model agreement on direction of change. b) Distribution of model-specific global mean additional yield impact due to changing couplings ($\Delta\Delta Y$) for the moderate emissions (SSP2-4.5, blue) and high emissions (SSP5-8.5, red) scenarios. Vertical red and blue lines denote multi-model median global mean impacts. Additional yield impacts are expressed as a percentage of 2004-2013 mean yields, averaged over areas with significant temperature effects on yield (Fig. 1a). c) Ensemble median additional impact of warming on maize yields due to changes in couplings over 2051-2100 under the high emissions scenario (SSP5-8.5), as a percent of local mean of recent yields (2004-2013). Projections are shown only for areas with significant historical maize yield sensitivity to temperature ($P < 0.1$); gray shading shows croplands with insignificant yield dependence on temperature. d) Same as b), but with additional yield impacts averaged over selected regions. Boxplot centerline denotes multi-model median; whiskers, tail projections within 1.5 interquartile range; and points, outliers.

The uncertainties in these projections highlight unresolved challenges in simulating temperature-moisture couplings using climate models and their importance to predicting the impact of climate change on global crop production. Specifically, the response of ET (largely mediated by soil and vegetation dynamics and land-atmosphere interaction) and precipitation (largely mediated by regional circulation) to interannual variability in temperature in future climates are both active areas of research (Lesk et al., 2020; Orlowsky & Seneviratne, 2010; Seth et al., 2019; Swann, 2018). While some regions with model consensus may reflect predictions with strong physical foundations, such as the enhanced land-atmosphere coupling in Europe with warming (Seneviratne et al., 2006; M. M. Vogel et al., 2017), they may also arise from stronger observational constraints and model validation effort across the northern midlatitudes (B. Mueller et al., 2011; Zscheischler & Seneviratne, 2017). Some regions lacking model consensus include important breadbaskets in southeast South America and chronically food-insecure and drought-vulnerable southeastern Africa, where weather observations are comparatively sparse and couplings are not well-constrained by observations (Zscheischler & Seneviratne, 2017) (Fig. 6, Appendix B Fig. 3). These regions also tend to have the largest differences in estimated historic couplings between CMIP6 and observation-based data (Appendix B Figure 5). Our result show how these uncertainties and potential model inaccuracies presently impede a complete understanding of the risks of climate change to crop production.

Several limitations of our study reflect important challenges and open questions. First, while we assess seasonal-scale yield responses and temperature-moisture couplings, future studies may consider sub-seasonal time scales, particularly the role of the couplings in short-duration heat extremes and flash droughts (Pendergrass et al., 2020; M. M. Vogel et al., 2017), and the differential vulnerability of crop growth stages. Second, we treat crops as passively affected by

these couplings, but in some densely-cropped regions they actively influence climate by modifying regional ET (He et al., 2020; N. D. Mueller et al., 2017). While this occurrence is limited to certain high-yielding regions at present, it may become increasingly common with continued crop intensification and thus merits further attention. Third, while we treat circulation and land-atmosphere couplings as distinct, the influence of their overlap and interaction on past and future crop yield sensitivity to temperature should be investigated (A. Berg et al., 2015; Orlowsky & Seneviratne, 2010). Fourth, future work should consider the uncertain impact of increased atmospheric CO_2 on future crop responses to combined heat and moisture stresses (Ainsworth & Long, 2021; Deryng et al., 2016), which may weaken or amplify the relationships in Fig. 2 by increasing the water use efficiency of crops (yield per unit water transpired). Finally, further attention to the role of natural vegetation, aerosols, and climate modes such as the El Niño-Southern Oscillation in temperature-moisture couplings is also merited (Skinner et al., 2018; Swann, 2018).

3) Conclusions

Limitations and uncertainties in the climate models notwithstanding, we draw the following main conclusions from our results. Local heat sensitivity of crop yields depends on the strength of coupling between temperature and moisture for maize and soy, but not for rice and wheat. We propose that this dependence, and its absence for rice and wheat, is consistent with the compounding of heat impacts by moisture stress where couplings are strong, and mitigation where they are weak. By 2051-2100, enhanced couplings over a majority of global cropland will most likely make crops more vulnerable to warming temperatures, with notable exceptions across Asia, where couplings weaken. These climate impacts on crops are widely omitted from climate risk assessments.

Our projections of a mounting threat to crop yields from changing temperature-moisture couplings in a warming climate underscore the need to adapt global crop management and genetics to concurrent heat and moisture stresses. Cropping adaptations, such as breeding for drought and heat tolerance, should thus avoid antagonisms between stress mechanism where couplings strengthen in the future (Challinor et al., 2016; Prasad et al., 2008), but may leverage them where couplings weaken. For instance, irrigation may disrupt the antagonistic feedbacks that lead to compounding heat and moisture stresses, so its effectiveness as a crop adaptation to heat may be enhanced where couplings get stronger in the future. However, the reliability of irrigation may simultaneously decline with strengthening couplings, as drought increasingly limits the availability of water for irrigation during extreme heat (i.e., when it is needed most). As another example, breeding crops for drought tolerance based on stomatal regulation (Gates, 1968; Grossiord et al., 2020) or sowing density (David B. Lobell et al., 2020) may exacerbate heat impacts by reducing canopy evaporative cooling or raising crop water demand respectively, a risk that would be less important where couplings weaken (as in much of Asia). Finally, our results may help further calibrate joint temperature-moisture impacts in crop models to assure their usefulness in developing climate-adaptive cropping strategies (Bassu et al., 2014; Schauberger et al., 2017).

Efforts to adapt cropping to climates with increasingly strong temperature-moisture couplings may prioritize subsistence cropping areas that are already prone to drought and heat, and where we project enhanced couplings to worsen crop vulnerability in the future. Even with robust adaptations, changes in crop sensitivity to heat under climate change will likely necessitate greater international cooperation in equitable food trade and emergency relief as climate shocks increase.

4) Methods:

Data and processing

For the historical climate analyses, we combine monthly 0.5° gridded mean temperature and total precipitation observations from the Hadley Center Climate Research Unit (CRU TS4.02) (Harris et al., 2014) with 0.25° modeled mean temperature and ET data from Global Land Data Assimilation System (GLDAS) Noah land surface model L4, version 2.0 (Rodell et al., 2004). We coarsen the ET data from 0.25° to 0.5°, to match the resolution of the temperature and precipitation data. To represent growing seasonal mean conditions, we average temperature and ET and sum precipitation during the average crop-specific growing periods based on a global crop calendar (Sacks et al., 2010). For wheat, we define the growing season as three months prior to harvest to exclude the vernalization period for winter wheat. Because ET is the input data with the greatest observational limitations, we verified the robustness of key parameters estimated via the regression model in Equation 2 to three alternative historical ET datasets: 1) GLDAS V2.0 Catchment Land System Model (CLSM) L4 over 1961-2010 (Rodell et al., 2004), 2) GLDAS V2.0 Variable Infiltration Capacity (VIC) L4 over 1961-2010 (Rodell et al., 2004), and 3) ERA5 Reanalysis over 1980-2010 (Hersbach et al., 2020).

The crop yield data are based on statistics from ~20,000 subnational political units over 1970-2013, harmonized for consistency with UN Food and Agriculture Organization (FAO) national statistics and gridded to 0.5° resolution (Ray et al., 2019). While harmonizing the subnational statistics with national FAO data ensures comparability between nations, it may introduce discontinuities in the data along certain national boundaries, notably Ukraine. We focus on maize, wheat, rice, and soy as crops that are globally dominant in calorie consumption and distributed across the world. For both the climate and crop data, we isolate interannual variability

from longer-term trends using singular spectrum analysis (SSA), a non-parametric method that avoids assumptions about the functional form of the climate and yield trends (Vautard et al., 1992; E. Vogel et al., 2019).

Historical temperature-moisture couplings

To characterize the couplings between temperature and moisture, we compute grid-cell interannual Pearson's correlation coefficients between the detrended temperature and ET from GLDAS for the land-atmosphere coupling ($r_{T,ET}$), and temperature and precipitation from CRU for the circulation coupling ($r_{T,P}$). This approach leverages the strengths of observation-based data for $r_{T,P,}$ but employs model-based data for ET, which is comparatively is sparsely observed over global croplands (B. Mueller et al., 2011; Zscheischler & Seneviratne, 2017). To improve the robustness of interannual correlations with respect to important modes of climate variability like the El Nino-Southern Oscillation, we use a somewhat longer 50-year time period of 1961-2010 than the study period constrained by the yield data. We define statistical significance of the couplings for each grid-cell using a two-tailed t-test with a threshold of $P < 0.1$.

For clarity, our nomenclature contrasts these two couplings based on the dominant locus of their occurrence either in atmosphere dynamics or land-atmosphere interactions (A. Berg et al., 2015; Seneviratne et al., 2010; Trenberth & Shea, 2005). However, the two couplings interact physically in some regions and should not be considered strictly distinct (A. Berg et al., 2015; Seneviratne et al., 2006; Trenberth & Shea, 2005). For instance, global correlations between grid cell $r_{T,ET}$ and $r_{T,P}$ ($r^2 = 0.21$ for maize and 0.29 for soybean) may reflect links among P, ET, and T in the coupled surface-atmosphere system that are not easily disentangled. Despite this, the magnitude of these correlations and the broadly divergent spatial pattern in their historic and

projected future magnitude both suggest a prevailing differentiation of the two couplings. For brevity, we present the couplings only for maize in Figure 1 and for the other crops in Appendix B Figure 1, because their spatial pattern does not differ substantially across the different crops.

Historical crop yield sensitivity to heat

We estimate the historical yield sensitivity to temperature as the slope coefficient (β_T) in a simple linear regression model relating detrended yields to temperature for each grid cell:

$$y = \beta_0 + \beta_T T + \varepsilon \qquad (1)$$

where y denotes estimated yields, β_0 the intercept, T the mean seasonal temperature, and ε the residual errors. Repeating this analysis for the four crops generates four maps of yield sensitivity to temperature for each crop. We standardize yield and temperature data such that β_T has units of standard deviations of yield per standard deviation of temperature (i.e., is dimensionless). This standardization eases the comparison of yield sensitivity across crop regions with different means and variances of yield and temperature.

The simplicity of this linear model for temperature impacts on yields eases interpretability of the spatial pattern of impacts and the results of subsequent analyses, at the cost of reduced specificity between the impacts of beneficial and detrimental sub-seasonal temperatures that comprise the seasonal mean temperature. Despite this limitation, the spatial pattern and magnitude of estimated yield sensitivity largely agrees with past studies using more complex models. For instance, we compare our unstandardized yield sensitivities aggregated to the national scale with those in the multi-model comparison of Zhao et al. (2018, ref. 4) in Appendix B Figure 8, and find broadly consistent signs and magnitudes for top producing countries for the four crops.

We define statistical significance of the yield sensitivities for each grid cell using a two-tailed t-test with a threshold of $p < 0.1$. Importantly, we do not interpret this yield sensitivity to

reflect the response to heat stress alone, but also response of crops to temperature via its impact on vapour pressure deficit, a key variable in moisture stress (D. B. Lobell et al., 2013; Rigden et al., 2020; Urban, Sheffield, et al., 2015). We conduct this analysis for all grid-cells with non-zero crop area to leverage the largest possible diversity of climates and crop systems, regardless their areal intensiveness.

Historical impact of temperature-moisture couplings on yield

Next, we assess the dependence of standardized yield sensitivity to temperature on the two historical coupling measures using a multiple linear regression model of the form:

$$\beta_T = \alpha_0 + \alpha_{T,ET} r_{T,ET} + \alpha_{T,P} r_{T,P} + \varepsilon \quad (2)$$

where $\alpha_{T,ET}$ and $\alpha_{T,P}$ coefficients reflect the response of yield sensitivity to each coupling ($r_{T,ET}$ and $r_{T,P}$), α_0 is the intercept, and ε the residual errors. This method aggregates local yield sensitivities and coupling strengths into a dataset for each crop, and the regression results in two global estimates of the yield sensitivity response to each coupling ($\alpha_{T,ET}$ and $\alpha_{T,P}$) for each crop. Because they represent change in a standardized coefficient per unit change in correlation, $\alpha_{T,ET}$ and $\alpha_{T,P}$ are dimensionless. We include all grid cells with non-zero crop area and significant yield sensitivities to temperature ($p < 0.1$) in this analysis, and note that the regression results are highly robust to a stricter significance threshold of $p < 0.05$ (Appendix B Fig. 9). Based on a minimum threshold for the coefficient of determination (r^2) of 0.2, we judge whether the couplings are substantially predictive of yield sensitivities for each crop, and proceed with future projections only for crops that met this criterion. Variance inflation factors for the models in Equation 2 were 1.2-1.3, indicating low susceptibility of the coefficient estimates to the moderate collinearity between $r_{T,ET}$ and $r_{T,P}$ (r^2 ~0.2-0.3). Estimated model parameters were broadly robust to

alternative historical ET datasets, including VIC and CLSM land models from GLDAS and the ERA5 reanalysis (Appendix B Figure 6).

Projecting future change in couplings

To assess future changes in the couplings, we employ projected monthly mean temperature and ET and monthly total precipitation from a suite of Coupled Model Intercomparison Project 6 (CMIP6) general circulation models, run under the SSP2-4.5 moderate emissions scenario(Eyring et al., 2016). We use all 12 models for which ET data is complete and available. The projected climate data are aggregated to the local growing season. We detrend the seasonal time series using SSA to remove the large influence of long-term forced trends in the climate variables, and regrid the data to a common 0.5° resolution. Despite the lower native resolution of many climate models, we proceed with this higher resolution to conserve the spatial detail of historical mean yields and yield sensitivities to temperature, which are based on higher-resolution data. However, we avoid introducing non-physical results to our downscaled climate projections by using nearest-neighbour approximation rather than interpolating. This method essentially conserves the original model resolution in the climate component of our projections, without sacrificing the higher resolution of observed variables.

To project future changes in the temperature-moisture couplings, we compute $r_{T,ET}$ and $r_{T,P}$ in the climate model data for both the historical period 1961-2010 and a future period of 2051-2100. We select the latter period to be distant enough in the future for climate signals to clearly emerge, but close enough to be useful for adaptation planning. We then compute a multi-model ensemble of correlation change factors by differencing the correlations between the historical and future periods. This differencing approach eliminates extraneous influence of historical mean

model biases compared to observations (Appendix B Fig. 5), isolating the relative change in couplings projected by each model relative to its own historical period. Despite this, we note that historical biases likely reflect incomplete model simulation of the processes relevant to change in the couplings. To represent the central tendency of the projection ensemble, we use the multi-model medians of projected change factors in couplings ($\Delta r_{T,ET}$ and $\Delta r_{T,P}$).

Projecting crop yield impacts of changing couplings

We use the historical estimated coefficients relating yield sensitivity to temperature with each coupling ($\alpha_{T,ET}$ and $\alpha_{T,P}$ in equation 2) to project future changes in yield sensitivity to temperature ($\Delta\beta_T$) resulting from changes in the couplings, following:

$$\Delta\beta_T = \alpha_{T,ET}\Delta r_{T,ET} + \alpha_{T,P}\Delta r_{T,P} \qquad (3)$$

This equation employs the regression relation estimated in equation 2, but allows the coupling strength at each grid cell to change based on the climate model projections. The central assumption in this approach is that the future yield sensitivity of each grid cell responds to future changes in the couplings at the global rate dictated by $\alpha_{T,ET}$ and $\alpha_{T,P}$. We note that successful crop adaptation may challenge this assumption (see Conclusions).

To ease the physical interpretation of the projected yield impacts, we convert the projected change in yield sensitivity to dimensional terms using:

$$\Delta B_T = \Delta\beta_T \frac{\sigma_Y}{\sigma_T} \qquad (4)$$

where ΔB_T coefficients have units of tons ha^{-1} °C^{-1}. We then project additional yield impacts of warming for each grid cell due to changes in coupling ($\Delta\Delta Y$) by multiplying this coefficient by

the multi-model median of the mean seasonal warming by 2051-2100 (ΔT, computed by differencing modeled mean seasonal temperatures between the future and historical periods):

$$\Delta\Delta Y = \Delta B_T \Delta T \qquad (5)$$

We present this additional yield impact as a percent of recent local yields averaged over 2004-2013, the 10 most recent years in our dataset, to contextualize the changes relative to local baseline yields. Finally, we average the percent yield changes across all grid cells with significant historical yield sensitivities to estimate net global additional yield impacts due to future changes in temperature-moisture couplings. Note that we map $\Delta r_{T,ET}$, and $\Delta r_{T,P}$ over the full global cropland, regardless of the significance of historical yield sensitivities, to enable interpretation of wider global patterns of change. However, we map $\Delta\Delta Y$ and $\Delta\beta_T$ only where historical yield sensitivity to temperature (β_T) is significant ($P < 0.1$). We also show projected yield change from warming alone to contextualize $\Delta\Delta Y$, however we do not consider these projections themselves to be a methodological improvement on past statistical yield projections using more complex models.

To assess uncertainty across the ensemble of climate models, we recompute equations 3-5 using model-specific changes in the couplings, rather than the ensemble median. We use a consistent multi-model median warming to compute additional yield impact so that the uncertainty analysis isolates differences between model-specific projected changes in couplings, rather than model differences in mean warming. This approach assumes that, at the seasonal scale, the influence of coupling changes on mean warming in each model is small relative to the radiative effect of greenhouse gases and dominant climate feedbacks (e.g. ocean and cloud responses to warming) (M. M. Vogel et al., 2017).

We then assess model agreement on the sign of yield change for each grid cell. To do so, we classify whether at least 8 models (2/3 of the ensemble) project either positive change (>10%

yield gain), negative change (>10% yield loss), or little change (<10% yield gain or loss). Grid cells where fewer than 8 models agree on the direction of change are classified as areas with substantial model disagreement. We also present histograms of model-specific projected net mean global yield change to reflect the distribution of plausible future global impacts. To account for uncertainty over future emissions, we include in this histogram equivalent results for a high-emissions scenario, SSP5-8.5 (Eyring et al., 2016). We also present $\Delta\Delta Y$ for this scenario to understand the spatial pattern of changes. Finally, we present $\Delta\Delta Y$ for the two emissions scenarios averaged over several regions with noteworthy vulnerability or global importance. The data and methods used in this study are summarized visually in Appendix B Figure 7. Base maps in Figures 1 and 4-6 are developed by Generic Mapping Tools and used under a creative commons license.

Appendix B

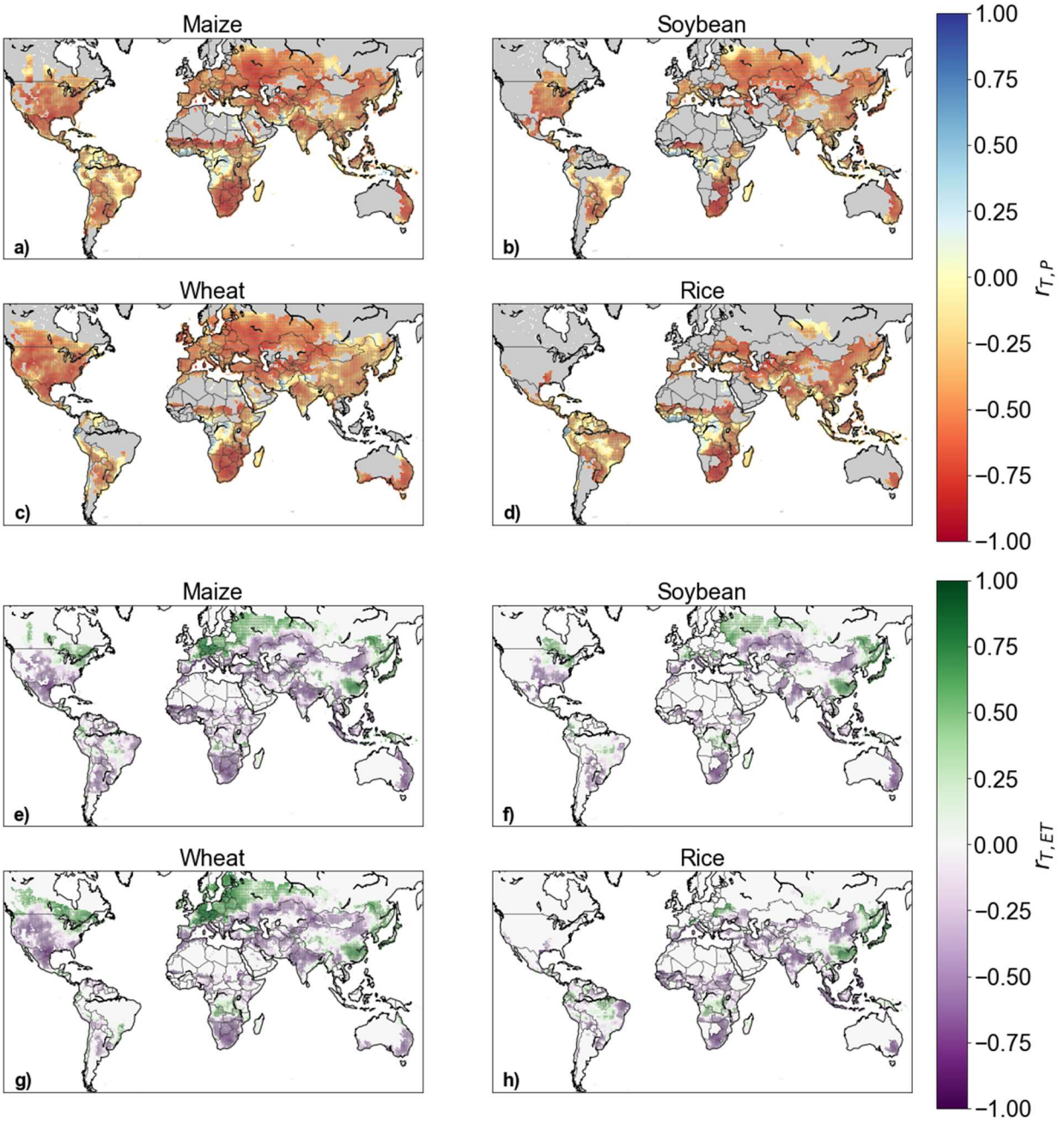

Appendix B Figure 1: Temperature-moisture couplings across global croplands during different cropping seasons. Circulation coupling strength, measured as the interannual correlation between detrended growing season mean temperature and total precipitation, during the local growing seasons of a) maize, b) soybean, c) wheat, and d) rice. Land-atmosphere coupling, measured as the interannual correlation between detrended growing season mean temperature and evapotranspiration, during the local growing seasons of e) maize, f) soybean, g) wheat, and h) rice. Hatching denotes significance of the correlation (two-tailed $p < 0.1$, t-test).

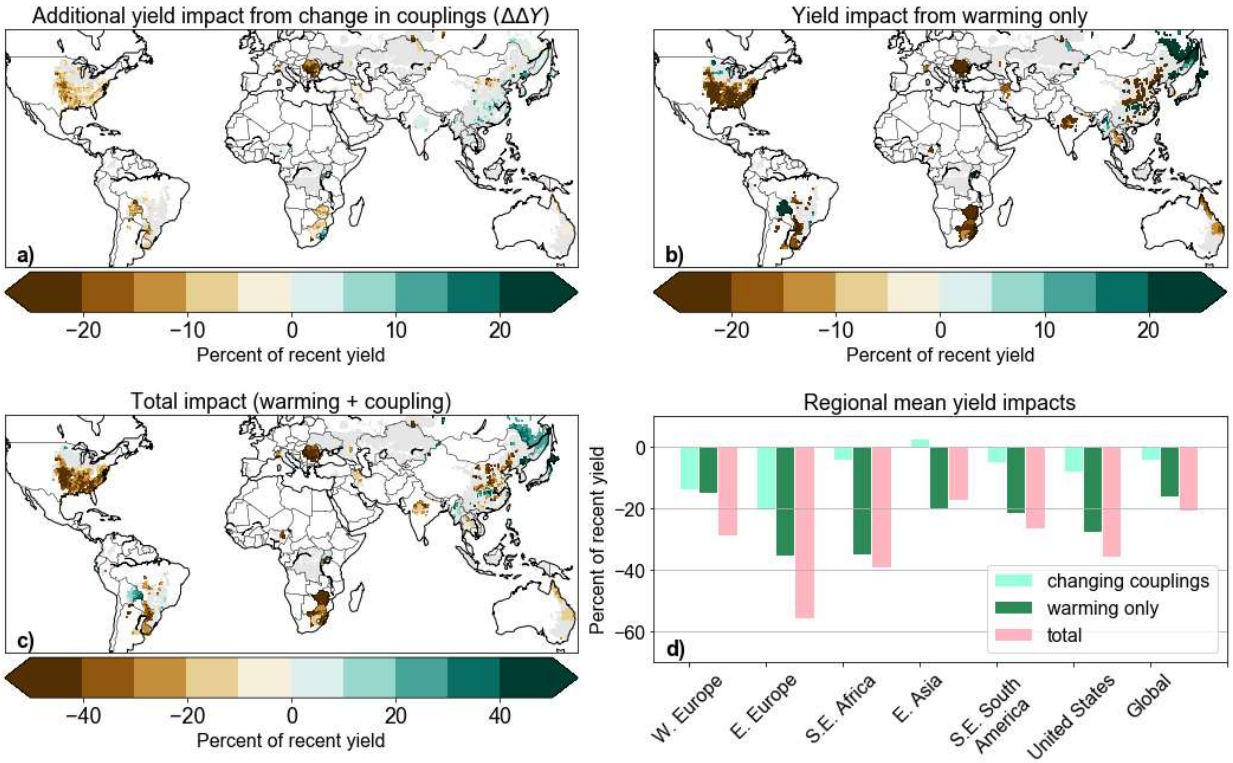

Appendix B Figure 2: Projected additional impact of future warming on soybean yields due to changing temperature-moisture couplings. a) Ensemble median additional impact of warming on soybean yields from projected changes in $r_{T,ET}$ and $r_{T,P}$ over 2051-2100 under a moderate emissions scenario (SSP2-4.5), as a percent of local mean of recent yields (2004-2013). b) Soybean yield changes (as a percent of recent yield) from ensemble median warming only, projected using historical yield sensitivity to temperature from Fig. 1b. c) Projected total yield impacts, estimated as the sum of impacts from changing couplings and warming only. Projections in a-c) are shown only for areas with significant historical soybean yield sensitivity to temperature ($p < 0.1$); gray shading shows croplands with insignificant yield dependence on temperature. d) Yield impacts averaged across selected key regions and globally

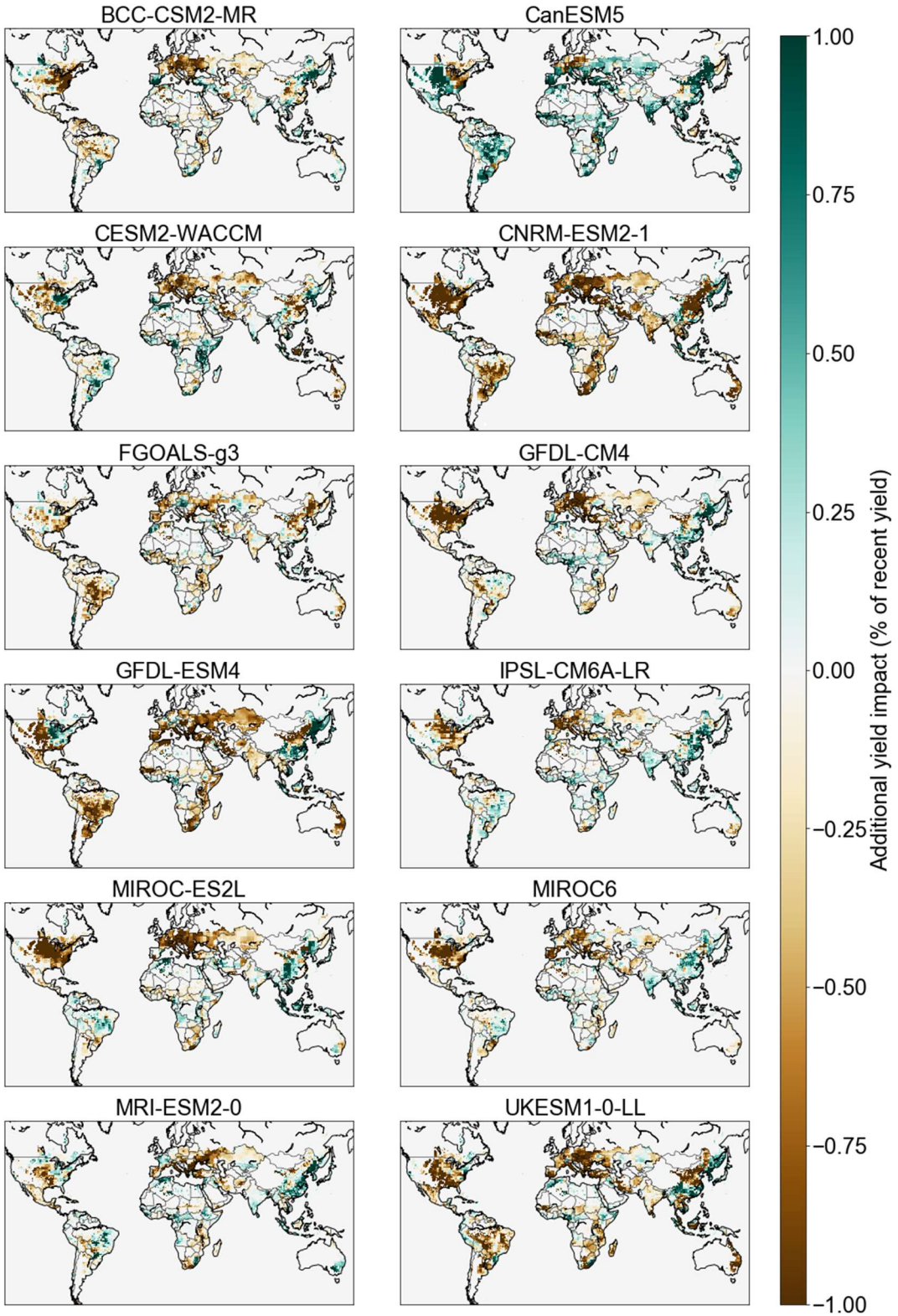

Appendix B Figure 3: Model specific projected additional yield impact ($\Delta\Delta Y$) due to changing temperature-moisture couplings. Same as Fig. 5a, but for individual CMIP6 climate models run under the moderate emissions (SSP2-4.5) scenario.

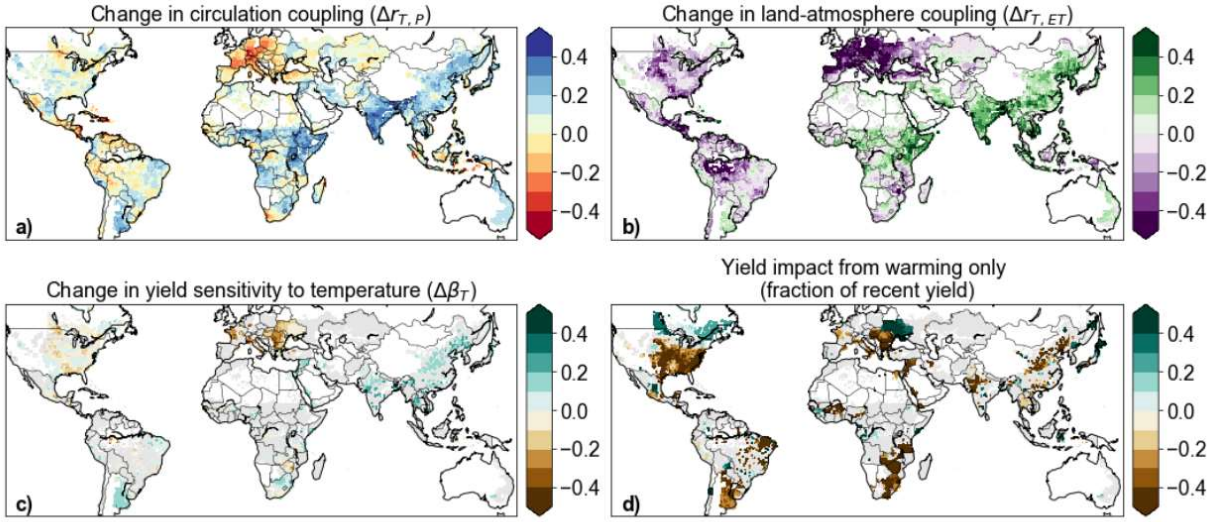

Appendix B Figure 4: Projected future changes in temperature moisture couplings and yield sensitivity in response to warming under a high emissions scenario. a) Projected change in circulation coupling (detrended interannual $r_{T,P}$) over 2051-2100 under a high emissions scenario (SSP5-8.5), compared to historical couplings over 1961-2010. The median of an ensemble of 12 CMIP6 climate model projections is shown for each grid cell. b) Same as a), but for land-atmosphere coupling ($r_{T,ET}$). c) Projected change in standardized maize yield sensitivity to temperature in response to changes in couplings, based on global slope coefficients from in Fig. 2a. d) Projected yield impact due to temperature warming only, expressed as a fraction of recent yields. For a-b) projections are shown over the full global maize croplands to facilitate interpretation of broader patterns, while for c-d) projections are shown only for areas with significant historical maize yield sensitivity to temperature ($p < 0.1$); gray shading shows croplands with insignificant yield dependence on temperature.

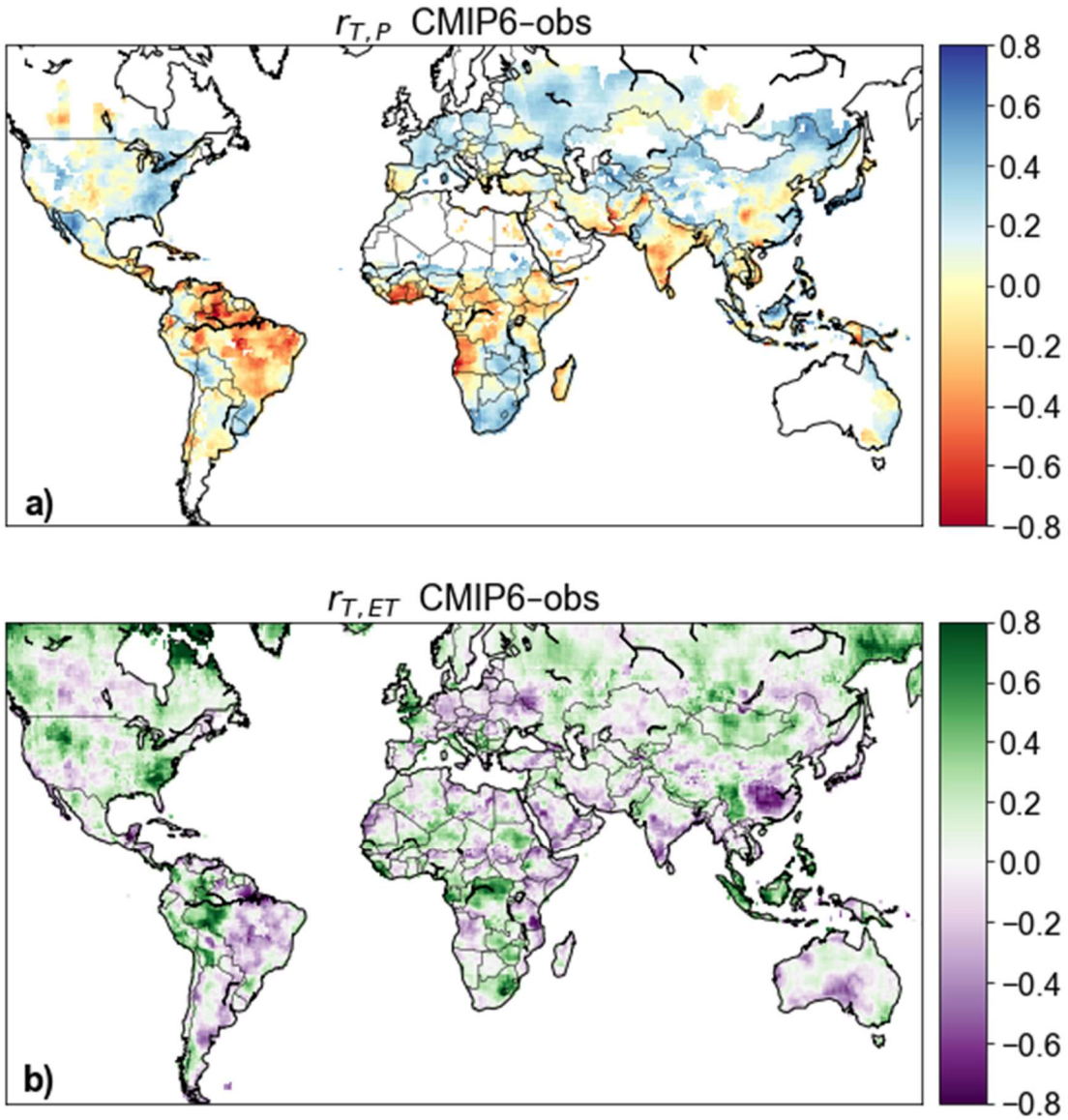

Appendix B Figure 5: Comparison of historical temperature-moisture couplings between CMIP6 models and observation-based datasets. a) Difference in circulation coupling strength, measured as the interannual correlation between detrended growing season mean temperature and total precipitation, between CMIP6 historical run ensemble median and historical observation-based data (Hadley Center CRU TS4.02). b) Difference in land-atmosphere coupling strength, measured as the interannual correlation between detrended growing season mean temperature and evapotranspiration, between CMIP6 historical run ensemble median and historical observation-based data (GLDAS Noah land surface model L4, version 2.0).

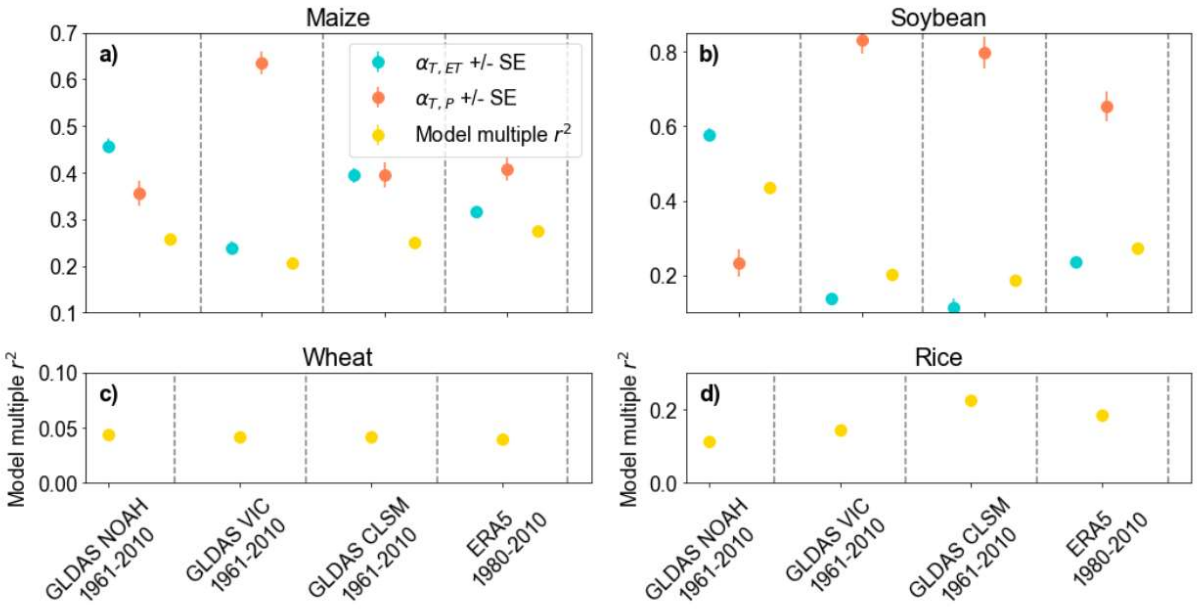

Appendix B Figure 6: Dependence of yield sensitivity to temperature on temperature-moisture couplings using alternative historical observation-based datasets. Slope coefficients (+/- standard error, blue and pink points) and/or coefficients of variation (gold points) for regression model in Equation 2 (see Methods) and Figure 2, re-estimated using the primary and 3 alternative historical observation-based data for a) maize, b) soybean, c) wheat, and d) rice.

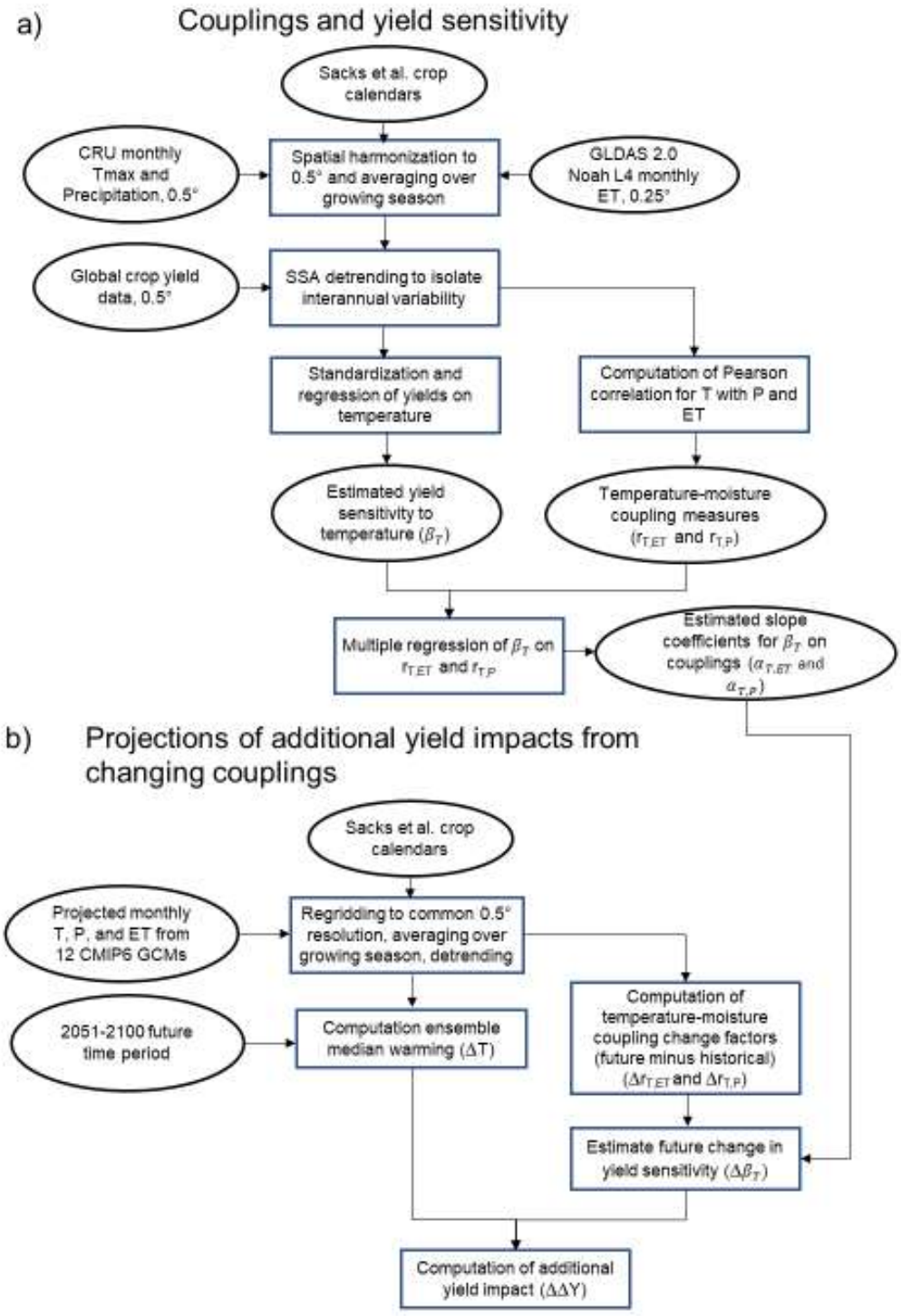

Appendix B Figure 7: Summary of data and methods used for historical analysis and projections. Flowchart describing sequence of methods employed for a) temperature-moisture coupling measure and yield sensitivity estimation, and b) projection of additional yield impacts from changes in couplings projection. Elliptical elements depict data inputs or outputs, while rectangular elements depict computations.

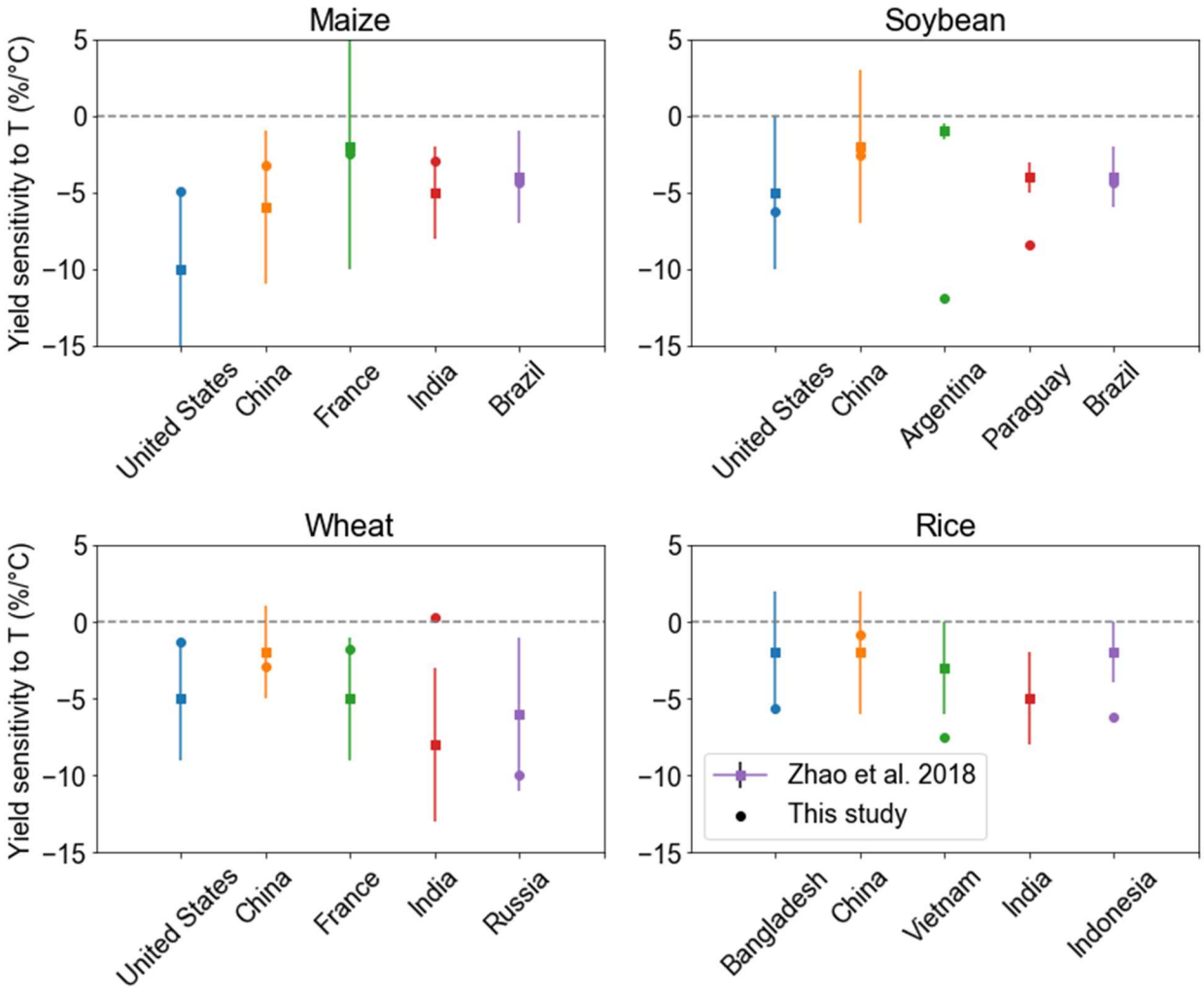

Appendix B Figure 8: Comparison of yield sensitivity to temperature between this study and multi-model intercomparison. Unstandardized yield sensitivity to temperature (in % per °C) as estimated in this study (circles) and in the intercomparison of statistical and mechanistic crop models in Zhao et al. (2018, ref. 4) (squares, lines denote 95% confidence interval). Yield sensitivities in this study were averaged to the national scale to match the resolution of ref. 4.

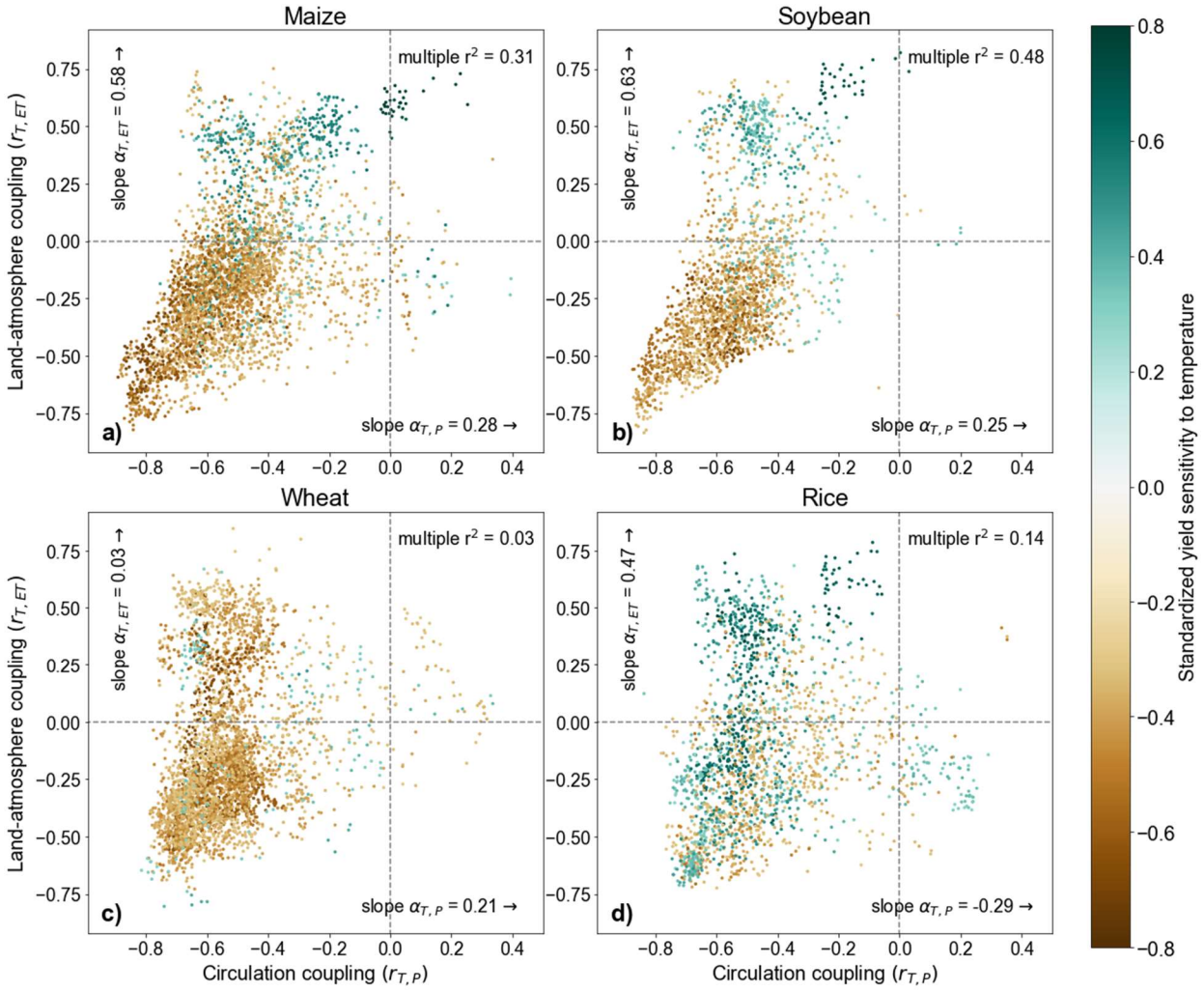

Appendix B Figure 9: Global dependence of yield sensitivity to temperature on two temperature-moisture couplings using a stricter significance criterion. Same as Figure 2, except using $p < 0.05$ as significance threshold on the yield-temperature slope coefficient for inclusion in the sample.

Appendix B Table 1: Dataset references and access information.

Dataset name	Access link
Gridded sub-national crop statistics for ~20,000 political units, 0.5°	Available upon request
HadCRU TS4.02 Gridded Observations, 0.5°	http://dx.doi.org/10.5285/b2f81914257c4188b181a4d8b0a46bff
GLDAS V2.0 Noah model L4 LSM, 0.25°	https://disc.gsfc.nasa.gov/datasets/GLDAS_NOAH025_M_2.0/summary?keywords=gldas
GLDAS V2.0 CLSM model L4, 1.0°	https://disc.gsfc.nasa.gov/datasets/GLDAS_CLSM10_M_2.0/summary?keywords=gldas
GLDAS V2.0 VIC model L4, 1.0°	https://disc.gsfc.nasa.gov/datasets/GLDAS_VIC10_M_2.0/summary?keywords=gldas
Sacks et al. Crop Calendar Datasets, 0.5°	https://nelson.wisc.edu/sage/data-and-models/crop-calendar-dataset/index.php
ERA5 Reanalysis Monthly Averages, 0.25°	https://doi.org/10.24381/cds.f17050d7
CMIP6 Historical Climate and ScenarioMIP Projections	https://console.cloud.google.com/storage/browser/cmip6

Chapter 3: Mitigation and Adaptation Emissions Embedded in the Broader Climate Transition

1) Introduction

The diverse dangers of human-induced climate change demand two major international efforts: reducing greenhouse gas (GHG) emissions enough to keep warming below a specified limit (Knutti et al., 2016; Rogelj et al., 2018; Schleussner et al., 2016; Seneviratne et al., 2016), and adapting infrastructure and patterns of human settlement to support societal goals at that level of warming (Diaz, 2016; Hauer et al., 2020; Lincke & Hinkel, 2021; Siders et al., 2019; Viguié et al., 2021). The twin global projects of climate mitigation and adaptation can be characterized as two components of a *broader climate transition*, in which temperatures stabilize and societies are adapted to the impacts. Such a transition will involve a significant investment of economic activity and energy use, which will generate CO_2 emissions as long as they are powered by fossil fuel combustion.

Among a wide array of potential mitigation and adaptation measures, we select three illustrative examples that are particularly widely required, energy intensive, and likely to be deployed (see Methods). First, mitigating CO_2 emissions from the energy sector necessitates the mass construction of renewable electricity generating capacity (Gambhir et al., 2019; Jacobson et al., 2017; Keyßer & Lenzen, 2021; Luderer et al., 2021; Rogelj et al., 2018; Van Vuuren et al., 2016). Because renewable capacity is presently insufficient, this process of *energy decarbonization* must be initially powered by an investment of fossil fuel energy, or *seed energy* (Sgouridis et al., 2016). Second, sea-level rise (SLR) caused by historical and future emissions will require the construction of coastal flood defenses and relocation of coastal settlements across

a potentially vast portion of the global coastline (Diaz, 2016; Hinkel et al., 2014; Lincke & Hinkel, 2021). Third, climate warming due to historical emissions will make space cooling necessary in new regions, and increase the duration and intensity of its use globally (Levesque et al., 2018; Viguié et al., 2021).

Refining estimates of remaining carbon budgets as a measure of the emissions 'runway' for the transition to a stable climate has been a topic of great importance to climate policy and Earth system science (Matthews et al., 2020). Emissions from mitigation and adaptation effectively reduce the space available for remaining CO_2 emissions in other economic sectors. Much effort has been devoted to understanding the economic costs of mitigation (Jacobson et al., 2017; Rogelj et al., 2013) and adaptation (Diaz, 2016; Hinkel et al., 2014) needed to achieve the broader climate transition. The likely carbon emissions cost of the transition itself, by contrast, has received less attention (Myhrvold & Caldeira, 2012; Seto et al., 2016).

Energy use for the clean energy transition has been suggested as a potentially large source of emissions (Luderer et al., 2018; Sers & Victor, 2018; Sgouridis et al., 2016; Tong et al., 2019), but a holistic global estimate of the aggregate magnitude of these emissions is presently lacking. Further, while energy demand for projected future space cooling has been studied in some regions (Viguié et al., 2021), likely emissions from this and other projected adaptations to climate change remain poorly understood. Thus, the potential for mitigation and adaptation emissions to effectively shorten the emissions runway, or necessitate shifts in economic priorities and investments to respect carbon budgets, remains largely unconstrained.

In this study, we provide an estimate of CO_2 emissions likely to result from mitigation and adaptation across the transition to a stable climate over 2020-2100 using a suite of climate and sectoral models. We first quantify the emissions embedded in a gradual 2°C-consistent transition

to determine if their magnitude is substantial from a policy and Earth system perspective. We then reassess these transition emissions under rapid and delayed energy decarbonization pathways to assess their sensitivity to climate ambition. We finally identify and discuss key uncertainties and leverage points for addressing potentially important emissions from mitigation and adaptation.

2) Results

We first present the simulated 2°C gradual energy decarbonization pathway, ensuing climate changes, projected adaptations, and estimated energy embedded in the transition. We then report estimates of embedded emissions for the energy decarbonization pathways and the adaptation interventions. Finally, we detail the emissions implications of a more gradual energy decarbonization scenario.

Projected rapid energy decarbonization pathway, climate change, and adaptation

Under the gradual energy decarbonization pathway projected using NETSET, wind and solar capacity is rapidly deployed beginning in 2020 with installation rates averaging 4.5TWp/yr over 2020-2050 (Fig. 1a). Solar and wind capacity plateaus at ~100TWp by 2050, satisfying ~80% of global primary energy demand (Fig. 1a). This deployment of solar and wind – along with smaller increasing contributions from geothermal and scale-limited renewables – drives the displacement of fossil fuels. The required energy seed totals 930PWh (3350EJ) over 2020-2100, of which 405PWh (1460EJ) or 43% are provided by fossil fuels (Fig. 1e). To put these numbers in perspective, the world consumed 155 PWh (560EJ) of primary energy in 2020.

Projected future CDDs continue to rise with global climate warming through the 2060s and then plateau through 2100, peaking at around 13% above 2020 levels (Fig. 1b, pink line). By

contrast, projected SLR proceeds steadily reaching a global mean of 50cm by 2100 compared to 2000 (Fig. 1b, blue line), reflective of the slower and higher-inertia response of oceans and cryosphere to warming. As a result of this SLR, we project based on CIAM that over the 2050-2100 planning period, protective infrastructure will be cost-optimal over 31,000km of coastline or around 3% of the global coastline, protecting 130 million people (Fig. 1c, Appendix C Fig. 1a). The median optimal protection height is around 1m, excluding wave run-up and initial under-protection. Some degree of coastal retreat would be cost optimal across a much larger ~70% of coastal segments, representing 67 million people globally (Fig. 1d, Appendix C Fig. 1b). These projections are comparable to other recent estimates (Lincke & Hinkel, 2021). Coastline segments where neither retreat nor protection are optimal are concentrated in sparsely populated desert and high latitude areas (Appendix C Fig. 1). Protected segments tend to be more densely populated (by a median factor of 5) and have higher climatological 1-in-1-year storm surges (by ~25%) than segments where retreat is optimal (Appendix C Fig. 1c-f).

Renewable energy deployment and adaptation result in energy demands throughout the 21st Century. Fossil fuel seed energy (i.e., fossil fuel investment into deploying renewables, Fig. 1e purple curve) peaks in the 2020s before rapidly being replaced by renewable seed energy (Fig. 1e, yellow curve), which reaches steady state by around 2070. As a result of projected higher CDDs, energy demand for climate-adaptive space cooling is projected by EDGE to rise gradually throughout the century to around 5EJ/year by 2100 (Fig. 1e, pink curve). Finally, using factors from Hammond et al. (2008) and Monahan et al. (2011), we estimate that energy embedded in coastal adaptations amounts to around 20EJ for retreat and 25EJ for protection in aggregate over 2020-2100, which we present as occurring at the midpoint of the transition in 2060 (Fig. 1e, squares, see Methods).

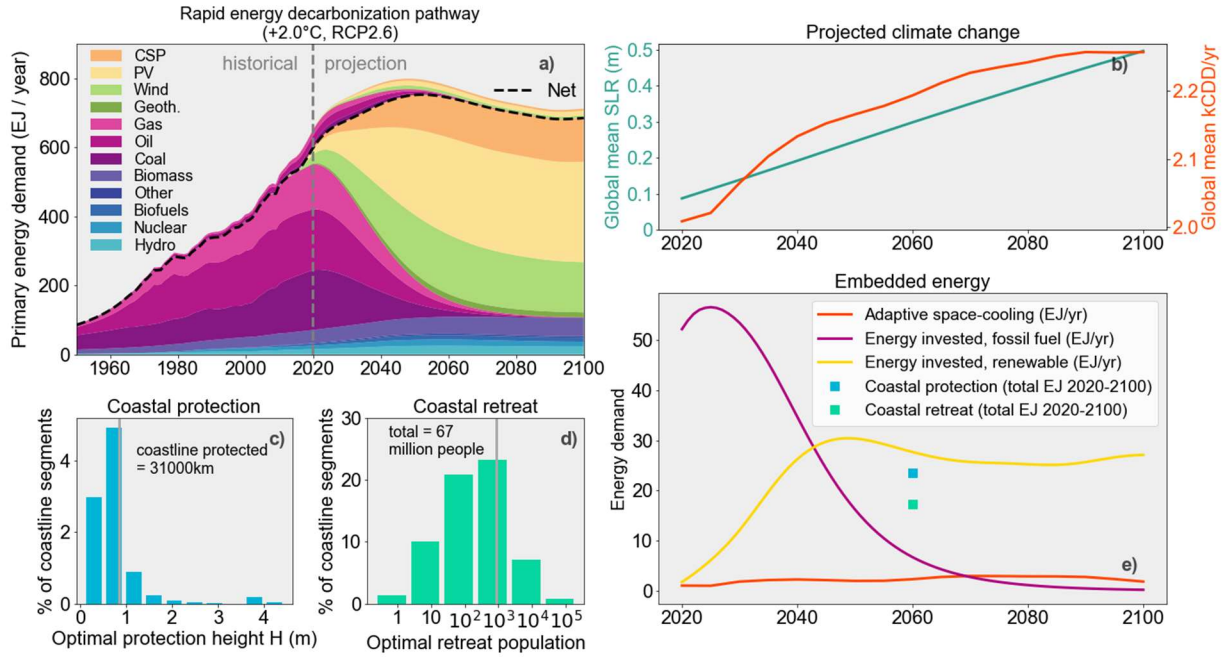

Figure 1: Energy demands from simulated rapid energy decarbonization and adaptation. a) Gradual 2°C energy decarbonization pathway projected using the NETSET global energy model (respecting a carbon budget of 1150GtCO$_2$ and minimum net energy per capita of 2000W). Coloured areas depict time evolution of primary energy demand across energy sources. The dotted black line separates energy investment into energy (above) from net energy available to society (below). The dotted grey line separates historical from projected data. b) Projected climate change forced by GHG emissions under RCP2.6, which results in an increase in population-weighted global mean cooling degree days (CDD, pink curve) and global mean SLR (blue curve). c) Distribution of cost-optimal coastal protection heights (by coastline segment) over the 2050-2100 planning period, projected using the CIAM model. The total coastline protected is the sum of the lengths of protected coastline segments. d) Same as c, but for cost-optimal retreat population. Note that retreat population is presented on a logarithmic axis. e) Time evolution of energy demand embedded in adaptation and energy decarbonization over 2020-2100. Coastal retreat and protection are presented as totals over 2020-2100, assumed to occur at the midpoint of the transition in 2060.

Substantial emissions embedded in the rapid energy decarbonization pathway

The CO_2 emissions resulting from the energy demand for adaptation and the energy decarbonization pathway depend on the emissions intensity of energy, which we derive from EIA global energy statistics in the 2019 International Energy Outlook. We estimate the average emissions intensity of major fossil fuels to be around 90tCO$_2$/TJ for coal, 60tCO$_2$/TJ for oil, and

50tCO_2/TJ for natural gas (Table S1). Based on these emissions factors, the evolution of the energy mix through the transition, and the fuel composition of seed energy for renewables (Fig. 1a), we project that the emissions from energy investment into energy peak in 2025 at 3.8$GtCO_2$/yr before steeply declining (Fig. 2a), as renewable energy replaces fossil fuels both in the overall energy mix and in energy investment into renewables. In total over 2020-2100, coal contributes 35$GtCO_2$, oil around 37$GtCO_2$, and gas around 23$GtCO_2$ for a total of 95$GtCO_2$, equivalent to 2.5 years of current global emissions and over 8% of the remaining carbon budget for 2°C (Fig. 2b).

Smaller emissions from adaptation through the transition

Emissions from adaptive cooling peak around 2030 at ~70$MtCO_2$/yr, about 2% of the peak seed energy emissions (3.8$GtCO_2$), before declining steeply beginning in the 2040s (Fig. 2c). This decline occurs even as adaptive cooling energy demand rises (Fig. 1e), compensated by reductions in the emissions intensity of energy as renewables displace fossil fuels (Fig. 1a). Following our partitioning scheme for process versus energy emissions embedded in coastal adaptation materials, the emissions intensities of sea dikes and coastal resettlement decline rapidly as fossil fuels are phased out, falling below half their present values by the assumed time of adaptation 2060 (dotted grey line, Fig. 2d-e). Thus, by the time coastal adaptation occurs in our model, it is reliant on a cleaner energy mix. While energy-related emissions dominate process emissions at the start of the transition (by a factor of 1.5 for dikes and 4 for resettlement), they contribute <10% of emissions by 2060 and thus drive the declining emissions intensity (Fig. 2d-e). In aggregate over 2020-2100, coastal protection contributes ~1$GtCO_2$ while coastal retreat and adaptive cooling each contribute around 0.3$GtCO_2$ (Fig. 2f). Total adaptation emissions through 2100 are thus much smaller than emissions from fossil fuel energy investment into renewable capacity, amounting to 1.5$GtCO_2$ or

around 0.1% of the remaining carbon budget, with a dominant share arising from coastal protection.

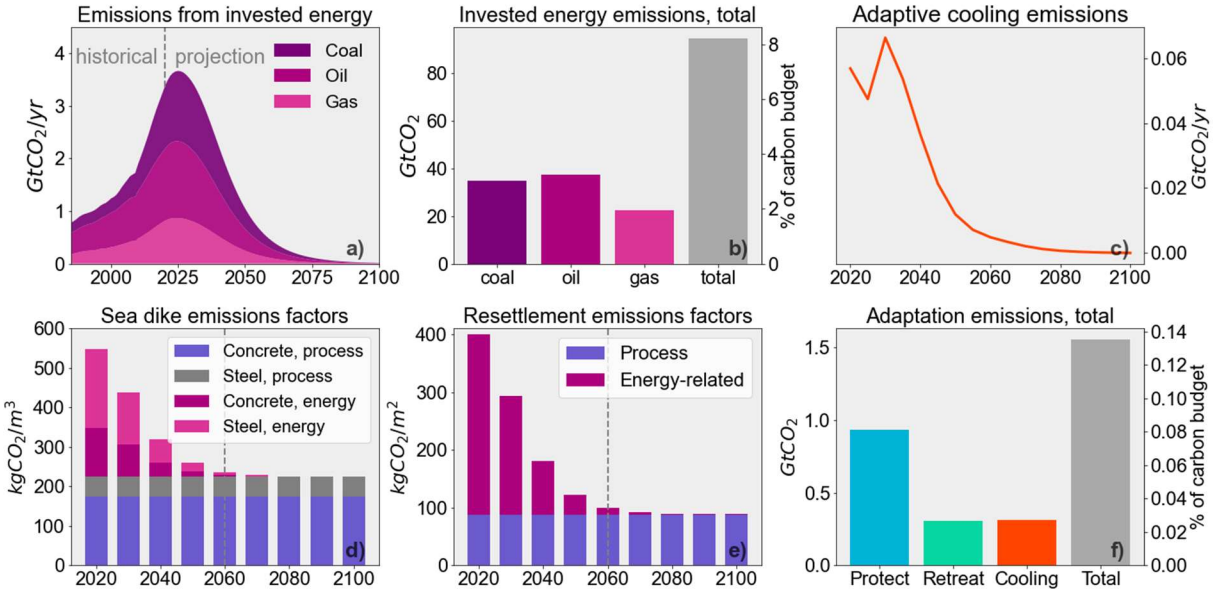

Figure 2: Estimated mitigation and adaptation CO_2 emissions embedded in the transition. a) Time evolution of emissions from fossil fuel energy investment into renewable energy as projected in NETSET. Dotted vertical line separates historical from projected data. b) Total emissions from fossil fuel energy investment into renewable capacity over 2020-2100 in absolute units and as a percent of the remaining carbon budget for 2°C. c) Time-evolution of adaptive cooling emissions based on energy demand from EDGE and energy mix from NETSET. d) Estimated emissions factors over time by source for materials in modeled sea dike. e) Estimated emissions factors over time by source for resettlement housing. Data in d-e) are based on LCA literature and decarbonization of energy mix as projected in NETSET, and vertical dotted line denotes the midpoint of the transition, at which coastal adaptations are assumed to take place. f) Total emissions from coastal retreat, coastal protection, and adaptive cooling over 2020-2100, in absolute units and as a percent of the remaining carbon budget for 2°C.

Strong sensitivity of transition emissions to the pace of decarbonization

Under rapid energy decarbonization limiting warming to 1.5°C, the renewable capacity installation rate averages 5.9TWp/yr over 2020-2050, 30% greater than the rate of the gradual pathway, and peaks strongly in the 2020s at over 10TWp/yr (Fig. 3a). As a result, fossil fuels are virtually eliminated from the energy mix by 2030, and renewable deployment is powered by reinvestment

of renewable energy thereafter (Appendix C Fig. 2b). This minimizes seed energy emissions to 20GtCO_2, an 80% reduction compared to gradual decarbonization (Fig. 3c).

By contrast, a cumulative 180GtCO_2 emissions result from renewable energy deployment under delayed decarbonization (Fig. 3b), nearly double those from the gradual pathway and 9 times greater than the rapid case (Fig. 3c). The mean installation rate of renewable capacity (2.6TWp/yr over 2020-2050) is roughly halved compared to the rapid transition (Appendix C Fig. 2a). This leads to a higher share of fossil fuels in the energy mix throughout the 21st Century (e.g., 47% in 2050, compared to 15% under gradual and <1% under rapid, Fig. 3c). Consequently, a majority of energy investment into renewables is derived from fossil fuels (73% in total over 2020-2100, compared to 43% under gradual and 11% under rapid decarbonization, Appendix C Fig. 2b).

Avoided emissions under rapid decarbonization limit climate change and projected adaptation. Sea levels rise by 14% less than under gradual decarbonization (43cm by 2100, Appendix C Fig. 2c), resulting in a 10% decrease in coastal protection (although retreat population rises by 4%). Under the delayed transition, greater total emissions accelerate global mean SLR (60cm by 2100, or 20% more than the gradual transition, Appendix C Fig. 2c), resulting in 13% more coastal protection and an 11% larger retreat population than under rapid decarbonization. Projected CDDs are boosted by 8% under delayed decarbonization and reduced by 4% under rapid decarbonization, compared to the gradual transition by 2100 (Appendix C Fig. 2c).

Adaptation emissions increase non-linearly with cumulative emissions across the pathways. Total adaptation emissions are reduced by 20% to 1.2GtCO_2 under rapid decarbonization compared to the gradual case, but triple under the delayed pathway for a total of 4.5GtCO_2 over 2020-2100 (Fig. 3c). Reductions in emissions with rapid decarbonization are dominated by an 80% reduction in cooling emissions. Conversely, emissions from all adaptations

expand substantially in the delayed pathway, increasing by ~80% for coastal protection (from 1 to 1.8GtCO_2), by a factor of 2.7 for coastal retreat (0.3 to 0.8 GtCO_2), and by a factor of 6.7 for adaptive cooling (0.3 to 2.0GtCO_2).

These increases in adaptation emissions are driven primarily (~90%) by an increased global emissions intensity of energy as the decarbonization pace slows (light grey bars in Fig. 3c), with a secondary contribution of ~10% from a higher amount of adaptation (i.e., higher energy demand, dark grey bars in Fig. 3c). Increased emissions from cooling are additionally raised by lower primary-to-final conversion efficiency of fossil fuels compared to renewables, boosting primary energy demand by 30% under delayed compared to rapid decarbonization (Appendix C Fig. 2c). Thus, fractional changes in adaptation emissions resulting from slower transitions far exceed the fractional change in adaptation amounts driven by geophysical climate impacts, because the resulting adaptation energy demand is met by far ‘dirtier ’energy.

Despite large absolute increases in embedded emissions embedded across the transition scenarios, their percentage of respective carbon budgets is relatively static (5.5% for rapid, 8.3% for gradual, and 8.6% for rapid decarbonization, Fig. 3c-d). However, as a point of comparison, the total emissions embedded in the delayed transition, the pathway most consistent with current global climate policy, amount to 16% if applied to of the 2°C carbon budget, and 46% if applied to the 1.5°C carbon budget. This comparison demonstrates that under current policies, the emissions embedded in the broader climate transition alone jeopardize the 1.5°C target, highlighting a novel contradiction between global climate commitments and actual policies.

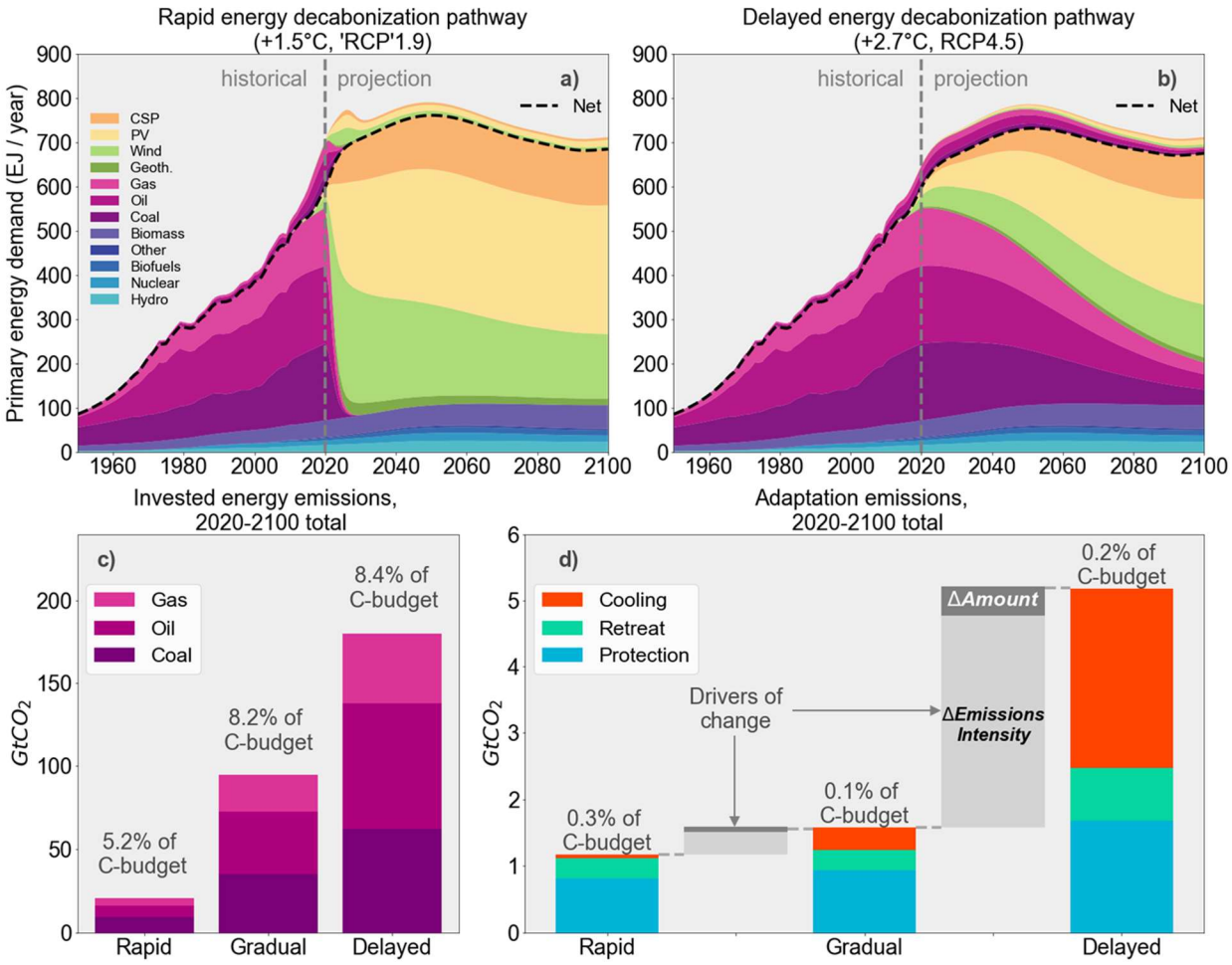

Figure 3: Comparative mitigation and adaptation CO_2 emissions from a rapid versus gradual transition. a) Rapid energy decarbonization pathway limiting warming to 1.5°C (same as Fig. 1a, except respecting a smaller carbon budget of 400$GtCO_2$). Coloured areas depict time evolution of primary energy demand across energy sources. The dotted black line separates energy investment into energy (above) from net energy available to society (below). The dotted grey line separates historical from projected data. b) Same as a) but for the delayed energy decarbonization pathway with warming ~2.7°C in 2100 (respecting a larger carbon budget of 2150$GtCO_2$). b) Total emissions from fossil fuel energy investment into renewable capacity over 2020-2100 for the three decarbonization pathways. Annotations show emissions as percentages of *respective* carbon budgets. c) Total emissions from coastal retreat, coastal protection, and adaptive cooling over 2020-2100 for the three decarbonization pathways. Grey floating bars show drivers of change in total adaptation emissions between the three cases, partitioned (as an average across the three adaptations) into a component due to change in amount of adaptation versus change in emissions intensity of primary energy.

3) Discussion and Conclusions

We estimate that over 2020-2100, a cumulative ~97GtCO_2 of emissions are embedded in energy decarbonization and major adaptations comprising the broader climate transition. These emissions are dominated by seed energy emissions (i.e., fossil fuel combustion to power renewable energy deployment, 95GtCO_2), with a smaller contribution from adaptive cooling and coastal protection and retreat (1.5GtCO_2, Fig. 2). Our estimates are by definition conservative since they exclude non-CO_2 GHGs, other adaptations such as inland flood protection (Dottori et al., 2018) and water transfer infrastructure (Qin et al., 2020), and other energy system changes like building retrofits, carbon capture and storage, and renewable energy transmission and storage (MacDonald et al., 2016; Zeyringer et al., 2018). Despite this, our estimated magnitude of mitigation and adaptation emissions embedded in the transition is sizeable and relevant to climate policy from several angles.

First, the emissions embedded in the transition are equivalent to a substantial mitigation effort. For instance, emissions under gradual decarbonization are 2.5 times (or 5 times for delayed decarbonization) larger than the total global emissions reductions attributable to national CO_2 abatement legislation over 1999-2016 (Eskander & Fankhauser, 2020). Further, they are on the order of (or for delayed decarbonization, about double) the emissions abatement from the United States hypothetically achieving net zero CO_2 emissions by 2050 (i.e., reducing emissions from ~5 to 0GtCO_2/yr over 30 years would avoid 75GtCO_2/yr, compared to constant emissions) (US Environmental Protection Agency, 2021). Relative to these measures, the emissions embedded in the transition are equivalent to a considerable climate legislative and mitigation effort. The emergence of these emissions in coming decades, which we argue is not currently widely

researched or included in policy debates, has the potential to further complicate the challenge of meeting both adaptation and mitigation targets.

Second, total transition emissions represent a non-negligible 5-8% of the remaining carbon budget under the respective scenarios. Furthermore, under delayed decarbonization, total transition emissions amount to 16% of the carbon budget for 2°C, and 46% of the carbon budget for 1.5°C. We argue that these mixed comparisons are not contradictory, but rather accurately reflect the current global gap between climate commitments and actions. While international agreements affirm well below 2°C and ideally 1.5°C as a maximum warming target, national policies are in aggregate more consistent with the ~2.7°C gradual transition scenario (Canadell et al., 2021; UNEP, 2020).

Thus, under current policies, emissions embedded in the transition alone jeopardize the 1.5°C target, but can minimized under decarbonization policies consistent with 1.5°C. Nevertheless, since carbons budgets are commonly interpreted as the emissions runway prior to which global emissions much reach net zero (Matthews et al., 2020), our results may imply that a non-negligible portion of this budget may need to be set aside for renewable seed energy and adaptation, effectively shortening the runway for other economic sectors. However, this implication of our results depend on whether these emissions should be regarded as outside (i.e., additional to) existing accounting of present and likely future emissions. We note a few considerations on this topic.

First, to our knowledge, projected emissions from adaptation are not included in mitigation scenarios generated by integrated assessment and other models, except insofar as climate damages affect economic drivers (De Cian et al., 2016; Fisher-Vanden et al., 2013). They thus are not widely considered in current policy assessments informed by these models. Second, some energy

investment into renewable capacity will replace fossil fuel infrastructure at its planned retirement, representing capacity maintenance without net new energy demand. However, some degree of early retirement will be necessary for to achieve more ambitious pathways (Pfeiffer et al., 2018; Tong et al., 2019). From this perspective, the additionality of seed energy emissions would be larger for faster-paced transitions necessitating more abandonment of fossil fueled capacity, a factor worthy of future examination. Third, as with historical infrastructure investments, the interventions that we examine may stimulate household consumption and economic growth in other sectors. Prior to radical decarbonization of energy or decoupling of economic growth from energy, this would augment emissions (Fankhauser & Tol, 2005; Grubler et al., 2018; Horen Greenford et al., 2020; Keyßer & Lenzen, 2021). However, the economic activity comprising the transition could also divert economic growth from sectors that shrink during the transition. In short, questions surrounding the additionality of transition emissions are complex, consequential, and worthy of further research.

We find that emissions embedded in the transition are highly sensitive to transition pace. For instance, under delayed decarbonization, seed energy emissions increase nearly tenfold, while adaptation emissions quadruple compared to the rapid 1.5°C pathway (Fig. 3). This sensitivity arises mainly because the rate of renewable energy reinvestment into more renewables is limited importantly by slower deployment pace under a delayed transition (Fig. 1a, e, Appendix C Fig. 2b), which strongly boosts the fossil-fuel seed energy emissions (Fig. 3b), akin to an ‘emissions trap ’(Sers & Victor, 2018). Adaptation emissions contribute secondarily to the sensitivity, partly because slower transitions result in more climate change and thus more adaptation, but mainly because they draw on a more emissions-intensive energy mix (Fig. 3c, Appendix C Fig. 2).

Emissions embedded in the transition are thus strongly sensitive to the pace of decarbonization and, consequently, low climate ambition comes at a high transition emissions cost.

We show that seed energy for renewable capacity is likely to comprise the bulk of transition emissions under the three pathways. Crucially, this implies that the majority of transition emissions are likely unavoidable, as a certain amount of fossil-fuel energy must be used to power initial renewable deployment. Until energy decarbonization has matured sufficiently, the fraction of seed energy that can be satisfied by renewables will be limited by low initial renewable capacity (Appendix C Fig. 2a). Thus, while seed energy emissions can be greatly reduced through ambitious decarbonization (Fig. 3c), they remain non-negligible under all scenarios. By contrast, technologies exist to minimize the energy- and emissions-intensity of adaptation, including nature-based coastal protection (Chu et al., 2012), alternatives to concrete and steel in construction such as engineered wood (Ramage et al., 2017), and passive solar cooling. However, the effectiveness and scalability of these alternatives remains uncertain.

Our results raise some important equity concerns that must be remedied for a just transition. Cost-optimal coastal protection projected using CIAM is more widespread in wealthier countries due to their higher GDP and coastal capital density. By contrast, the sub-Saharan Africa coastline is only protected in a few dense population centers (Appendix C Fig. 1a), forcing the majority of the population to either face rising seas or retreat. Further, wealthier people and countries typically have greater economic energy intensities and thus contribute disproportionately to the carbon cost of deploying renewables. Thus, transition emissions are disproportionately caused by wealthier people, while their impacts are faced disproportionately by those with less wealth, furthering historical inequity surrounding climate change (Hubacek et al., 2017; Matthews, 2016). A greater

commitment of wealthy nations and individuals to equitable financial transfers, priorities, and policies is needed to relegate these unjust outcomes to the past.

As a broad global estimate spanning many complex sectors, our study has five important limitations that may be improved upon in future research. First, although our research provides new insight and groundwork, it should be expanded to account for non-CO_2 emissions (notably N_2O, CH_4, and hydrofluorocarbons) and other positive emissions sources from mitigation and adaptation. Further, in focusing on adaptations with potentially large emissions, we do not target others with potential avoided or negative emissions (for instance, a reduction in heating energy use) which may be included in future studies. Second, future model improvements may integrate dynamic interactions between interventions, such as energy system changes due to SLR impacts on coastal energy infrastructure, which may help elucidate other synergies or trade-offs between mitigation and adaptation. Third, while we omit economic considerations for the sake of tractability, they merit future attention, notably around the function of capital markets, assumptions of energy decoupling from GDP growth, and their influences on evolution of decarbonization and adaptation. Fourth, in the absence of a solid observational basis, we make assumptions about the timing of coastal adaptations, whose influence on transition emissions should be further explored. Finally, although we examine the sensitivity of our results to decarbonization pace, we otherwise rely on median socioeconomic, energy, and geophysical projections, which in reality contain large uncertainties. Specifically, the sensitivity of transition emissions to high- or low-end projections of climate warming, SLR, renewable energy learning rates, and population and GDP growth should be explored further.

Despite these limitations, we conclude that the magnitude of CO_2 emissions embedded in the broader climate transition are of geophysical and policy relevance, equaling an important

fraction of the remaining carbon budget. In addition, transition emissions can be greatly reduced under faster-paced decarbonization, lending new urgency to policy progress on rapid renewable energy deployment. We also conclude that regionally disparate contributions to transition emissions threaten to perpetuate present and historical climate inequities into the transition era, unless wealthy actors commit to equitable policies. Most fundamentally, our results point to underappreciated synergies and trade-offs between mitigation goals and embedded transition emissions, which must be better understood and integrated into climate policy for a just and effective transition.

4) Methods:

Overall framework and scope

To estimate the probable emissions from mitigation and adaptation through the transition to a stable climate, we must first establish a limited scope of sectoral interventions. It is impossible to exhaustively account for the diverse changes required to mitigate and adapt to climate change globally, which involve a vast array of changes at household, institutional, national, and international scales. We instead focus on interventions that satisfy three criteria which we treat as proxies for the global gross energetic and material magnitude of the interventions, as well as the likelihood of them being implemented.

First, we constrain our scope to interventions responding to global-scale changes (e.g., adaptation to SLR, deployment of solar and wind power) rather than ones that are limited to specific environments (e.g., adaptation to or reducing emissions from melting permafrost). Second, we focus on plausibly energy- and material-intensive options for adaptation (for instance, constructing new coastal protections as opposed to breeding heat-tolerant crop varieties) and

mitigation (for instance, building wind turbines as opposed to reducing deforestation). Finally, we focus on adaptation to aspects of climate change projected with high confidence (e.g., sea levels and mean temperatures are very likely to rise and not fall), rather than aspects with greater directional uncertainty and higher regional and temporal variability (e.g., hydrological drought may increase or decrease in many places). We assert that high confidence in the direction of such changes translates to high confidence in the eventuality of the interventions.

Following these criteria, four sectoral interventions are likely to be among the largest sources of emissions, enabling a simple but conservative estimate of the rough magnitude. These are 1) energy decarbonization, or the construction of renewable electricity generating capacity and associated infrastructure, 2) coastal protection, 3) coastal retreat, and 4) adaptive enhancement of space cooling. This list is a small sample of the likely total mitigation and adaptation effort, and in this sense our estimated emissions from mitigation and adaptation are by definition a lower bound. Furthermore, many of the key economic, energy, and policy interactions among mitigation and adaptation interventions remain frontiers of research with dramatic uncertainties (Hauer et al., 2020; Horton et al., 2021; Lesnikowski et al., 2017; Viguié et al., 2021). We therefore conceptually simplify our analysis by neglecting some potential interactions among these interventions, instead treating them as dynamically independent (e.g., we neglect future coastal retreat as a potential barrier or boon to deployment of offshore wind). We further limit our focus to CO_2 as the main anthropogenic GHG.

For each of the four interventions (subscripts i), we conceptualize emissions ($E_{i,t}$) as the amount of each activity ($N_{i,t}$) times its emissions intensity ($I_{i,t}$), both of which evolve over the years of the transition (subscript t). The cumulative total emissions from mitigation and adaptation (E_{M+A}) interventions through the transition is the sum over i and t:

$$E_{M+A} = \sum_{i,t} E_{i,t} = \sum_{i,t} N_{i,t} I_{i,t} \quad (1)$$

This simple governing equation decomposes the task of emissions estimation into two components: modeling adaptation and mitigation activities over time, and estimating their emissions intensities. Data limitations constrain the spatial scale of the equation to the global aggregate, precluding the examination of differences between countries ' mitigation and adaptation pathways and emissions intensities. The time dependence of the terms in equation 1 relates to the pace of energy decarbonization, as well as population and economic trends. We use a broadly consistent set of input GDP and population projections from the UN median scenario (United Nations 2019), Shared Socioeconomic Pathways (SSPs) (KC & Lutz, 2017), and other sources (Diaz, 2016; Levesque et al., 2018; Sgouridis et al., 2016). We examine the transition over the period 2020-2100.

The amount of each intervention over time is estimated using a suite of sectoral models, namely the Sustainable Energy Transition model (NETSET V2.0) (Sgouridis et al., 2016), the Coastal Impacts and Adaptation Model (CIAM V1) (Diaz, 2016), and the Energy Demand Generator (EDGE) (Levesque et al., 2018). To estimate emissions intensities of the interventions over time, we generally first estimate the energy intensity of the intervention based on literature, and then convert the energy to emissions depending on the energy mix evolution from the NETSET runs and the emissions intensities of fossil fuels from literature. For the case of coastal retreat and protection, we separately assess *process emissions* arising from chemical reactions in material production (i.e., CO_2 released by chemical reactions in concrete and steel production). The methods for the sectoral modeling and emissions accounting are discussed in the following sections. The complete methods are summarized in Figure S3.

Energy decarbonization pathways

We use the NETSET energy transition model to simulate the replacement of fossil fuels with renewables and the investment of energy into bringing the renewable capacity online (i.e. the 'seed 'energy for renewables) through 2100. As a net energy model, NETSET is suited to this task, explicitly simulating energy investments into energy via variation in energy return on energy invested (EROEI) across primary energy sources. Meanwhile, the main limitation of NETSET is incomplete representation of economic dynamics (e.g. capital markets, technological diffusion, and economy-energy feedbacks beyond EROEI dynamics). The model functions as a globally-aggregated back-casting model that simulates plausible transition pathways satisfying the preconditions that 1) geophysical carbon budgets for assumed warming targets are not exceeded (see section *Emissions accounting*), and 2) a minimum *net* primary power per person of 2000W is met by the global energy system (*net* meaning excluding seed energy). Other important model dynamics included assumed scale-limitations for hydroelectricity, nuclear, geothermal, and biomass, as well as assumptions about future learning rates in deployment of solar and wind. The energetic contribution of fossil fuels through the transition is determined based on Hubbert curves with assumed peak extraction in 2020. We use a uniform peak extraction year across scenarios to isolate the influence of transition pace, rather than time of onset. Finally, the deployment of scalable renewables (i.e., solar photovoltaic, compact solar power, geothermal, and wind) dynamically responds to the time evolution of fossil fuels and scale-limited renewable capacity, subject to the per-capita energetic and carbon budget preconditions. Energy investment into renewables is allocated across energy sources based on the gross energy mix and EROEI of different energy sources, and we track the fraction of renewable energy reinvestment as a key determinant of seed-energy emissions. NETSET is open-source (https://set.csaladen.es/) and further model details can be found in Sgouridis et al. (2016).

We focus first on a gradual decarbonization pathway assuming a carbon budget of 1,150GtCO$_2$ from 2020 onwards, corresponding to a warming cap of 2°C assuming a 67th percentile transient climate response to cumulative emissions (TCRE) (Canadell et al., 2021). This scenario is broadly consistent with the RCP2.6 emissions scenario in terms of cumulative total emissions and ensuing climate-model projected warming (Meinshausen et al., 2011). We then examine the sensitivity of embedded transition emissions to delayed and rapid decarbonization pathways. For the delayed case, we stipulate a carbon budget of 2,150GtCO$_2$, linked to a warming of 2.7°C in 2100 (67th percentile TCRE) and broadly consistent with RCP4.5 emissions scenario in terms of cumulative total emissions and warming. This scenario is in line with the current global aggregate of actual climate policies, and thus reflects a likely pathway in the absence of strong climate policy ambition. For the rapid case, we stipulate a carbon budget of 400GtCO$_2$ linked to a warming cap of 1.5°C, consistent the 2015 Paris agreement. Together, these scenarios reflect the plausible range of decarbonization pace, including highly ambitious (rapid), moderately ambitious (gradual), and business-as-usual (delayed) pathways.

We simulate these three energy decarbonization pathways using NETSET (Sgouridis et al., 2016), and use these simulations as the energy system backbone for the remaining modeling in this study. First, the simulations enable the estimation of emissions embedded in the transition by providing time series of coal, oil, and natural gas energy investment into renewables (N_{SET}). Second, they enable the estimation of the emissions intensity of global energy use for the three adaptation interventions via time series of energy mix.

Coastal retreat and protection

CIAM is a global cost-optimization model that assesses coastal impacts and least-cost optimal adaptation decisions for ~12,000 individual coastal segments (Diaz 2016). The model code is

open-source and publicly available from https://github.com/delavane/CIAM. The decision set includes construction of coastal protection (conceived of here as a sea dike), coastal retreat (conceived of reconstruction of coastal settlements further inland), or no adaptation (with associated flood damage and loss of coastal land). The model assimilates diverse socioeconomic and geophysical data, notably from the DIVA coastline dataset (Vafeidis et al., 2008), to estimate protection, retreat, and flood damage costs as well as the value of inundated coastal land (land value) and wetlands (value of wetland ecosystem services). For each segment, the optimal decision is that which minimizes the sum of these costs under projected SLR for an assumed planning period. Beyond the optimal decision category, the model also provides optimal quantities for retreat (the retreat perimeter defined as an elevation above sea level, from which retreat population can be derived) and protection (the optimal dike height).

CIAM's main strength is its integration of top-down geophysical drivers of risk with bottom-up socioeconomic variables (e.g., GDP, land value, and population, broadly consistent with SSP2) that are essential to understanding probabilities of coastal protection and retreat. Its main limitation is that a relatively circumscribed set of socioeconomic variables are considered, excluding hard-to-quantify ones reflecting local political or cultural barriers to or enablers of retreat and protection (Hauer et al., 2020; Horton et al., 2021; Mach & Siders, 2021). These factors could lead to outcomes that deviate from cost-optimality. Further, cost "optimal" decisions under this framework are not necessarily equitable or socially preferred due to a dominant influence of GDP as a proxy of capital density on model adaptation decisions. As a result, CIAM projects large parts of the Global South with high population but low capital density to remain unprotected through 2100.

Our CIAM implementation stipulates an adaptation planning horizon of 2050-2100 in which decision-making accounts for sea level in 2050 and projected SLR to 2100 (i.e., we assume planners use a unified set of sea level projections). This planning horizon allows the three decarbonization pathways to have differential influences on adaptation decisions, as SLR projections do strongly depend on emissions scenarios prior to 2050. The optimization is run for 10-year time steps over this 50-year planning time horizons over. In each time step, the historical flood statistics for each coastal segment are incremented by locally-downscaled SLR projections, modifying the cost function and thus the optimal decision over time. We then aggregate the incremental adaptations over the planning horizon into a single projected adaptation decision responding to projected SLR for the period. Because CIAM does not simulated when within the 50-year planning horizon adaptations will be built, we assume that all coastal adaptations occur in 2060. This provides a reasonable 10 years after the start of the planning period for adaptations to roll out, and the time midpoint of the transition as defined by our analysis period.

Projected mean SLR is based on (Kopp et al., 2014), which downscales global SLR projections to the local scale. This dataset increments circa-2000 historical sea level distributions, estimated from global tide gauge data, by projected thermal expansion, land-based ice melt, land water storage, and other terms, driven by RCP2.6 for gradual decarbonization and RCP4.5 for the delayed case. High-resolution downscaled SLR projections are still under development for the 1.5°C rapid pathway, so in the interim, we estimate them by decrementing those for RCP2.6 by the global mean difference in sea level rise between 2.0°C and 1.5°C (Fox-Kemper et al., 2021).

A central method in CIAM for the present study involves accounting for extreme sea levels, which determine retreat perimeter and protection height via their influence on flood damage costs and subsequent optimization. The DIVA dataset reports estimated 1-in-1, -10, -100, and -1000

year storm surge heights, which are used in CIAM along with SLR projections to estimate expected values of the flood damage in the cost optimization. Thus, cost-optimal retreat perimeters and protection heights are ultimately based on these underlying surge height levels. To account for initial adaptation in the absence of comprehensive global data on coastal protective infrastructure, CIAM's default assumption is that global coastlines are initially protected to the 1-in-1 year (i.e. mean annual maximum) storm surge height (S_1) at the beginning of the planning period. Here, we modify this assumption to better reflect widespread under-protection of global coastlines (McMichael et al., 2020), asserting instead that all coastal segments are initially protected to one-half of the 1-in-1 year storm surge.

In the absence of life-cycle analysis (LCA) literature for coastal protection infrastructure, we developed a simple geometric model of a generic dike based on technical literature (Jonkman et al., 2013; Vietnam Ministry of Agriculture and Rural Development, 2011) to estimate the volume of sea dike materials as a function of optimal protection height (H_{opt}) and coastal segment length (Appendix C Fig. 4). To convert the optimal protection height to sea dike build height, we increment the optimal protection height by the climatological maximum wave height from DIVA to incorporate a realistic wave run-up height (W_C) into the dike design. Thus, the full protection height including initial adaptation is given by:

$$H = H_{opt} + \frac{1}{2}S_1 + W_C \tag{2}$$

We then model the dike as a trapezoid in cross section with berm width b of 5m, slopes m_1 and m_2 of 1:4 on the seaward side and 1:3 on the landward side, and a reinforced concrete foundation with thickness of $F = ¼H$. We assume the dike to be filled with local soil and rock (and thus neglect transport emissions) and encased in a revetement of medium-strength steel reinforced concrete

with thickness T equal to 1m. We treat the sum over coastal segments s of the volume of reinforced concrete in the dikes (N_{CP}), which is quadratic in build height, as the main driver of coastal protection emissions. This volume is the product of the cross-sectional area of the concrete revetement and the coastline segment length (L_s):

$$N_{CP} = \sum_s L_s \left\{ \frac{1}{4}(m_1 + m_2 + b)H^2 + (m_1 + m_2)HT - \frac{1}{2}(m_1 + m_2)T^2 + (m_1 + m_2)T \right\} \quad (3)$$

For the case of coastal retreat, we treat the number of households retreated (N_{CR}) as the driver of emissions, assuming an equivalent number of new dwellings will be constructed to accommodate them. Retreat population is estimated by first converting the retreat perimeter height to retreat area using elevation-area functions in DIVA and then multiplying the retreat area by population density (also from DIVA). Due to a lack of supporting literature, we neglect emissions likely to result from energy embedded in the removal of abandoned housing and infrastructure.

Space cooling

To estimate future adaptive energy demand for space cooling, we use the EDGE building energy modeling framework (Levesque et al., 2018). EDGE expands the SSPs (Dellink et al., 2017; KC & Lutz, 2017; O'Neill et al., 2017) to project consistent changes in building floor space demand (positively related to GDP and total population, negatively to population density) and building efficiency (assumed to increase with technological improvement). In EDGE, per capita cooling energy demand responds to climate warming in two ways. As hot days increase with climate warming, a larger proportion of the global population acquires cooling equipment, and each cooling appliance is used more intensively. Simulated cooling demand is also influenced by population growth, efficiency improvements in cooling appliances and building envelopes, and income per capita which augments floor space per capita and the relative affordability of air conditioning. Additional detail on the EDGE framework can be found in (Levesque et al., 2018).

Future cooling degree day (CDDs) are projected based on CMIP5 climate model runs under the RCPs emissions scenarios. In this setup, CDD's are computed as the sum of daily degrees above an assumed daily mean temperature cooling threshold of 21°C. Gridded temperature projections from the climate models are weighted by population density in their aggregation to the national scale. In this study, we use final energy demand projections from EDGE run under the 'middle-of-the-road 'SSP2 and with CDD projections from RCP2.6 for gradual decarbonization and RCP4.5 for the delayed scenario. For the rapid pathway, we rescale the RCP2.6 CDD projections based on the global difference in mean warming between the 2.0°C and 1.5°C pathways, as explicit CDD projections for this scenario are still under development.

Population, income, and insulation dynamics are assumed to be the same for all decarbonization pathways to isolate the impact of climate change from socioeconomic trends. We further isolate the climate-adaptive component of projected energy demand for each pathway by subtracting energy demand projections under a constant historical climatology from the runs with warming. This assumes that expanding cooling due to socioeconomic trends (e.g., first-time acquisition of air conditioners newly enabled by rising incomes) is not itself climate-adaptive. We convert final to primary cooling energy demand by first estimating the global primary-to-final energy conversion efficiency based on global mean power station conversion efficiencies from the IEA, averaged over the 5 most recent years with available data (2014-2018) (IEA 2021). We update this primary-to-final ratio through the energy decarbonization pathway based on the energy mix evolution in NETSET, assuming a primary-to-final energy ratio of 1 for renewables. We finally report climate-adaptive space cooling as primary energy demand, which we treat as the relevant input to the emissions accounting.

Emissions accounting

The sectoral modeling approaches enable an estimation of the adaptation amount ($N_{i,t}$) terms in equation 1. The remaining ingredient is to estimate the emissions intensities of the interventions ($I_{i,t}$), which we accomplish by combining with LCA literature and databases with NETSET energy mix projections (Table S1). We limit the scope of the study to CO_2. First, we estimate the global mean emissions intensity of primary energy (I_F) for the three fossil fuel classes in NETSET (coal, oil, and gas) which are then used to compute emissions from space cooling and coastal adaptation energy demand. The emissions intensity of energy use from coal, oil, and natural gas is estimated as the 2018-2050 average of projected global energy-related emissions by fuel class divided by the total energy use by fuel class based on data from the US Energy Information Administration International (EIA) Energy Outlook 2019 (Table S1). Note that this approach does not assimilate EIA energy mix projections, but only emissions intensity projections. We neglect emissions from the extraction and processing of nuclear fuels, and assume zero emissions from other non-fossil fuel energy carriers such as fugitive emissions from geothermal and hydroelectric and non-energy related build emissions for solar and wind (e.g., process emissions from steel).

To estimate the cumulative emissions embedded in the decarbonization pathways, we first estimate the global emissions intensity of overall primary energy use over time ($I_{E,t}$ in units of mass of CO_2 per unit primary energy use) by weighting the emissions intensities per fuel *f* by their share in the energy mix as projected in NETSET ($x_{f,t}$). We then simply multiply projected energy investment into energy (N_{SET}) by $I_{E,t,}$ the global emissions intensity of energy, and sum across the transition period:

$$E_{SET} = \sum_t N_{SET,t} I_{E,t} = \sum_t N_{SET,t} \sum_f x_{f,t} I_f \qquad (3)$$

We follow a similar equation to convert adaptive cooling energy demand to emissions. While space cooling is linked to certain potent non-energy GHG emissions such as hydrofluorocarbons, we

limit the scope of our assessment to CO_2. We also do not consider avoided emissions from reduced space heating, as we limit our scope to adaptations with positive emissions.

For construction of sea dikes, we use emissions factors and embedded energy estimates for construction materials from (Hammond & Jones, 2008). Assuming a density of concrete of 2,400kg/m^3 and 150kg of reinforcing steel per m^3 (Kellenberger et al., 2007), we calculate a volumetric emissions factor to convert global total volume of sea dike revetement ($N_{CP,}$ equation 3) to emissions. We neglect emissions from rock and soil transport for the dike interior as well as from site preparation. For coastal retreat, we assume resettlement will be directed towards medium density urban developments and base our emissions factor on recent LCA estimates of CO_2 emissions and embedded energy (E) arising from these constructions per unit floor area (Kayaçetin & Tanyer, 2020; Monahan & Powell, 2011). These estimates include some necessary infrastructure beyond dwellings themselves, such as roads, but are not comprehensive (e.g., they do not include water systems). To convert between retreat population and retreat dwellings, we assume a mean household size of five people (Pew Research Center, 2019), and a dwelling ground area of 225m^2 as in EDGE (Levesque et al., 2018).

For dikes and resettlement, the emissions intensity incorporates both fossil fuel energy use and non-energy process emissions from materials such as cement and steel production. To account for decarbonization of energy in the future, we update the emissions factors for dikes and resettlement at time t by rescaling emissions due to embedded energy (E) by the difference in emissions intensity of energy (I_E) between time t and prior to the transition (t_0):

$$I_{i,t} = I_{i,t_0} + E(I_{E,t} - I_{E,t_0}) \qquad (4)$$

This approach assumes that the remaining non-rescaled portion of the emissions (i.e., process emissions) remains constant into the future. The precision of the timing of adaptation decisions

from CIAM is limited to 50-year planning horizons, so we simply assume that all coastal retreat and protection occurs at the midpoint of the transition in 2060. We neglect emissions from the operation and maintenance of relocated housing and coastal protection.

The final aspect of emissions accounting is to contextualize the emissions embedded in the transition relative to relevant benchmarks. To understand the magnitude of emissions on an Earth system scale, we express transition emissions as a fraction of the remaining carbon budget for the respective pathways (1,150$GtCO_2$ for gradual, 2,150$GtCO_2$ for delayed, and 400$GtCO_2$ for rapid) (Canadell et al., 2021).

Appendix C

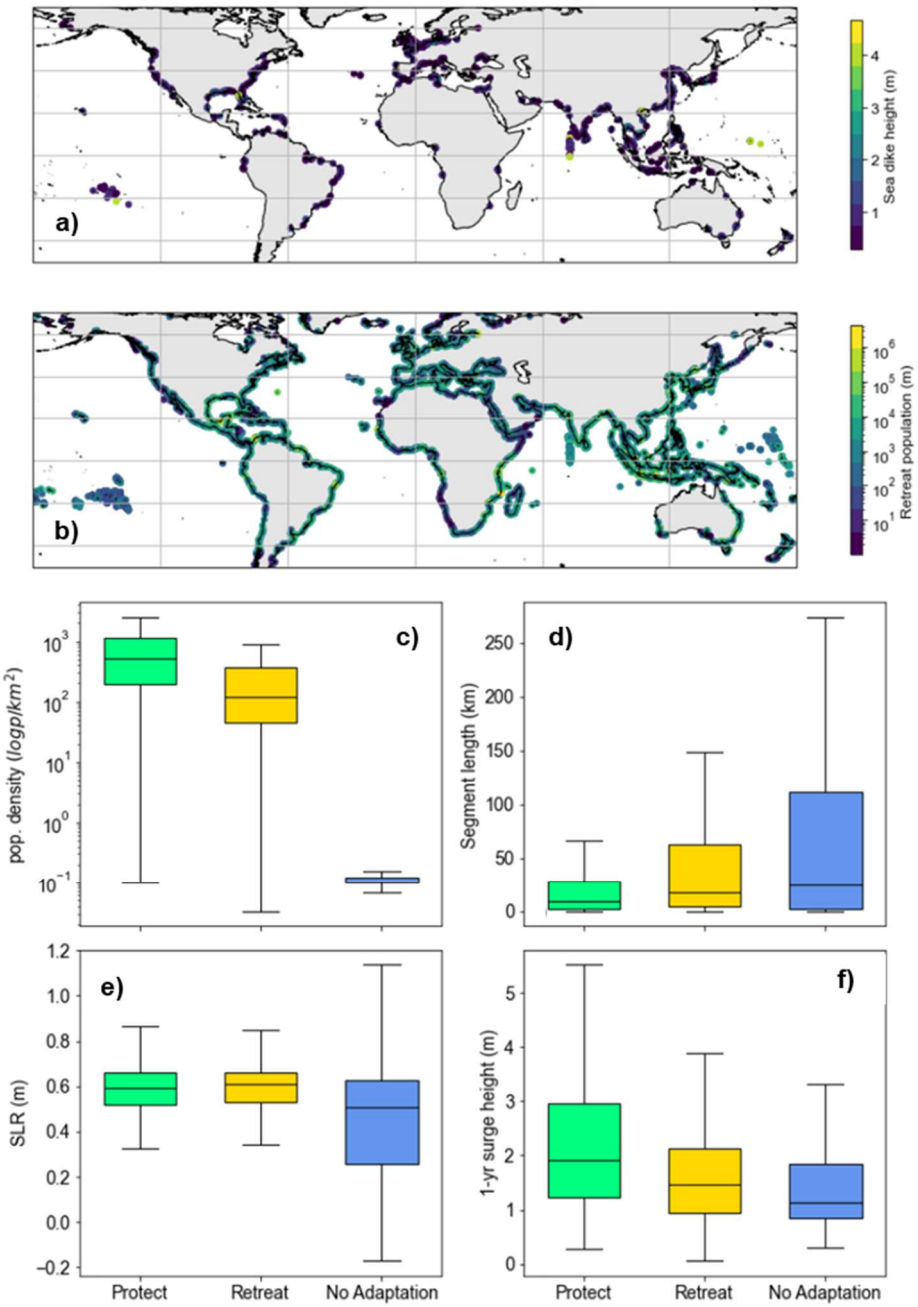

Appendix C Figure 1: Geographic distribution of coastal adaptation. a) Optimal coastal protection height for individual coastline segments for the 2050-2100 planning period under RCP 2.6 (rapid decarbonization) as projected using CIAM. b) Same as a) but showing optimal retreat population. c-f) Boxplots of geographic determinants of coastal adaptation across adaptation decisions, c) population density (logarithmic), d) length of coastline segments, e) projected SLR in 2100, and f) historical once-per-year maximum storm surge height. Boxplot depict distributions of determinant variable values across coastline segments within each adaptation decisions. Boxplot centers depict medians, boxes the 25th and 75th percentiles, and whiskers maxima and minima excluding outliers.

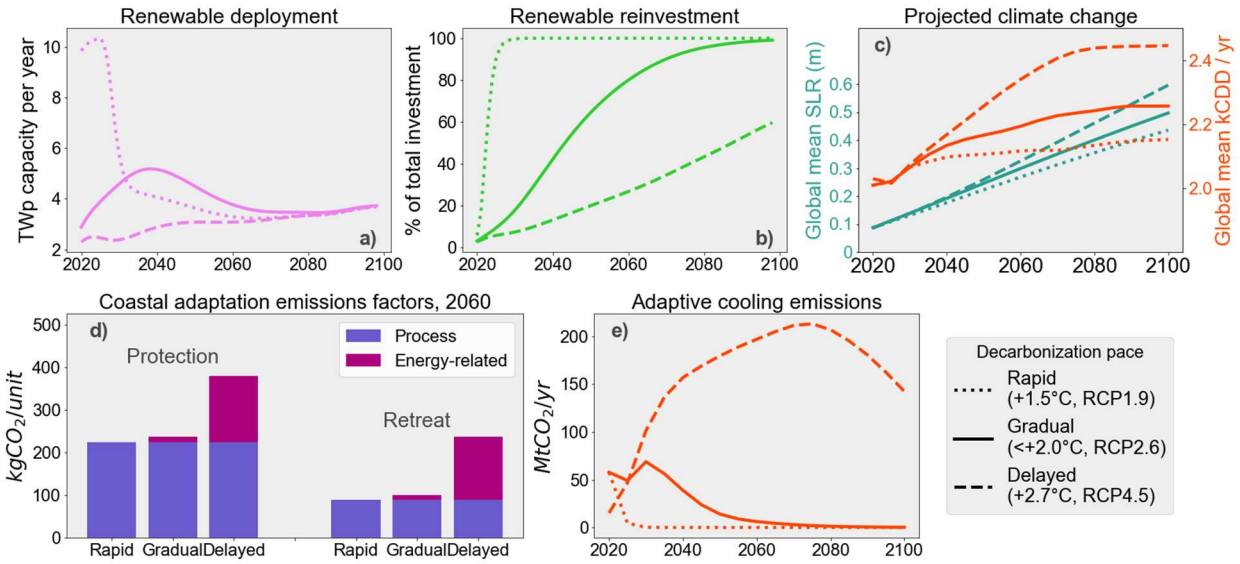

Appendix C Figure 2: Drivers of increased emissions under gradual decarbonization compared to the rapid scenario. a) Simulated renewable energy deployment rate (TWp capacity per year, pink) and reinvestment rates (percent of total energy invested into renewables, green) under gradual (solid lines) and rapid (dotted lines) decarbonization. b) Projected cumulative global mean SLR (m, blue) and warming (kCDD per year, red) under RCP4.5 (for gradual decarbonization) and RCP2.6 (for rapid). c) Adaptive cooling emissions ($MtCO_2$ per year) under gradual (solid lines) and rapid (dotted lines) decarbonization, as well as under RCP4.5 warming but using the energy mix of rapid decarbonization (dot-dash line). d) Emissions intensities of coastal protection ($kgCO_2$ per m^3 dike) and retreat ($kgCO_2$ per m^2 replacement housing) under rapid and gradual decarbonization. Emissions intensities are separated into process emissions (due to chemical reactions in material production, purple-blue bars), assumed constant through the transition, and energy-related emissions (simulated to decline with energy decarbonization, dark pink bars).

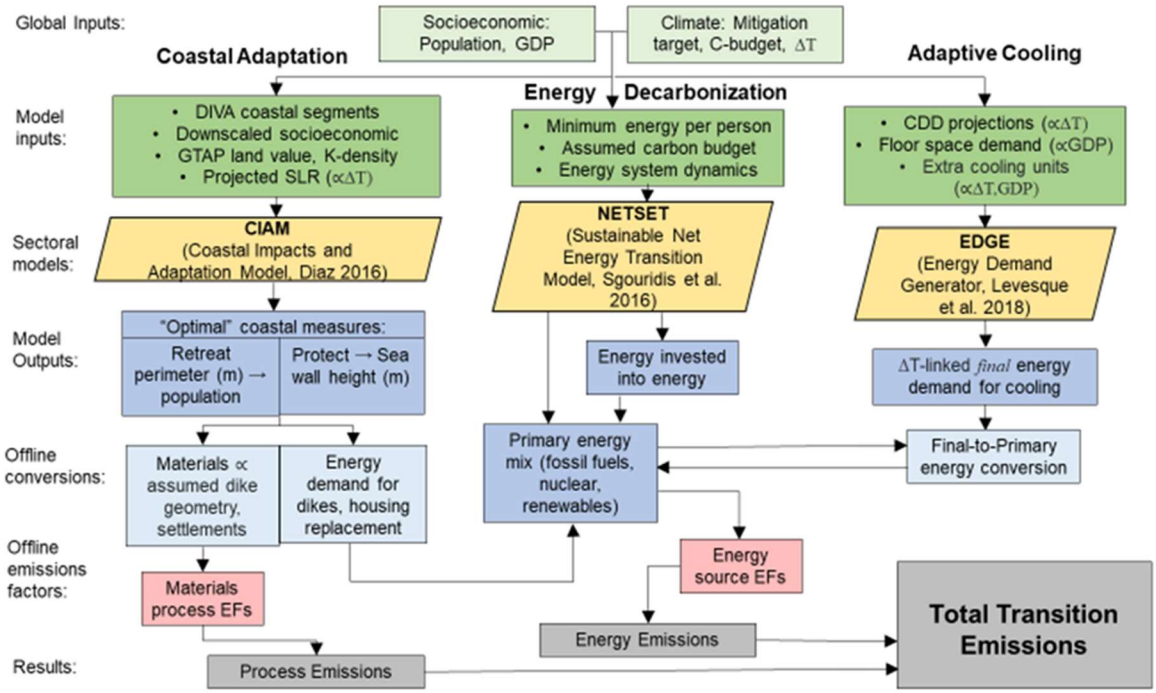

Appendix C Figure 3: Flowchart of methods used to estimate mitigation and adaptation emissions embedded in the transition to a stable climate. Global data inputs appear in light green at top, with model-specific data inputs, assumptions, and key dependencies shown in dark green below. Sectoral models with references appear in yellow. Direct sectoral model outputs appear in dark blue, while offline conversions of model outputs to energy or material terms appear in light blue. Finally, energy and materials demands are converted to emissions (shown in grey) based on energy and material process emissions factors (EFs), shown in pink.

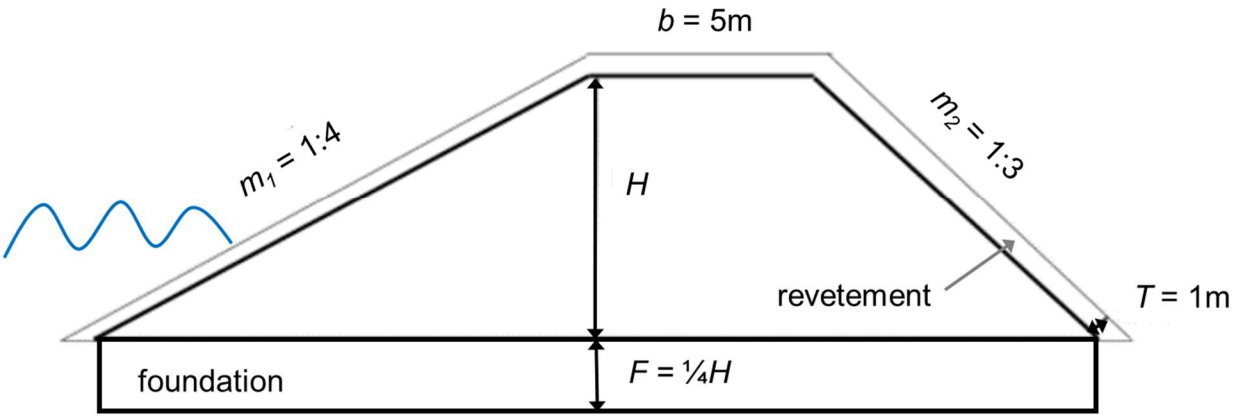

Appendix C Figure 4: Idealized dike model geometry. Cross-section schematic of idealized dike with annotated key parameters of the geometry (which appear in equation 3). Dimensions are not to scale. The dike height H includes optimal protection height (H_{opt}) incremented by initial under-adaptation (S_1) and wave run-up heights (W_c) as per equation 2. The concrete revetement and foundation are taken as drivers of emissions related to coastal protection, while the interior of the dike is assumed to be filled with local rock and soil with negligible associated emissions. The coastline segment length (L_s) runs perpendicular to the plane of the cross section (i.e., into the page).

Appendix C Table 1: Factor values used for emissions accounting and their sources.

Sector	Item	Factor	Value	Source
Primary energy	Oil	Emissions factor	60GtCO2/TJ	EIA IEO 2019
	Coal	Emissions factor	90GtCO2/TJ	EIA IEO 2019
	Gas	Emissions factor	50GtCO2/TJ	EIA IEO 2019
Coastal protection	Concrete	Density	2,400kg/m3	
		Emissions factor	0.035kgC/kg	Hammond et al. 2008
		Embodied energy	0.95MJ/kg	Hammond et al. 2008
	Steel general rebar	Mass per m3 concrete	150kg/m3	Kellenberger et al. 2007
		Emissions factor	0.482kgC/kg	Hammond et al. 2008
		Embodied energy	24.4MJ/kg	Hammond et al. 2008
Coastal retreat	Household size	Global mean	5 people	Pew 2019
	Floor area	Global mean	150m2	
	Housing	Emissions factor	400kgCO2/m2	Monahan et al. 2011
		Embodied energy	5.7GJ/m2	Monahan et al. 2011

Conclusion

In Chapter 1, I show that while hourly rainfall intensification under warming may benefit some important crop yields somewhat, it will not compensate for the larger impacts of warming itself. Chapter 2 demonstrates a signature of temperature-moisture couplings in the global pattern of maize and soy sensitivity to heat, and shows how future strengthening of the couplings will exacerbate the impact of warming on average. In light of this research (and a wide body of other research and overwhelming obviousness), effective mitigation is essential. In Chapter 3, I show that the emissions embedded in the broader climate transition are substantial enough to merit deeper consideration in global climate policy and, under current policies, seriously imperil the 1.5°C maximum warming goal.

The results of Chapter 3 should provide additional rationale for prioritizing rapid decarbonization. However, rationale has been abundant over my entire lifespan, and has done little to actually displace fossil fuels. Moreover, even if the publication of Chapter 3 succeeds in conveying this political significance, the deployment of renewable energy will most likely take longer than ideal, given myriad technical and geopolitical complications (F. C. Moore et al., 2022). Crops and food systems will therefore need to be adapted if they are to continue underpinning human wellbeing and survival in the 21st Century. And towards this necessity, I focus my conclusions on the implications of Chapters 1 and 2 for crop adaptation.

Implications of Chapters 1 and 2 for crop adaptation

In the introduction, I situated these chapters within the concept of compound extremes, a popular topic in contemporary climate science, impacts, and adaptation literature. And while the questions addressed in these chapters are highly specific instances of this general concept, I think the general

concept neatly capture the core challenge defining this period in agricultural history. By this, I mean that crop production faces a long-term concurrent rise in multiple climate (and other stressors), which may weaken some historically-effective yield-boosting tactics.

Future climate impacts on crops will likely be largely determined by increases in three extremes: heat, drought, and heavy short-duration precipitation. For reasons outlined above, these changes will occur simultaneously, and interactively influence future yields. Chapter 1 uncovers a modest potential yield gain from stronger hourly rainfall under climate change, which only slightly offsets a larger yield loss from warming. Chapter 2 shows that the larger yield loss from warming may be exacerbated by 21st-Century intensification of the couplings that cause heat and drought to co-occur. Although many questions persist, these considerations of compound extremes taken together result in a more pessimistic updated expectation for future yields, mainly as a result of increasing compound heat-drought risk.

Facing extreme heat *or* drought, yields have traditionally been ensured through two approaches: crop breeding and management. For extreme heat, crop breeding typically involves selecting for favorable metabolic and stomatal temperature sensitivities. For drought, crop breeding largely targets water-use efficiency and drought tolerance. Irrigation and stress avoidance have for millennia been used as important management strategies for both. These dominant traditional targets to breed crops for drought *or* heat may become limited or even conflict under concurrent heat *and* drought.

A key breeding target for drought or heat is stomatal density (the number of leaf pores per unit area) and stomatal regulation (the physiology of how these stomata are opened and closed to control the trade off between carbon gain and water loss) (Buckley, 2019; C. E. Moore et al., 2021). Together, these parameters control crop transpiration, which lowers plant water status and depletes

soil moisture, but cools leaf temperatures through latent heating. One way of breeding for drought targets the former effects of transpiration: increase stomatal regulation during drought to maintain plant water status and soil moisture. One way of breeding for heat targets the latter: decrease stomatal regulation so crops continue to transpire at high temperatures to locally buffer the heat extreme. The goals of these two approaches are at odds for combined heat and drought, in which tightened stomatal regulation limits the crops 'thermoregulation capacity, but lax stomatal regulation further depletes soil moisture raises crops 'risks of critical wilting (cavitation).

These dynamics, combined with the results of this thesis, suggest that the stomatal avenue for crop breeding is of limited promise for adaptation to future climates. The relevance of this antagonism could be curtailed with expanding irrigation, which is widely cited as a promising crop adaptation (Carter et al., 2016; J. Jägermeyr et al., 2016). In the context of compound extremes, irrigation has a double benefit to crops in a warming climate: it provides crops with sufficient soil moisture while cooling the local land surface (Thiery et al., 2020). However, the results of this thesis point to new limitations of irrigation in the context of compound extremes. With a future rise in concurrent drought and heat, surface water sources may be especially limited at precisely the moments they are most needed. Further, irrigation on hot and dry days may boost humidity and heat stress to agricultural workers, complicating adaptive management. Finally, extractions for irrigation from deep groundwater sources, which are less sensitive to climate variability, are highly unsustainable in many regions dependent on them (Rosa, Chiarelli, Rulli, et al., 2020).

The results of Chapter 1 point to another promising avenue for crop adaptation to climate change. The proposed (and yet to be tested) mechanism for maximum yield benefits from heavy hourly-intensity rainfall relates to its relative plant availability (i.e., higher correlation with soil moisture) compared to light (high evaporative loss) and extreme (high runoff loss) intensities. Crop

morphology and canopy structure – a traditional breeding target with regard to light penetration (C. E. Moore et al., 2021) – may be explored as a variable than can help optimize interception dynamics given these results. Further, improvements to soil organic carbon content and texture may increase the range of rainfall intensities that can be absorbed by soils (along with myriad other crop, mitigation, and environmental co-benefits).

Other traditional breeding goals, like increasing enzymatic optimal temperatures and resistance to cavitation, will likely remain promising regardless of concurrent extremes. Further, despite the limitations across much of global croplands discussed above, irrigation is promising and should be equitably financed in the Tropics, where yield gaps are presently high, but future water availability and temperature-moisture couplings are more favorable to agriculture (Rosa, Chiarelli, Sangiorgio, et al., 2020). Regardless, the broadest conclusion of Chapters 1 and 2 is that crop adaptation will increasingly need to consider multivariate targets and complex biophysical interactions in the context of compound extremes, seeking co-benefits and avoiding antagonisms from the cell to field scale (Ramirez-Villegas et al., 2020).

A final thought on whether this is useful

To conclude, it is worth considering a point raised early in the introduction, which is that crop production only partly determines food security, and to consider the usefulness of this research to the real-world problems at hand. Two considerations are well beyond the results of this thesis, but certainly worth noting.

First, the global food crisis is increasingly one of too-many-calories, not-enough-nutrients. Some of the main results of this thesis concern maize and soy, which largely provide cheap carbohydrates and oil, and otherwise are mostly destined for feed rather than food (Cassidy et al.,

2013). What is more deficient in global diets is fiber and micronutrients from fruits and vegetables, which are typically produced in intensive horticulture systems that differ importantly from field crops. Future yields and adaptation avenues for these systems, as well as 'alternative 'cereals like millet and sorghum (which are more nutritious *and* drought and heat tolerant than maize and soy), require more attention. In other words, if maize is globally the most vulnerable crop to climate change (Jägermeyr et al., 2021), perhaps it is worth considering the attendant possible health and nutrition opportunities, and whether food security would be better supported by replacing the caloric shortfall from maize with more nutritious alternatives (Challinor et al., 2016).

Second, it remains unclear to me whether such biogeoscientific research is useful to future food security goals. For instance, some leaders in climate science have called for increasing attention to how disciplinary skills can be best applied to support adaptation (Sobel, 2020). One hope for this thesis is to signal (and, to a small extent, contribute to) a greater integration among biogeosientists, plant physiologists, crop breeders, agronomists, and food system researchers to provide the research insights needed. Whether anyone with resources and authority listens to us is perhaps a separate question. But one place to start is to ask, and provide the soundest possible answers to, the right questions.

References

Ainsworth, E. A., & Long, S. P. (2021). 30 years of free-air carbon dioxide enrichment (FACE): What have we learned about future crop productivity and its potential for adaptation? *Global Change Biology*, *27*(1), 27–49. https://doi.org/10.1111/gcb.15375

Ali, H., Fowler, H. J., Lenderink, G., Lewis, E., & Pritchard, D. (2021). Consistent Large-Scale Response of Hourly Extreme Precipitation to Temperature Variation Over Land. *Geophysical Research Letters*, *48*(4). https://doi.org/10.1029/2020GL090317

Allan, R. P., Barlow, M., Byrne, M. P., Cherchi, A., Douville, H., Fowler, H. J., Gan, T. Y., Pendergrass, A. G., Rosenfeld, D., Swann, A. L. S., Wilcox, L. J., & Zolina, O. (2020). Advances in understanding large-scale responses of the water cycle to climate change. *Annals of the New York Academy of Sciences*, *1472*(1), 49–75. https://doi.org/10.1111/nyas.14337

Ashraf, M., & Habib-ur-Rehman. (1999). Interactive effects of nitrate and long-term waterlogging on growth, water relations, and gaseous exchange properties of maize (Zea mays L.). *Plant Science*, *144*(1), 35–43. https://doi.org/10.1016/S0168-9452(99)00055-2

Ault, T. R. (2020). On the essentials of drought in a changing climate. *Science*, *368*(6489), 256–260. https://doi.org/10.1126/SCIENCE.ABC4034

Bassu, S., Brisson, N., Durand, J. L., Boote, K., Lizaso, J., Jones, J. W., Rosenzweig, C., Ruane, A. C., Adam, M., Baron, C., Basso, B., Biernath, C., Boogaard, H., Conijn, S., Corbeels, M., Deryng, D., De Sanctis, G., Gayler, S., Grassini, P., … Waha, K. (2014). How do various maize crop models vary in their responses to climate change factors? *Global Change Biology*, *20*(7), 2301–2320. https://doi.org/10.1111/gcb.12520

Berg, A., Findell, K., Lintner, B., Giannini, A., Seneviratne, S. I., Van Den Hurk, B., Lorenz, R.,

Pitman, A., Hagemann, S., Meier, A., Cheruy, F., Ducharne, A., Malyshev, S., & Milly, P. C. D. (2016). Land-atmosphere feedbacks amplify aridity increase over land under global warming. *Nature Climate Change*, *6*(9), 869–874. https://doi.org/10.1038/nclimate3029

Berg, A., Lintner, B., Findell, K., & Giannini, A. (2017). Soil moisture influence on seasonality and large-scale circulation in simulations of the West African monsoon. *Journal of Climate*, *30*(7), 2295–2317. https://doi.org/10.1175/JCLI-D-15-0877.1

Berg, A., Lintner, B. R., Findell, K. L., Malyshev, S., Loikith, P. C., & Gentine, P. (2014). Impact of soil moisture-atmosphere interactions on surface temperature distribution. *Journal of Climate*, *27*(21), 7976–7993. https://doi.org/10.1175/JCLI-D-13-00591.1

Berg, A., Lintner, B. R., Findell, K., Seneviratne, S. I., Denhurk, B. Van, Ducharne, A., Chéruy, F., Hagemann, S., Lawrence, D. M., Malyshev, S., Meier, A., & Gentine, P. (2015). Interannual coupling between summertime surface temperature and precipitation over land: Processes and implications for climate change. *Journal of Climate*, *28*(3), 1308–1328. https://doi.org/10.1175/JCLI-D-14-00324.1

Berg, P., Moseley, C., & Haerter, J. O. (2013). Strong increase in convective precipitation in response to higher temperatures. *Nature Geoscience*, *6*(3), 181–185. https://doi.org/10.1038/ngeo1731

Berrang-Ford, L., Siders, A. R., Lesnikowski, A., Fischer, A. P., Callaghan, M. W., Haddaway, N. R., Mach, K. J., Araos, M., Shah, M. A. R., Wannewitz, M., Doshi, D., Leiter, T., Matavel, C., Musah-Surugu, J. I., Wong-Parodi, G., Antwi-Agyei, P., Ajibade, I., Chauhan, N., Kakenmaster, W., … Abu, T. Z. (2021). A systematic global stocktake of evidence on human adaptation to climate change. *Nature Climate Change*, *11*(11), 989–1000. https://doi.org/10.1038/s41558-021-01170-y

Buckley, T. N. (2019). How do stomata respond to water status? *New Phytologist*, *224*(1), 21–36. https://doi.org/10.1111/nph.15899

Butler, E. E., & Huybers, P. (2013). Adaptation of US maize to temperature variations. *Nature Climate Change*, *3*(1), 68–72. https://doi.org/10.1038/nclimate1585

Byrne, M. P. (2021). Amplified warming of extreme temperatures over tropical land. *Nature Geoscience*, *14*(11), 837–841. https://doi.org/10.1038/s41561-021-00828-8

Canadell, J. G., Monteiro, P. M. S., Costa, M. H., L. Cotrim da Cunha, P. M. C., Eliseev, A. V., Henson, S., Ishii, M., Jaccard, S., Koven, C., Lohila, A., Patra, P. K., Piao, S., Rogelj, J., Syampungani, S., Zaehle, S., & Zickfeld, K. (2021). Global carbon and other biogeochemical cycles and feedbacks. In P. Masson-Delmotte, V., A. P. Zhai, S. L. Connors, C. Péan, S. Berger, N. Caud, Y. Chen, L. Goldfarb, M. I. Gomis, M. Huang, K. Leitzell, E. Lonnoy, J. B. R. Matthews, T. K. Maycock, T. Waterfield, O. Yelekçi, R. Yu, & B. Zhou (Eds.), *Climate Change 2021: The Physical Science Basis. Contribution of Working Group I to the Sixth Assessment Report of the Intergovernmental Panel on Climate Change*. Cambridge University Press.

Carter, E. K., Melkonian, J., Riha, S. J., & Shaw, S. B. (2016). *Separating heat stress from moisture stress : analyzing yield response to high temperature in irrigated maize Separating heat stress from moisture stress : analyzing yield response to high temperature in irrigated maize*.

Cassidy, E. S., West, P. C., Gerber, J. S., & Foley, J. A. (2013). Redefining agricultural yields: From tonnes to people nourished per hectare. *Environmental Research Letters*, *8*(3). https://doi.org/10.1088/1748-9326/8/3/034015

Center, P. R. (2019). *Religion and Living Arrangements Around the World*.

http://www.ghbook.ir/index.php?name= فرهنگ و رسانه های نوین&option=com_dbook&task=readonline&book_id=13650&page=73&chkhashk=ED9C9491B4&Itemid=218&lang=fa&tmpl=component%0Ahttp://www.albayan.ae%0Ahttps://scholar.google.co.id/scholar?hl=en&q=APLIKASI+PENGENA

Challinor, A. J., Koehler, A.-K., Ramirez-Villegas, J., Whitfield, S., & Das, B. (2016). Current warming will reduce yields unless maize breeding and seed systems adapt immediately. *Nature Climate Change*, *6*(10), 954–958.

Chou, C., Chen, C. A., Tan, P. H., & Chen, K. T. (2012). Mechanisms for global warming impacts on precipitation frequency and intensity. *Journal of Climate*, *25*(9), 3291–3306. https://doi.org/10.1175/JCLI-D-11-00239.1

Choudhury, F. K., Rivero, R. M., Blumwald, E., & Mittler, R. (2017). Reactive oxygen species, abiotic stress and stress combination. *Plant Journal*, *90*(5), 856–867. https://doi.org/10.1111/tpj.13299

Chu, J., Yan, S. W., & Li, W. (2012). Innovative methods for dike construction - An overview. *Geotextiles and Geomembranes*, *30*, 35–42. https://doi.org/10.1016/j.geotexmem.2011.01.008

Climate Action Tracker. (2021). *Climate Action Tracker Emissions Gap*. climateactiontracker.org%0A

Coffel, E. D., Keith, B., Lesk, C., Horton, R. M., Bower, E., Lee, J., & Mankin, J. S. (2019). Future Hot and Dry Years Worsen Nile Basin Water Scarcity Despite Projected Precipitation Increases. *Earth s Future*, *7*(8), 967–977. https://doi.org/10.1029/2019EF001247

Cohen, I., Zandalinas, S. I., Huck, C., Fritschi, F. B., & Mittler, R. (2021). Meta-analysis of

drought and heat stress combination impact on crop yield and yield components. *Physiologia Plantarum*, *171*(1), 66–76. https://doi.org/10.1111/ppl.13203

Crafts-Brandner, S. J., & Salvucci, M. E. (2002). Sensitivity of photosynthesis in a C4 plant, mazie, to heat stress. *Plant Physiology*, *129*, 1773–1780.

Dai, A., Rasmussen, R. M., Liu, C., Ikeda, K., & Prein, A. F. (2020). A new mechanism for warm-season precipitation response to global warming based on convection-permitting simulations. *Climate Dynamics*, *55*(1–2), 343–368. https://doi.org/10.1007/s00382-017-3787-6

Dastane, N. G. (1978). Effective rainfall in irrigated agriculture. *FAO Irrigation and Drainage Engineering*, *4*(1), 25. https://doi.org/ISBN 92-5-100272-X

de Bruyn, L. P., & de Jager, J. M. (1978). A meteorological approach to the identification of drought sensitive periods in field crops. *Agricultural Meteorology*, *19*, 35–40.

De Cian, E., Hof, A. F., Marangoni, G., Tavoni, M., & Van Vuuren, D. P. (2016). Alleviating inequality in climate policy costs: An integrated perspective on mitigation, damage and adaptation. *Environmental Research Letters*, *11*(7). https://doi.org/10.1088/1748-9326/11/7/074015

Dellink, R., Chateau, J., Lanzi, E., & Magné, B. (2017). Long-term economic growth projections in the Shared Socioeconomic Pathways. *Global Environmental Change*, *42*, 200–214. https://doi.org/10.1016/j.gloenvcha.2015.06.004

Deryng, D., Elliott, J., Folberth, C., Müller, C., Pugh, T. A. M., Boote, K. J., Conway, D., Ruane, A. C., Gerten, D., Jones, J. W., Khabarov, N., Olin, S., Schaphoff, S., Schmid, E., Yang, H., & Rosenzweig, C. (2016). Regional disparities in the beneficial effects of rising CO2 concentrations on crop water productivity. *Nature Climate Change*, *6*(8), 786–790.

https://doi.org/10.1038/nclimate2995

Diaz, D. B. (2016). Estimating global damages from sea level rise with the Coastal Impact and Adaptation Model (CIAM). *Climatic Change*, *137*(1–2), 143–156. https://doi.org/10.1007/s10584-016-1675-4

Dottori, F., Szewczyk, W., Ciscar, J. C., Zhao, F., Alfieri, L., Hirabayashi, Y., Bianchi, A., Mongelli, I., Frieler, K., Betts, R. A., & Feyen, L. (2018). Increased human and economic losses from river flooding with anthropogenic warming. *Nature Climate Change*, *8*(9), 781–786. https://doi.org/10.1038/s41558-018-0257-z

Entekhabi, B. D., Njoku, E. G., Neill, P. E. O., Kellogg, K. H., Crow, W. T., Edelstein, W. N., Entin, J. K., Goodman, S. D., Jackson, T. J., Johnson, J., Kimball, J., Piepmeier, J. R., Koster, R. D., Martin, N., Mcdonald, K. C., Moghaddam, M., Moran, S., Reichle, R., Shi, J. C., … Zyl, J. Van. (2010). TheSoilMoistureActivePassive (SMAP). *IEEE Proceedings*, *98*(5), 704–716.

Eskander, S. M. S. U., & Fankhauser, S. (2020). Reduction in greenhouse gas emissions from national climate legislation. *Nature Climate Change*, *10*(8), 750–756. https://doi.org/10.1038/s41558-020-0831-z

Eyring, V., Bony, S., Meehl, G. A., Senior, C. A., Stevens, B., Stouffer, R. J., & Taylor, K. E. (2016). Overview of the Coupled Model Intercomparison Project Phase 6 (CMIP6) experimental design and organization. *Geoscientific Model Development*, *9*(5), 1937–1958. https://doi.org/10.5194/gmd-9-1937-2016

Fankhauser, S., & Tol, R. S. J. (2005). On climate change and economic growth. *Resource and Energy Economics*, *27*(1), 1–17. https://doi.org/10.1016/j.reseneeco.2004.03.003

Fisher-Vanden, K., Sue Wing, I., Lanzi, E., & Popp, D. (2013). Modeling climate change

feedbacks and adaptation responses: Recent approaches and shortcomings. *Climatic Change*, *117*(3), 481–495. https://doi.org/10.1007/s10584-012-0644-9

Fishman, R. (2016). More uneven distributions overturn benefits of higher precipitation for crop yields. *Environmental Research Letters*, *11*(024004).

Fowler, H. J., Lenderink, G., Prein, A. F., Westra, S., Allan, R. P., Ban, N., Barbero, R., Berg, P., Blenkinsop, S., Do, H. X., Guerreiro, S., Haerter, J. O., Kendon, E. J., Lewis, E., Schaer, C., Sharma, A., Villarini, G., Wasko, C., & Zhang, X. (2021). Anthropogenic intensification of short-duration rainfall extremes. *Nature Reviews Earth and Environment*, *2*(2), 107–122. https://doi.org/10.1038/s43017-020-00128-6

Fox-Kemper, B., Hewitt, H. T., Xiao, C., Aðalgeirsdóttir, G., Drijfhout, S. S., Edwards, T. L., Golledge, N. R., Hemer, M., Kopp, R. E., Krinner, G., Mix, A., Notz, D., Nowiciki, S., Nurhati, I. S., Ruiz, J., Sallée, J.-B., Slangen, A. B. A., & Yu, Y. (2021). Ocean, Cryosphere and Sea Level Change. *Climate Change 2021: The Physical Science Basis. Contribution of Working Group I to the Sixth Assessment Report of the Intergovernmental Panel on Climate ChangeScience Basis. Contribution of Working Group I to the Sixth Assessment Report of the Intergover*, *2018*(August), 1–257.

Frieler, K., Schauberger, B., Arneth, A., Balkovič, J., Chryssanthacopoulos, J., Deryng, D., Elliott, J., Folberth, C., Khabarov, N., Müller, C., Olin, S., Pugh, T. A. M., Schaphoff, S., Schewe, J., Schmid, E., Warszawski, L., & Levermann, A. (2017). Understanding the weather signal in national crop-yield variability. *Earth s Future*, *5*(6), 605–616. https://doi.org/10.1002/2016EF000525

Gambhir, A., Rogelj, J., Luderer, G., Few, S., & Napp, T. (2019). Energy system changes in 1.5 °C, well below 2 °C and 2 °C scenarios. *Energy Strategy Reviews*, *23*(July 2018), 69–80.

https://doi.org/10.1016/j.esr.2018.12.006

Gampe, D., Zscheischler, J., Reichstein, M., O'Sullivan, M., Smith, W. K., Sitch, S., & Buermann, W. (2021). Increasing impact of warm droughts on northern ecosystem productivity over recent decades. *Nature Climate Change*, *11*(9), 772–779. https://doi.org/10.1038/s41558-021-01112-8

Gates, D. M. (1968). Transpiration and leaf temperature. *Annu. Rev. Plant. Physiol.*, *19*, 211–238.

Grossiord, C., Buckley, T. N., Cernusak, L. A., Novick, K. A., Poulter, B., Siegwolf, R. T. W., Sperry, J. S., & McDowell, N. G. (2020). Plant responses to rising vapor pressure deficit. *New Phytologist*, *226*(6), 1550–1566. https://doi.org/10.1111/nph.16485

Grubler, A., Wilson, C., Bento, N., Boza-Kiss, B., Krey, V., McCollum, D. L., Rao, N. D., Riahi, K., Rogelj, J., De Stercke, S., Cullen, J., Frank, S., Fricko, O., Guo, F., Gidden, M., Havlík, P., Huppmann, D., Kiesewetter, G., Rafaj, P., … Valin, H. (2018). A low energy demand scenario for meeting the 1.5 °c target and sustainable development goals without negative emission technologies. *Nature Energy*, *3*(6), 515–527. https://doi.org/10.1038/s41560-018-0172-6

Hammond, G. P., & Jones, C. I. (2008). Embodied energy and carbon in construction materials. *Proceedings of Institution of Civil Engineers: Energy*, *161*(2), 87–98. https://doi.org/10.1680/ener.2008.161.2.87

Harris, I., Jones, P. D., Osborn, T. J., & Lister, D. H. (2014). Updated high-resolution grids of monthly climatic observations – the CRU TS3.10 dataset. *Int. J. Climatol.*, *34*, 623–642.

Harvell, C. D., Mitchell, C., Ward, J., Altizer, S., Dobson, A., Ostfeld, R., Harvell, C. D., Mitchell, C. E., Ward, J. R., Altizer…, S., Altizer, S., Dobson, A. P., Ostfeld, R. S., &

Samuel, M. D. (2002). Climate warming and disease risks for terrestrial and marine biota. *Science*, *296*, 2158–2162. https://doi.org/10.1126/science.1063699

Hauer, M. E., Fussell, E., Mueller, V., Burkett, M., Call, M., Abel, K., McLeman, R., & Wrathall, D. (2020). Sea-level rise and human migration. *Nature Reviews Earth & Environment*, *1*(1), 28–39. https://doi.org/10.1038/s43017-019-0002-9

He, Y., Lee, E., & Mankin, J. S. (2020). Seasonal tropospheric cooling in Northeast China associated with cropland expansion. *Environmental Research Letters*, *15*(3). https://doi.org/10.1088/1748-9326/ab6616

Hersbach, H., Bell, B., Berrisford, P., Hirahara, S., Horányi, A., Muñoz-Sabater, J., Nicolas, J., Peubey, C., Radu, R., Schepers, D., Simmons, A., Soci, C., Abdalla, S., Abellan, X., Balsamo, G., Bechtold, P., Biavati, G., Bidlot, J., Bonavita, M., … Thépaut, J. N. (2020). The ERA5 global reanalysis. *Quarterly Journal of the Royal Meteorological Society*, *146*(730), 1999–2049. https://doi.org/10.1002/qj.3803

Hinkel, J., Lincke, D., Vafeidis, A. T., Perrette, M., Nicholls, R. J., Tol, R. S. J., Marzeion, B., Fettweis, X., Ionescu, C., & Levermann, A. (2014). Coastal flood damage and adaptation costs under 21st century sea-level rise. *Proceedings of the National Academy of Sciences of the United States of America*, *111*(9), 3292–3297. https://doi.org/10.1073/pnas.1222469111

Hoegh-Guldberg, O., Jacob, D., & Taylor, M. (2018). Impacts of 1.5°C of Global Warming on Natural and Human Systems. In *Special Report, Intergovernmental Panel on Climate Change* (Issue ISBN 978-92-9169-151-7, pp. 175–181). http://report.ipcc.ch/sr15/pdf/sr15_chapter3.pdf

Horen Greenford, D., Crownshaw, T., Lesk, C., Stadler, K., & Matthews, H. D. (2020). Shifting economic activity to services has limited potential to reduce global environmental impacts

due to the household consumption of labour. *Environmental Research Letters*, *15*(6). https://doi.org/10.1088/1748-9326/ab7f63

Horton, R. M., de Sherbinin, A., Wrathall, D., & Oppenheimer, M. (2021). Assessing human habitability and migration. In *Science* (Vol. 372, Issue 6548, pp. 1279–1283). https://doi.org/10.1126/science.abi8603

Horton, R. M., Mankin, J. S., Lesk, C., Coffel, E., & Raymond, C. (2016). A Review of Recent Advances in Research on Extreme Heat Events. *Current Climate Change Reports*, *2*(4), 242–259. https://doi.org/10.1007/s40641-016-0042-x

Hubacek, K., Baiocchi, G., Feng, K., Muñoz Castillo, R., Sun, L., & Xue, J. (2017). Global carbon inequality. *Energy, Ecology and Environment*, *2*(6), 361–369. https://doi.org/10.1007/s40974-017-0072-9

IEA. (2021). *World Energy Balances: Overview*. https://www.iea.org/reports/world-energy-balances-overview

Jacobson, M. Z., Delucchi, M. A., Bauer, Z. A. F., Goodman, S. C., Chapman, W. E., Cameron, M. A., Bozonnat, C., Chobadi, L., Clonts, H. A., Enevoldsen, P., Erwin, J. R., Fobi, S. N., Goldstrom, O. K., Hennessy, E. M., Liu, J., Lo, J., Meyer, C. B., Morris, S. B., Moy, K. R., … Yachanin, A. S. (2017). 100% Clean and Renewable Wind, Water, and Sunlight All-Sector Energy Roadmaps for 139 Countries of the World. *Joule*, *1*(1), 108–121. https://doi.org/10.1016/j.joule.2017.07.005

Jägermeyr, J., Gerten, D., Schaphoff, S., Heinke, J., Lucht, W., & Rockström, J. (2016). Integrated crop water management might sustainably halve the global food gap. *Environmental Research Letters*, *11*(2). https://doi.org/10.1088/1748-9326/11/2/025002

Jägermeyr, Jonas, Müller, C., Ruane, A. C., Elliott, J., Balkovic, J., Castillo, O., Faye, B., Foster,

I., Folberth, C., Franke, J. A., Fuchs, K., Guarin, J. R., Heinke, J., Hoogenboom, G., Iizumi, T., Jain, A. K., Kelly, D., Khabarov, N., Lange, S., … Rosenzweig, C. (2021). Climate impacts on global agriculture emerge earlier in new generation of climate and crop models. *Nature Food*, *2*(11), 873–885. https://doi.org/10.1038/s43016-021-00400-y

Jonkman, S. N., Hillen, M. M., Nicholls, R. J., Kanning, W., & Van Ledden, M. (2013). Costs of adapting coastal defences to sea-level rise - New estimates and their implications. *Journal of Coastal Research*, *29*(5), 1212–1226. https://doi.org/10.2112/JCOASTRES-D-12-00230.1

Karl, T., Nicholls, N., & Ghazi, A. (1999). Workshop on Indices and Indicators for Climate Extremes Precipitation.pdf. In *Climate Change* (Vol. 42, pp. 3–7). https://doi.org/10.1007/978-94-015-9265-9_2

Kayaçetin, N. C., & Tanyer, A. M. (2020). Embodied carbon assessment of residential housing at urban scale. *Renewable and Sustainable Energy Reviews*, *117*(October 2019), 109470. https://doi.org/10.1016/j.rser.2019.109470

KC, S., & Lutz, W. (2017). The human core of the shared socioeconomic pathways: Population scenarios by age, sex and level of education for all countries to 2100. *Global Environmental Change*, *42*, 181–192. https://doi.org/10.1016/j.gloenvcha.2014.06.004

Kellenberger, D., Althaus, H.-J., Jungbluth, N., Künninger, T., Lehmann, M., & Thalmann, P. (2007). Life Cycle inventories of Building Products. *Final Report Ecoinvent Data v2.0*, *7*, 914.

Kendon, E. J., Roberts, N. M., Fowler, H. J., Roberts, M. J., Chan, S. C., & Senior, C. A. (2014). Heavier summer downpours with climate change revealed by weather forecast resolution model. *Nature Climate Change*, *4*, 570–576. https://doi.org/10.1038/NCLIMATE2258

Keyßer, L. T., & Lenzen, M. (2021). 1.5 °C degrowth scenarios suggest the need for new mitigation pathways. *Nature Communications*, *12*(1), 1–16. https://doi.org/10.1038/s41467-021-22884-9

Knutti, R., Rogelj, J., Sedlácek, J., & Fischer, E. M. (2016). A scientific critique of the two-degree climate change target. *Nature Geoscience*, *9*(1), 13–18. https://doi.org/10.1038/ngeo2595

Kopp, R. E., Horton, R. M., Little, C. M., Mitrovica, J. X., Oppenheimer, M., Rasmussen, D. J., Strauss, B. H., & Tebaldi, C. (2014). Probabilistic 21st and 22nd century sea-level projections at a global network of tide-gauge sites. *Earth s Future*, *2*(8), 383–406. https://doi.org/10.1002/2014ef000239

Koster, R. D., Chang, Y., Wang, H., & Schubert, S. D. (2016). Impacts of local soil moisture anomalies on the atmospheric circulation and on remote surface meteorological fields during boreal summer: A comprehensive analysis over North America. *Journal of Climate*, *29*(20), 7345–7364. https://doi.org/10.1175/JCLI-D-16-0192.1

Krajewski W.F., & Smith J.A. (2002). Radar hydrology: rainfall estimation. *Advances in Water Resources*, *25*, 1387–1394. https://doi.org/10.1016/S0309-1708(02)00062-3

Lau, W. K., Wu, H., & Kim, K. (2013). *A canonical response of precipitation characteristics to global warming from CMIP5 models*. *40*(June), 3163–3169. https://doi.org/10.1002/grl.50420

Lenderink, G., & Van Meijgaard, E. (2008). Increase in hourly precipitation extremes beyond expectations from temperature changes. *Nature Geoscience*, *1*, 511–514. https://doi.org/10.1038/ngeo262

Leonard, M., Westra, S., Hurk, B. Van Den, Mcinnes, K., & Risbey, J. (2013). *Understanding*

the role of compound events in for understanding extreme impacts. *April*. https://doi.org/10.1002/wcc.252

Lepore, C., Allen, J. T., & Tippett, M. K. (2016). Relationships between hourly rainfall intensity and atmospheric variables over the contiguous United States. *Journal of Climate*, *29*(9), 3181–3197. https://doi.org/10.1175/JCLI-D-15-0331.1

Lesk, C., & Anderson, W. (2021). Decadal variability modulates trends in concurrent heat and drought over global croplands. *Environmental Research Letters*.

Lesk, C., Coffel, E., & Horton, R. (2020). Net benefits to US soy and maize yields from intensifying hourly rainfall. *Nature Climate Change*, *10*(9), 819–822. https://doi.org/10.1038/s41558-020-0830-0

Lesk, C., Rowhani, P., & Ramankutty, N. (2016). Influence of extreme weather disasters on global crop production. *Nature*, *529*(7584), 84–87. https://doi.org/10.1038/nature16467

Lesnikowski, A., Ford, J., Biesbroek, R., Berrang-Ford, L., Maillet, M., Araos, M., & Austin, S. E. (2017). What does the Paris Agreement mean for adaptation? *Climate Policy*, *17*(7), 825–831. https://doi.org/10.1080/14693062.2016.1248889

Levesque, A., Pietzcker, R. C., Baumstark, L., De Stercke, S., Grübler, A., & Luderer, G. (2018). How much energy will buildings consume in 2100? A global perspective within a scenario framework. *Energy*, *148*, 514–527. https://doi.org/10.1016/j.energy.2018.01.139

Li, Y., Guan, K., Schnitkey, G. D., Delucia, E., & Peng, B. (2019). Excessive rainfall leads to maize yield loss of a comparable magnitude to extreme drought in the United States. *Global Change Biology*, *October 2018*, 1–13. https://doi.org/10.1111/gcb.14628

Lian, X., Piao, S., Huntingford, C., Li, Y., Zeng, Z., Wang, X., Ciais, P., McVicar, T. R., Peng, S., Ottlé, C., Yang, H., Yang, Y., Zhang, Y., & Wang, T. (2018). Partitioning global land

evapotranspiration using CMIP5 models constrained by observations. *Nature Climate Change*, *8*(7), 640–646. https://doi.org/10.1038/s41558-018-0207-9

Lin, Y. (2011). GCIP/EOP Surface: Precipitation NCEP/EMC 4KM Gridded Data (GRIB) Stage IV Data. *UCAR/NCAR - Earth Observing Laboratory*. https://doi.org/https://doi.org/10.5065/D6PG1QDD

Lincke, D., & Hinkel, J. (2021). Coastal Migration due to 21st Century Sea-Level Rise. *Earth s Future*, *9*(5), 1–14. https://doi.org/10.1029/2020EF001965

Liu, B., Asseng, S., Müller, C., Ewert, F., Elliott, J., Lobell, D. B., Martre, P., Ruane, A. C., Wallach, D., Jones, J. W., Rosenzweig, C., Aggarwal, P. K., Alderman, P. D., Anothai, J., Basso, B., Biernath, C., Cammarano, D., Challinor, A., Deryng, D., … Zhu, Y. (2016). Similar estimates of temperature impacts on global wheat yield by three independent methods. *Nature Climate Change*, *6*(12), 1130–1136. https://doi.org/10.1038/nclimate3115

Lobell, D. B., & Gourdji, S. M. (2012). The Influence of Climate Change on Global Crop Productivity. *Plant Physiology*, *160*(4), 1686–1697. https://doi.org/10.1104/pp.112.208298

Lobell, D. B., Hammer, G. L., McLean, G., Messina, C., Roberts, M. J., & Schlenker, W. (2013). The critical role of extreme heat for maize production in the United States. *Nature Climate Change*, *3*(5), 497–501. https://doi.org/10.1038/nclimate1832

Lobell, David B., Bänziger, M., Magorokosho, C., & Vivek, B. (2011). Nonlinear heat effects on African maize as evidenced by historical yield trials. *Nature Climate Change*, *1*(1), 42–45. https://doi.org/10.1038/nclimate1043

Lobell, David B., Deines, J. M., & Tommaso, S. Di. (2020). Changes in the drought sensitivity of US maize yields. *Nature Food*, *1*(11), 729–735. https://doi.org/10.1038/s43016-020-00165-w

Lobell, David B, & Burke, M. B. (2008). Why are agricultural impacts of climate change so uncertain? The importance of temperature relative to precipitation. *Environmental Research Letters*, *3*, 1–8. https://doi.org/10.1088/1748-9326/3/3/034007

Lobell, David B, & Field, C. B. (2007a). Global scale climate – crop yield relationships and the impacts of recent warming. *Environmental Research Letters*. https://doi.org/10.1088/1748-9326/2/1/014002

Lobell, David B, & Field, C. B. (2007b). Global scale climate – crop yield relationships and the impacts of recent warming. *Environmental Research Letters*, *2*. https://doi.org/10.1088/1748-9326/2/1/014002

Luderer, G., Madeddu, S., Merfort, L., Ueckerdt, F., Pehl, M., Pietzcker, R., Rottoli, M., Schreyer, F., Bauer, N., Baumstark, L., Bertram, C., Dirnaichner, A., Humpenöder, F., Levesque, A., Popp, A., Rodrigues, R., Strefler, J., & Kriegler, E. (2021). Impact of declining renewable energy costs on electrification in low-emission scenarios. *Nature Energy*. https://doi.org/10.1038/s41560-021-00937-z

Luderer, G., Vrontisi, Z., Bertram, C., Edelenbosch, O. Y., Pietzcker, R. C., Rogelj, J., De Boer, H. S., Drouet, L., Emmerling, J., Fricko, O., Fujimori, S., Havlík, P., Iyer, G., Keramidas, K., Kitous, A., Pehl, M., Krey, V., Riahi, K., Saveyn, B., … Kriegler, E. (2018). Residual fossil CO2 emissions in 1.5-2 °c pathways. *Nature Climate Change*, *8*(7), 626–633. https://doi.org/10.1038/s41558-018-0198-6

MacDonald, A. E., Clack, C. T. M., Alexander, A., Dunbar, A., Wilczak, J., & Xie, Y. (2016). Future cost-competitive electricity systems and their impact on US CO2 emissions. *Nature Climate Change*, *6*(5), 526–531. https://doi.org/10.1038/nclimate2921

Mach, K. J., & Siders, A. R. (2021). Reframing strategic, managed retreat for transformative

climate adaptation. *Science*, *372*(6548), 1294–1299. https://doi.org/10.1126/science.abh1894

Martínez-Casasnovas, J. A., Ramos, M. C., & Ribes-Dasi, M. (2002). Soil erosion caused by extreme rainfall events: Mapping and quantification in agricultural plots from very detailed digital elevation models. *Geoderma*, *105*(1–2), 125–140. https://doi.org/10.1016/S0016-7061(01)00096-9

Matiu, M., Ankerst, D. P., & Menzel, A. (2017). Interactions between temperature and drought in global and regional crop yield variability during 1961-2014. *PLoS ONE*, *12*(5), 1–23.

Matthews, H. D. (2016). Quantifying historical carbon and climate debts among nations. *Nature Climate Change*, *6*(1), 60–64. https://doi.org/10.1038/nclimate2774

Matthews, H. D., Tokarska, K. B., Nicholls, Z. R. J., Rogelj, J., Canadell, J. G., Friedlingstein, P., Frölicher, T. L., Forster, P. M., Gillett, N. P., Ilyina, T., Jackson, R. B., Jones, C. D., Koven, C., Knutti, R., MacDougall, A. H., Meinshausen, M., Mengis, N., Séférian, R., & Zickfeld, K. (2020). Opportunities and challenges in using remaining carbon budgets to guide climate policy. *Nature Geoscience*, *13*(12), 769–779. https://doi.org/10.1038/s41561-020-00663-3

McDermid, S. S., Cook, B. I., De Kauwe, M. G., Mankin, J., Smerdon, J. E., Williams, A. P., Seager, R., Puma, M. J., Aleinov, I., Kelley, M., & Nazarenko, L. (2021). Disentangling the Regional Climate Impacts of Competing Vegetation Responses to Elevated Atmospheric CO2. *Journal of Geophysical Research: Atmospheres*, *126*(5), 1–23. https://doi.org/10.1029/2020JD034108

McMichael, C., Dasgupta, S., Ayeb-Karlsson, S., & Kelman, I. (2020). A review of estimating population exposure to sea-level rise and the relevance for migration. *Environmental*

Research Letters, *15*(12). https://doi.org/10.1088/1748-9326/abb398

Meinshausen, M., Smith, S. J., Calvin, K., Daniel, J. S., Kainuma, M. L. T., Lamarque, J., Matsumoto, K., Montzka, S. A., Raper, S. C. B., Riahi, K., Thomson, A., Velders, G. J. M., & van Vuuren, D. P. P. (2011). The RCP greenhouse gas concentrations and their extensions from 1765 to 2300. *Climatic Change*, *109*(1), 213–241. https://doi.org/10.1007/s10584-011-0156-z

Meisinger, J. J., & Delgado, J. A. (2002). Principles for managing nitrogen leaching. *Journal of Soil and Water Conservation*, *57*(6), 485–498.

Miralles, D. G., Gentine, P., Seneviratne, S. I., & Teuling, A. J. (2019). Land–atmospheric feedbacks during droughts and heatwaves: state of the science and current challenges. *Annals of the New York Academy of Sciences*, *1436*(1), 19–35. https://doi.org/10.1111/nyas.13912

Miralles, D. G., Teuling, A. J., Van Heerwaarden, C. C., & De Arellano, J. V. G. (2014). Mega-heatwave temperatures due to combined soil desiccation and atmospheric heat accumulation. *Nature Geoscience*, *7*(5), 345–349. https://doi.org/10.1038/ngeo2141

Mittler, R. (2006). *Abiotic stress , the field environment and stress combination*. *11*(1). https://doi.org/10.1016/j.tplants.2005.11.002

Monahan, J., & Powell, J. C. (2011). An embodied carbon and energy analysis of modern methods of construction in housing: A case study using a lifecycle assessment framework. *Energy and Buildings*, *43*(1), 179–188. https://doi.org/10.1016/j.enbuild.2010.09.005

Moore, C. E., Meacham-Hensold, K., Lemonnier, P., Slattery, R. A., Benjamin, C., Bernacchi, C. J., Lawson, T., & Cavanagh, A. P. (2021). The effect of increasing temperature on crop photosynthesis: From enzymes to ecosystems. *Journal of Experimental Botany*, *72*(8),

2822–2844. https://doi.org/10.1093/jxb/erab090

Moore, F. C., Lacasse, K., Mach, K. J., Shin, Y. A., Gross, L. J., & Beckage, B. (2022). Determinants of emissions pathways in the coupled climate–social system. *Nature*, *603*(7899), 103–111. https://doi.org/10.1038/s41586-022-04423-8

Mueller, B., Seneviratne, S. I., Jimenez, C., Corti, T., Hirschi, M., Balsamo, G., Ciais, P., Dirmeyer, P., Fisher, J. B., Guo, Z., Jung, M., Maignan, F., McCabe, M. F., Reichle, R., Reichstein, M., Rodell, M., Sheffield, J., Teuling, A. J., Wang, K., … Zhang, Y. (2011). Evaluation of global observations-based evapotranspiration datasets and IPCC AR4 simulations. *Geophysical Research Letters*, *38*(6), 1–7. https://doi.org/10.1029/2010GL046230

Mueller, Brigitte, & Seneviratne, S. I. (2012). Hot days induced by precipitation deficits at the global scale. *Proceedings of the National Academy of Sciences of the United States of America*, *109*(31), 12398–12403. https://doi.org/10.1073/pnas.1204330109

Mueller, N. D., Rhines, A., Butler, E. E., Ray, D. K., Siebert, S., Holbrook, N. M., & Huybers, P. (2017). Global relationships between cropland intensification and summer temperature extremes over the last 50 years. *Journal of Climate*, *30*(18), 7505–7528. https://doi.org/10.1175/JCLI-D-17-0096.1

Munkvold, G. P. (2003). Epidemiology of Fusarium diseases and their mycotoxins in maize ears. *European Journal of Plant Pathology*, *109*(7), 705–713. https://doi.org/10.1023/A:1026078324268

Myhrvold, N. P., & Caldeira, K. (2012). Greenhouse gases, climate change and the transition from coal to low-carbon electricity. *Environmental Research Letters*, *7*(1). https://doi.org/10.1088/1748-9326/7/1/014019

Ning, G., Luo, M., Zhang, W., Liu, Z., Wang, S., & Gao, T. (2022). Rising risks of compound extreme heat-precipitation events in China. *International Journal of Climatology*, 0–2. https://doi.org/10.1002/joc.7561

O'Gorman, P., & Schneider, T. (2009). The physical basis for increases in precipitation extremes in simulations of 21st-century climate change. *Proceedings of the National Academy of Sciences*, *106*(35), 14773–14777.

O'Neill, B. C., Kriegler, E., Ebi, K. L., Kemp-Benedict, E., Riahi, K., Rothman, D. S., van Ruijven, B. J., van Vuuren, D. P., Birkmann, J., Kok, K., Levy, M., & Solecki, W. (2017). The roads ahead: Narratives for shared socioeconomic pathways describing world futures in the 21st century. *Global Environmental Change*, *42*, 169–180. https://doi.org/10.1016/j.gloenvcha.2015.01.004

Orlowsky, B., & Seneviratne, S. I. (2010). Statistical analyses of land-atmosphere feedbacks and their possible pitfalls. *Journal of Climate*, *23*(14), 3918–3932. https://doi.org/10.1175/2010JCLI3366.1

Ortiz-Bobea, A., Wang, H., Carrillo, C. M., & Ault, T. R. (2019). Unpacking the climatic drivers of US agricultural yields. *Environmental Research Letters*, *14*(6). https://doi.org/10.1088/1748-9326/ab1e75

Ostmeyer, T., Parker, N., Jaenisch, B., Alkotami, L., Bustamante, C., & Jagadish, S. V. K. (2020). Impacts of heat, drought, and their interaction with nutrients on physiology, grain yield, and quality in field crops. *Plant Physiology Reports*, *25*(4), 549–568. https://doi.org/10.1007/s40502-020-00538-0

Pahle, M., Tietjen, O., Osorio, S., Egli, F., Steffen, B., Schmidt, T. S., & Edenhofer, O. (2022). Safeguarding the energy transition against political backlash to carbon markets. *Nature*

Energy. https://doi.org/10.1038/s41560-022-00984-0

Palecki, M. A., Angel, J. R., & Hollinger, S. E. (2005). Storm Precipitation in the United States. Part I: Meteorological Characteristics. *Journal of Applied Meteorology*, *44*(6), 933–946. https://doi.org/10.1175/jam2243.1

Pendergrass, A. G., Meehl, G. A., Pulwarty, R., Hobbins, M., Hoell, A., AghaKouchak, A., Bonfils, C. J. W., Gallant, A. J. E., Hoerling, M., Hoffmann, D., Kaatz, L., Lehner, F., Llewellyn, D., Mote, P., Neale, R. B., Overpeck, J. T., Sheffield, A., Stahl, K., Svoboda, M., … Woodhouse, C. A. (2020). Flash droughts present a new challenge for subseasonal-to-seasonal prediction. *Nature Climate Change*, *10*(3), 191–199. https://doi.org/10.1038/s41558-020-0709-0

Pfeiffer, A., Hepburn, C., Vogt-schilb, A., & Caldecott, B. (2018). *Committed emissions from existing and planned power plants and asset stranding required to meet the Paris Agreement OPEN ACCESS Committed emissions from existing and planned power plants and asset stranding required to meet the Paris Agreement*.

Prasad, P. V. V., Staggenborg, S. A., Ristic, Z., Ahuja, L. R., Reddy, V. R., Saseendran, S. A., & Yu, Q. (2008). *Impacts of Drought and/or Heat Stress on Physiological, Developmental, Growth, and Yield Processes of Crop Plants*. 301–356. https://doi.org/10.2134/advagricsystmodel1.c11

Prein, A. F., Rasmussen, R. M., Ikeda, K., Liu, C., Clark, M. P., & Holland, G. J. (2017). The future intensification of hourly precipitation extremes. *Nature Climate Change*, *7*(1), 48–52. https://doi.org/10.1038/nclimate3168

Qin, Y., Abatzoglou, J. T., Siebert, S., Huning, L. S., AghaKouchak, A., Mankin, J. S., Hong, C., Tong, D., Davis, S. J., & Mueller, N. D. (2020). Agricultural risks from changing snowmelt.

Nature Climate Change, *10*(5), 459–465. https://doi.org/10.1038/s41558-020-0746-8

Ramage, M. H., Burridge, H., Busse-Wicher, M., Fereday, G., Reynolds, T., Shah, D. U., Wu, G., Yu, L., Fleming, P., Densley-Tingley, D., Allwood, J., Dupree, P., Linden, P. F., & Scherman, O. (2017). The wood from the trees: The use of timber in construction. *Renewable and Sustainable Energy Reviews*, *68*(October 2016), 333–359. https://doi.org/10.1016/j.rser.2016.09.107

Ramirez-Villegas, J., Molero Milan, A., Alexandrov, N., Asseng, S., Challinor, A. J., Crossa, J., van Eeuwijk, F., Ghanem, M. E., Grenier, C., Heinemann, A. B., Wang, J., Juliana, P., Kehel, Z., Kholova, J., Koo, J., Pequeno, D., Quiroz, R., Rebolledo, M. C., Sukumaran, S., … Reynolds, M. (2020). CGIAR modeling approaches for resource-constrained scenarios: I. Accelerating crop breeding for a changing climate. *Crop Science*, *60*(2), 547–567. https://doi.org/10.1002/csc2.20048

Ray, D. K., Gerber, J. S., Macdonald, G. K., & West, P. C. (2015). Climate variation explains a third of global crop yield variability. *Nature Communications*, *6*, 1–9. https://doi.org/10.1038/ncomms6989

Ray, D. K., West, P. C., Clark, M., Gerber, J. S., Prishchepov, A. V., & Chatterjee, S. (2019). Climate change has likely already affected global food production. *PLoS ONE*, *14*(5), 1–18. https://doi.org/10.1371/journal.pone.0217148

Raymond, C., Horton, R. M., Zscheischler, J., Martius, O., AghaKouchak, A., Balch, J., Bowen, S. G., Camargo, S. J., Hess, J., Kornhuber, K., Oppenheimer, M., Ruane, A. C., Wahl, T., & White, K. (2020). Understanding and managing connected extreme events. *Nature Climate Change*, *10*(7), 611–621. https://doi.org/10.1038/s41558-020-0790-4

Ridder, N. N., Ukkola, A. M., Pitman, A. J., & Perkins-Kirkpatrick, S. E. (2022). Increased

occurrence of high impact compound events under climate change. *Npj Climate and Atmospheric Science*, *5*(1), 1–8. https://doi.org/10.1038/s41612-021-00224-4

Rigden, A. J., Mueller, N. D., Holbrook, N. M., Pillai, N., & Huybers, P. (2020). Combined influence of soil moisture and atmospheric evaporative demand is important for accurately predicting US maize yields. *Nature Food*, *1*(February). https://doi.org/10.1038/s43016-020-0028-7

Rodell, M., Houser, P. R., Jambor, U., Gottschalck, J., Mitchell, K., Meng, C. J., Arsenault, K., Cosgrove, B., Radakovich, J., Bosilovich, M., Entin, J. K., Walker, J. P., Lohmann, D., & Toll, D. (2004). The Global Land Data Assimilation System. *Bulletin of the American Meteorological Society*, *85*(3), 381–394. https://doi.org/10.1175/BAMS-85-3-381

Rogelj, J., Den Elzen, M., Höhne, N., Fransen, T., Fekete, H., Winkler, H., Schaeffer, R., Sha, F., Riahi, K., & Meinshausen, M. (2016). Paris Agreement climate proposals need a boost to keep warming well below 2 °c. *Nature*, *534*(7609), 631–639. https://doi.org/10.1038/nature18307

Rogelj, J., McCollum, D. L., Reisinger, A., Meinshausen, M., & Riahi, K. (2013). Probabilistic cost estimates for climate change mitigation. *Nature*, *493*(7430), 79–83. https://doi.org/10.1038/nature11787

Rogelj, J., Popp, A., Calvin, K. V., Luderer, G., Emmerling, J., Gernaat, D., Fujimori, S., Strefler, J., Hasegawa, T., Marangoni, G., Krey, V., Kriegler, E., Riahi, K., Van Vuuren, D. P., Doelman, J., Drouet, L., Edmonds, J., Fricko, O., Harmsen, M., … Tavoni, M. (2018). Scenarios towards limiting global mean temperature increase below 1.5 °c. *Nature Climate Change*, *8*(4), 325–332. https://doi.org/10.1038/s41558-018-0091-3

Rosa, L., Chiarelli, D. D., Rulli, M. C., Dell'Angelo, J., & D'Odorico, P. (2020). Global

agricultural economic water scarcity. *Science Advances*, *6*(18), 1–11. https://doi.org/10.1126/sciadv.aaz6031

Rosa, L., Chiarelli, D. D., Sangiorgio, M., Beltran-Peña, A. A., Rulli, M. C., D'Odorico, P., & Fung, I. (2020). Potential for sustainable irrigation expansion in a 3 °c warmer climate. *Proceedings of the National Academy of Sciences of the United States of America*, *117*(47), 29526–29534. https://doi.org/10.1073/pnas.2017796117

Rosenzweig, C., Elliott, J., Deryng, D., Ruane, A. C., Müller, C., Arneth, A., Boote, K. J., Folberth, C., Glotter, M., Khabarov, N., Neumann, K., Piontek, F., Pugh, T. A. M., Schmid, E., Stehfest, E., Yang, H., & Jones, J. W. (2014). Assessing agricultural risks of climate change in the 21st century in a global gridded crop model intercomparison. *Proceedings of the National Academy of Sciences*, *111*(9), 3268–3273. https://doi.org/10.1073/pnas.1222463110

Rosenzweig, C., Tubiello, F. N., Goldberg, R., Mills, E., & Bloomfield, J. (2002). Increased crop damage in the US from excess precipitation under climate change. *Global Environmental Change*, *12*(3), 197–202. https://doi.org/10.1016/S0959-3780(02)00008-0

Sacks, W. J., Deryng, D., & Foley, J. A. (2010). Crop planting dates : an analysis of global patterns. *Global Ecology and Biogeography*, *19*(5), 607–620. https://doi.org/10.1111/j.1466-8238.2010.00551.x

Sánchez, B., Rasmussen, A., & Porter, J. R. (2014). Temperatures and the growth and development of maize and rice: A review. *Global Change Biology*, *20*(2), 408–417. https://doi.org/10.1111/gcb.12389

Sarhadi, A., Ausín, M. C., Wiper, M. P., Touma, D., & Diffenbaugh, N. S. (2018). Multidimensional risk in a nonstationary climate : Joint probability of increasingly severe

warm and dry conditions. *Science Advances*, *4*.

Schauberger, B., Archontoulis, S., Arneth, A., Balkovic, J., Ciais, P., Deryng, D., Elliott, J., Folberth, C., Khabarov, N., Müller, C., Pugh, T. A. M., Rolinski, S., Schaphoff, S., Schmid, E., Wang, X., Schlenker, W., & Frieler, K. (2017). Consistent negative response of US crops to high temperatures in observations and crop models. *Nature Communications*, *8*. https://doi.org/10.1038/ncomms13931

Scheff, J., Mankin, J. S., Coats, S., & Liu, H. (2021). CO2-plant effects do not account for the gap between dryness indices and projected dryness impacts in CMIP6 or CMIP5. *Environmental Research Letters*, *16*(3). https://doi.org/10.1088/1748-9326/abd8fd

Schlenker, W., & Roberts, M. J. (2009). Nonlinear temperature effects indicate severe damages to U.S. crop yields under climate change. *Proceedings of the National Academy of Sciences*, *106*(37), 15594–15598. https://doi.org/10.1073/pnas.0906865106

Schleussner, C. F., Deryng, D., Müller, C., Elliott, J., Saeed, F., Folberth, C., Liu, W., Wang, X., Pugh, T. A. M., Thiery, W., Seneviratne, S. I., & Rogelj, J. (2018). Crop productivity changes in 1.5 °c and 2 °c worlds under climate sensitivity uncertainty. *Environmental Research Letters*, *13*(6). https://doi.org/10.1088/1748-9326/aab63b

Schleussner, C. F., Rogelj, J., Schaeffer, M., Lissner, T., Licker, R., Fischer, E. M., Knutti, R., Levermann, A., Frieler, K., & Hare, W. (2016). Science and policy characteristics of the Paris Agreement temperature goal. *Nature Climate Change*, *6*(9), 827–835. https://doi.org/10.1038/nclimate3096

Seneviratne, S. I. (2019). Chapter 11: Weather and climate extreme events in a changing climate. In *Climate Change 2021: The Physical Science Basis. Contribution of Working Group I to the Sixth Assessment Report of the Intergovernmental Panel on Climate Change* (Vol. 46,

Issue 5, pp. 2573–2582).

Seneviratne, S. I., Corti, T., Davin, E. L., Hirschi, M., Jaeger, E. B., Lehner, I., Orlowsky, B., & Teuling, A. J. (2010). Investigating soil moisture-climate interactions in a changing climate: A review. *Earth-Science Reviews*, *99*(3–4), 125–161. https://doi.org/10.1016/j.earscirev.2010.02.004

Seneviratne, S. I., Donat, M. G., Pitman, A. J., Knutti, R., & Wilby, R. L. (2016). Allowable CO2 emissions based on regional and impact-related climate targets. *Nature*, *529*(7587), 477–483. https://doi.org/10.1038/nature16542

Seneviratne, S. I., Lüthi, D., Litschi, M., & Schär, C. (2006). Land-atmosphere coupling and climate change in Europe. *Nature*, *443*(7108), 205–209. https://doi.org/10.1038/nature05095

Sers, M. R., & Victor, P. A. (2018). The Energy-missions Trap. *Ecological Economics*, *151*(February), 10–21. https://doi.org/10.1016/j.ecolecon.2018.04.004

Seth, A., Giannini, A., Rojas, M., Rauscher, S. A., Bordoni, S., Singh, D., & Camargo, S. J. (2019). Monsoon Responses to Climate Changes—Connecting Past, Present and Future. *Current Climate Change Reports*, 63–79. https://doi.org/10.1007/s40641-019-00125-y

Seto, K. C., Davis, S. J., Mitchell, R. B., Stokes, E. C., Unruh, G., & Ürge-Vorsatz, D. (2016). Carbon Lock-In: Types, Causes, and Policy Implications. *Annual Review of Environment and Resources*, *41*, 425–452. https://doi.org/10.1146/annurev-environ-110615-085934

Sgouridis, S., Csala, D., & Bardi, U. (2016). The sower's way: Quantifying the narrowing net-energy pathways to a global energy transition. *Environmental Research Letters*, *11*(9). https://doi.org/10.1088/1748-9326/11/9/094009

Shortridge, J. (2019). Observed trends in daily rainfall variability result in more severe climate

change impacts to agriculture. *Climatic Change*, *157*(3–4), 429–444. https://doi.org/10.1007/s10584-019-02555-x

Siders, A. R., Hino, M., & Mach, K. J. (2019). The case for strategic and managed climate retreat. *Science*, *365*(6455), 761–763. https://doi.org/10.1126/science.aax8346

Siebert, S., Webber, H., Zhao, G., & Ewert, F. (2017). Heat stress is overestimated in climate impact studies for irrigated agriculture. *Environmental Research Letters*, *12*(5), 0–4. https://doi.org/10.1088/1748-9326/aa702f

Singh, D., McDermid, S. P., Cook, B. I., Puma, M. J., Nazarenko, L., & Kelley, M. (2018). Distinct Influences of Land Cover and Land Management on Seasonal Climate. *Journal of Geophysical Research: Atmospheres*, *123*(21), 12,017-12,039. https://doi.org/10.1029/2018JD028874

Sippel, S., Reichstein, M., Ma, X., Mahecha, M. D., Lange, H., Flach, M., & Frank, D. (2018). Drought, Heat, and the Carbon Cycle: a Review. *Current Climate Change Reports*, *4*(3), 266–286. https://doi.org/10.1007/s40641-018-0103-4

Skinner, C. B., Poulsen, C. J., & Mankin, J. S. (2018). Amplification of heat extremes by plant CO2 physiological forcing. *Nature Communications*, *9*(1), 1–11. https://doi.org/10.1038/s41467-018-03472-w

Suzuki, N., Rivero, R. M., Shulaev, V., Blumwald, E., & Mittler, R. (2014). Abiotic and biotic stress combinations. *New Phytologist*, *203*(1), 32–43. https://doi.org/10.1111/nph.12797

Swann, A. L. S. (2018). Plants and Drought in a Changing Climate. *Current Climate Change Reports*, *4*, 192–201.

Swann, A. L. S., Hoffman, F. M., Koven, C. D., & Randerson, J. T. (2016). Plant responses to increasing CO2 reduce estimates of climate impacts on drought severity. *Proceedings of the*

National Academy of Sciences of the United States of America, *113*(36), 10019–10024. https://doi.org/10.1073/pnas.1604581113

Teuling, A. J., Seneviratne, S. I., Stöckli, R., Reichstein, M., Moors, E., Ciais, P., Luyssaert, S., Van Den Hurk, B., Ammann, C., Bernhofer, C., Dellwik, E., Gianelle, D., Gielen, B., Grünwald, T., Klumpp, K., Montagnani, L., Moureaux, C., Sottocornola, M., & Wohlfahrt, G. (2010). Contrasting response of European forest and grassland energy exchange to heatwaves. *Nature Geoscience*, *3*(10), 722–727. https://doi.org/10.1038/ngeo950

Thiery, W., Visser, A. J., Fischer, E. M., Hauser, M., Hirsch, A. L., Lawrence, D. M., Lejeune, Q., Davin, E. L., & Seneviratne, S. I. (2020). Warming of hot extremes alleviated by expanding irrigation. *Nature Communications*, *11*(1), 1–7. https://doi.org/10.1038/s41467-019-14075-4

Thornton, P. E., Thornton, M. M., Mayer, B. W., Wilhelmi, N., Wei, Y., Devarakonda, R., & Cook, R. B. (2016). Daymet: daily surface weather data on a 1-km grid for North America, Version 2. *ORNL DAAC, Oak Ridge, Tennessee, USA*.

Thorp, J. M., & Scott, B. C. (1982). Preliminary calculations of average storm duration and seasonal precipitation rates for the northeast sector of the united states. *Atmospheric Environment (1967)*, *16*(7), 1763–1774. https://doi.org/10.1016/0004-6981(82)90269-4

Tong, D., Zhang, Q., Zheng, Y., Caldeira, K., Shearer, C., Hong, C., Qin, Y., & Davis, S. J. (2019). Committed emissions from existing energy infrastructure jeopardize 1.5 °C climate target. *Nature*, *572*(7769), 373–377. https://doi.org/10.1038/s41586-019-1364-3

Trenberth, K. E., & Shea, D. J. (2005). Relationships between precipitation and surface temperature. *Geophysical Research Letters*, *32*(14), 1–4. https://doi.org/10.1029/2005GL022760

Troy, T. J., Kipgen, C., & Pal, I. (2015). The impact of climate extremes and irrigation on US crop yields. *Environmental Research Letters*, *10*(5). https://doi.org/10.1088/1748-9326/10/5/054013

Ukkola, A. M., De Kauwe, M. G., Roderick, M. L., Abramowitz, G., & Pitman, A. J. (2020). Robust Future Changes in Meteorological Drought in CMIP6 Projections Despite Uncertainty in Precipitation. *Geophysical Research Letters*, *47*(11), e2020GL087820. https://doi.org/10.1029/2020GL087820

UNEP. (2020). *Emissions Gap Report 2020*. 1–102. https://www.unenvironment.org/interactive/emissions-gap-report/2019/

United Nations, Department of Economic and Social Affairs, P. D. (2019). World Population Prospects 2019: Data Booket. In *ST/ESA/SER. A/424.*

Urban, D. W., Roberts, M. J., Schlenker, W., & Lobell, D. B. (2015). The effects of extremely wet planting conditions on maize and soybean yields. *Climatic Change*, *130*(2), 247–260. https://doi.org/10.1007/s10584-015-1362-x

Urban, D. W., Sheffield, J., & Lobell, D. B. (2015). The impacts of future climate and carbon dioxide changes on the average and variability of US maize yields under two emission scenarios. *Environmental Research Letters*, *10*(4). https://doi.org/10.1088/1748-9326/10/4/045003

US Environmental Protection Agency. (2021). *Inventory of U.S. greenhouse gas emissions and sinks: 1990-2019*.

USDA. (n.d.). *USDA Quickstats.* http://quickstats.nass.usda.gov/

Vafeidis, A. T., Nicholls, R. J., McFadden, L., Tol, R. S. J., Hinkel, J., Spencer, T., Grashoff, P. S., Boot, G., & Klein, R. J. T. (2008). A new global coastal database for impact and

vulnerability analysis to sea-level rise. *Journal of Coastal Research*, *24*(4), 917–924. https://doi.org/10.2112/06-0725.1

van der Velde, M., Wriedt, G., & Bouraoui, F. (2010). Estimating irrigation use and effects on maize yield during the 2003 heatwave in France. *Agriculture, Ecosystems and Environment*, *135*(1–2), 90–97. https://doi.org/10.1016/j.agee.2009.08.017

Van Der Wiel, K., Selten, F. M., Bintanja, R., Blackport, R., & Screen, J. A. (2020). Ensemble climate-impact modelling: extreme impacts from moderate meteorological conditions. *Environmental Research Letters*, *15*(3). https://doi.org/10.1088/1748-9326/ab7668

Van Elewijk, L. (1989). Stemflow on maize: A stemflow equation and the influence of rainfall intensity on stemflow amount. *Soil Technology*, *2*, 41–48.

Van Vuuren, D. P., Van Soest, H., Riahi, K., Clarke, L., Krey, V., Kriegler, E., Rogelj, J., Schaeffer, M., & Tavoni, M. (2016). Carbon budgets and energy transition pathways. *Environmental Research Letters*, *11*(7). https://doi.org/10.1088/1748-9326/11/7/075002

Vautard, R., Yiou, P., & Ghil, M. (1992). Singular-spectrum analysis: A toolkit for short, noisy chaotic signals. *Physica D: Nonlinear Phenomena*, *58*(1–4), 95–126. https://doi.org/10.1016/0167-2789(92)90103-T

Vietnam Ministry of Agriculture and Rural Development. (2011). *Technical Guidelines on Sea Dike Design*.

Viguié, V., Juhel, S., Ben-Ari, T., Colombert, M., Ford, J. D., Giraudet, L. G., & Reckien, D. (2021). When adaptation increases energy demand: A systematic map of the literature. *Environmental Research Letters*, *16*(3). https://doi.org/10.1088/1748-9326/abc044

Vogel, E., Donat, M. G., Alexander, L. V, Meinshausen, M., Ray, D. K., Karoly, D., Meinshausen, N., & Frieler, K. (2019). The effects of climate extremes on global

agricultural yields. *Environmental Research Letters*, *14*, 054010.

Vogel, M. M., Orth, R., Cheruy, F., Hagemann, S., Lorenz, R., van den Hurk, B. J. J. M., & Seneviratne, S. I. (2017). Regional amplification of projected changes in extreme temperatures strongly controlled by soil moisture-temperature feedbacks. *Geophysical Research Letters*, *44*(3), 1511–1519. https://doi.org/10.1002/2016GL071235

Wei, Z., Yoshimura, K., Wang, L., Miralles, D. G., Jasechko, S., & Lee, X. (2017). Revisiting the contribution of transpiration to global terrestrial evapotranspiration. *Geophysical Research Letters*, *44*(6), 2792–2801. https://doi.org/10.1002/2016GL072235

Welch, J. R., Vincent, J. R., Auffhammer, M., Moya, P. F., Dobermann, A., & Dawe, D. (2010). Rice yields in tropical/subtropical Asia exhibit large but opposing sensitivities to minimum and maximum temperatures. *Proceedings of the National Academy of Sciences of the United States of America*, *107*(33), 14562–14567. https://doi.org/10.1073/pnas.1001222107

Westra, S., Fowler, H. J., Evans, J. P., Alexander, L. V., Berg, P., Johnson, F., Kendon, E. J., Lenderink, G., & Roberts, N. M. (2014). Future changes to the intensity and frequency of short-duration extreme rainfall. *Reviews of Geophysics*, *69*(37), 34. https://doi.org/10.1029/88EO01108

Zahran, H. H. (1999). Rhizobium-Legume Symbiosis and Nitrogen Fixation under Severe Conditions and in an Arid Climate. *Microbiology and Molecular Biology Reviews*, *63*(4), 968–989.

Zeyringer, M., Price, J., Fais, B., Li, P. H., & Sharp, E. (2018). Designing low-carbon power systems for Great Britain in 2050 that are robust to the spatiotemporal and inter-annual variability of weather. *Nature Energy*, *3*(5), 395–403. https://doi.org/10.1038/s41560-018-0128-x

Zhang, H., & Sonnewald, U. (2017). Differences and commonalities of plant responses to single and combined stresses. *Plant Journal*, *90*(5), 839–855. https://doi.org/10.1111/tpj.13557

Zhang, T., Lin, X., & Sassenrath, G. F. (2015). Current irrigation practices in the central United States reduce drought and extreme heat impacts for maize and soybean, but not for wheat. *Science of the Total Environment*, *508*, 331–342. https://doi.org/10.1016/j.scitotenv.2014.12.004

Zhang, W., Villarini, G., Scoccimarro, E., & Vecchi, G. A. (2017). Stronger influences of increased CO2 on subdaily precipitation extremes than at the daily scale Wei. *Geophysical Research Letters*, *44*, 7454–7471. https://doi.org/10.1002/2017GL074024

Zhao, C., Liu, B., Piao, S., Wang, X., Lobell, D. B., Huang, Y., & Huang, M. (2017). Temperature increase reduces global yields of major crops in four independent estimates. *Proceedings of the National Academy of Sciences*, *114*(35), 1–6. https://doi.org/10.1073/pnas.1701762114

Zhou, S., Williams, A. P., Lintner, B. R., Berg, A. M., Zhang, Y., Keenan, T. F., Cook, B. I., Hagemann, S., Seneviratne, S. I., & Gentine, P. (2021). Soil moisture–atmosphere feedbacks mitigate declining water availability in drylands. *Nature Climate Change*, *11*(1), 38–44. https://doi.org/10.1038/s41558-020-00945-z

Zhu, X., & Troy, T. J. (2018). Agriculturally relevant climate extremes and their trends in the world's major growing regions. *Earth s Future*, *6*, 656–672.

Zscheischler, J., Martius, O., Westra, S., Bevacqua, E., Raymond, C., Horton, R. M., van den Hurk, B., AghaKouchak, A., Jézéquel, A., Mahecha, M. D., Maraun, D., Ramos, A. M., Ridder, N. N., Thiery, W., & Vignotto, E. (2020). A typology of compound weather and climate events. *Nature Reviews Earth and Environment*, *1*(7), 333–347.

https://doi.org/10.1038/s43017-020-0060-z

Zscheischler, J., & Seneviratne, S. I. (2017). Dependence of drivers affects risks associated with compound events. *Science Advances*, *3*(6), 1–11. https://doi.org/10.1126/sciadv.1700263